2002

Large eddy simulations of atmospheric convection on Mars

Timothy I. Michaels
San Jose State University

Follow this and additional works at: https://scholarworks.sjsu.edu/etd_theses

Recommended Citation

Michaels, Timothy I., "Large eddy simulations of atmospheric convection on Mars" (2002). *Master's Theses*. 2326.
DOI: https://doi.org/10.31979/etd.hj7r-457k
https://scholarworks.sjsu.edu/etd_theses/2326

INFORMATION TO USERS

This manuscript has been reproduced from the microfilm master. UMI films the text directly from the original or copy submitted. Thus, some thesis and dissertation copies are in typewriter face, while others may be from any type of computer printer.

The quality of this reproduction is dependent upon the quality of the copy submitted. Broken or indistinct print, colored or poor quality illustrations and photographs, print bleedthrough, substandard margins, and improper alignment can adversely affect reproduction.

In the unlikely event that the author did not send UMI a complete manuscript and there are missing pages, these will be noted. Also, if unauthorized copyright material had to be removed, a note will indicate the deletion.

Oversize materials (e.g., maps, drawings, charts) are reproduced by sectioning the original, beginning at the upper left-hand corner and continuing from left to right in equal sections with small overlaps.

LARGE EDDY SIMULATION OF ATMOSPHERIC CONVECTION ON MARS

A Thesis

Presented to

The Faculty of the Department of Meteorology

San Jose State University

In Partial Fulfillment

of the Requirements for the Degree

Master of Science

by

Timothy I. Michaels

August 2002

UMI Number: 1410426

UMI®

APPROVED FOR THE DEPARTMENT OF METEOROLOGY

_____
Dr. Scot Rafkin

_____
Dr. Alison Bridger

_____
Dr. Robert Haberle, NASA Ames Research Center

APPROVED FOR THE UNIVERSITY

_____

ABSTRACT

LARGE EDDY SIMULATION OF ATMOSPHERIC CONVECTION ON MARS

by Timothy I. Michaels

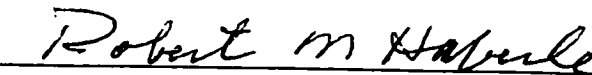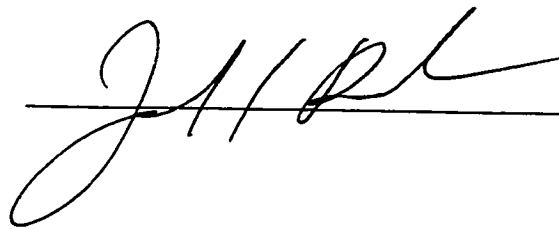This thesis addresses the detailed nature of daytime convection in the atmospheric boundary layer (ABL) of Mars. Thus far, there have been no detailed, three–dimensional studies of Mars' ABL. However, it is the ABL that primarily affects spacecraft descent, landed operations, surface erosion, and the initial transport of eroded materials. Extremely few data exist for this atmospheric region, so numerical simulations were performed using the Mars Regional Atmospheric Modeling System (MRAMS).

The modifications made to a terrestrial mesoscale model (RAMS — Colorado State University) that yielded MRAMS are described, and MRAMS results are compared with lander measurements. Large Eddy Simulation (LES) results are explored in detail and found to be only outwardly similar to Earth's ABL. Important differences in scale and energy transport are discussed. Finally, small–scale convective vortices in the LES solution, many of which would likely be described by an observer as dust devils, are examined.

ACKNOWLEDGMENTS

I wish to thank those people who in some way helped me in the completion of this work:

TABLE OF CONTENTS

1. INTRODUCTION

1.1 Complexity and Importance of Atmospheric Phenomena on Mars

Many decades of continuing observational and direct explorations have enabled humankind to make great leaps in the understanding of Mars. However, the same data have revealed an ever-increasing number and variety of observed or inferred atmospheric phenomena that cannot be adequately simulated by current Mars general circulation models or even measured *in situ* in any practical fashion, and are therefore relatively poorly understood. Strong radiative forcing of the Martian atmosphere (Haberle et al. 1993), widespread complex and extreme topography, and highly variable patterns of surface albedo and thermal inertia combine to produce strong local and regional slope winds both during the day and at night, every sol (Mars solar day; 88775 seconds). Dust storms often initiate in quite localized regions, and all manner of obstacles have been seen to perturb the atmospheric flow (e.g., wind streaks, mountain/gravity waves and associated clouds). Dust devils occur frequently over much of Mars and are nearly an order of magnitude larger in size than their terrestrial counterparts. It has been postulated that Martian dust devils are a significant element in the maintenance of the relatively constant dust loading of the atmosphere. Perhaps most importantly, the above-mentioned phenomena may pose a threat to all direct exploration of Mars. Namely, it is possible that the descent and landed stages of nearly any robotic or manned mission to Mars could be significantly affected, even terminated, by regional and/or local weather. This work is undertaken in an effort to begin to characterize the above-mentioned localized atmospheric processes.

1.2 Definitions

Although an atmosphere has processes on a continuum of spatial and temporal scales, two broad spatial scale classifications will be made and used throughout this paper in order to facilitate discussion. Atmospheric phenomena that are able to be resolved on a finite–difference grid with a horizontal spacing of $4 \leq \Delta x \leq 60$ kilometers are classified as *mesoscale*. Those resolvable with a horizontal gridspacing of $1 \leq \Delta x \leq 3999$ meters are classified as *microscale*.

A number of acronyms will be used repeatedly throughout the discussion:

RAMS: *Regional Atmospheric Modeling System*; a regional (i.e., not global), nonhydrostatic, terrestrial atmospheric model developed at Colorado State University.

MGCM: *Mars General Circulation Model*; any global, typically hydrostatic atmospheric model for Mars.

MRAMS: *Mars Regional Atmospheric Modeling System*; a version of RAMS heavily modified for use on Mars (developed at San Jose State University).

PBL or ABL: *Planetary or Atmospheric Boundary Layer*; the layer of the atmosphere bounded and significantly affected by the planetary surface.

CBL: *Convective Boundary Layer*; a special case where large–scale convection is a dominant process within the ABL.

LES: *Large Eddy Simulation*; a microscale numerical atmospheric simulation in which the large turbulent eddies (i.e., those that contain the vast

majority of the total turbulent energy) are explicitly resolved (not parameterized) by the model numerics. The contribution of all smaller eddies is parameterized.

1.3 Previous Research

1.3.1 Observations

The existence of a thin Martian atmosphere has been postulated since at least 1784, when the noted astronomer Sir William Herschel published a paper in which he concluded that if Mars has an atmosphere, it must be relatively tenuous compared to that of Earth. Soon afterward, telescopes evolved to the point that distinct bright spots (clouds) were resolvable that changed over hours or days. This was further evidence that Mars has an atmosphere, and the first clue that the Martian atmosphere is dynamic (i.e., it does not remain motionless and clear). Antoniadi (1930) reported that beginning in 1877, large obscurations of the planet's surface occurred — dust storms. These dust storms provided evidence that Mars' atmosphere is capable of eroding the planet's surface and of large–scale, energetic organization.

Images from the Mariner 6 and 7 spacecraft offered the first close look at Martian clouds. Mariner 9 arrived at Mars in 1971, in the midst of a gigantic dust storm, and measured the upper extent of the dust as being approximately 70 kilometers. This spacecraft also was the first to image local dust storms, synoptic–scale fronts, ground fogs in valleys, wave clouds over craters, lee waves downwind of obstacles, bright and dark wind streaks (some of which changed over time) in the lee of obstacles, and dune fields. These were the first solid clues that the atmosphere of Mars contributes

significantly to the state of the planet's surface. Later, the two Viking Landers recorded huge seasonal pressure changes at their locations, and also recorded dust devil transits near or over them. The Viking Orbiters recorded large mid–latitude storms (not associated with dust), numerous images of dust devils (and discovering their huge size in both width and height), and many more observable atmospheric phenomena.
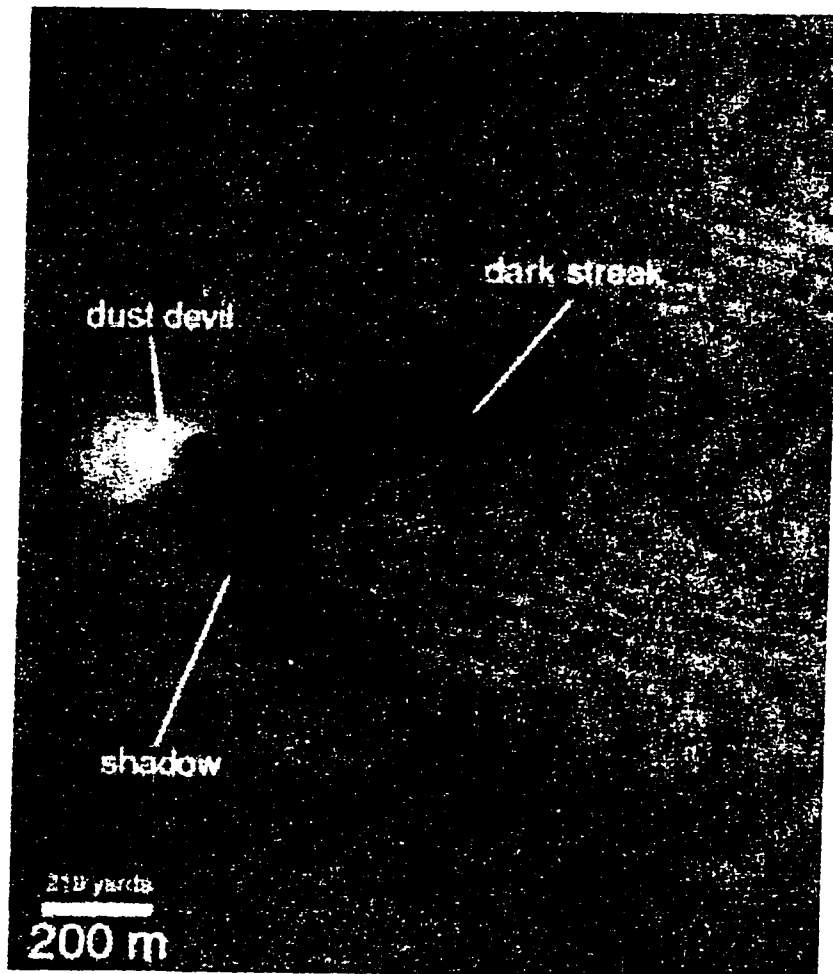
Figure 1. Mars Global Surveyor MOC image of a Mars dust devil
(Image credit: NASA/JPL/Malin Space Science Systems)

Observations using the Hubble Space Telescope and ground–based telescopes (even amateur instruments) have also yielded insight, especially as a method to bridge temporal gaps between spacecraft reconnaissance of Mars (such as during the 1980s and

4

the first half of the 1990s). The Mars Pathfinder mission in 1997 and the present Mars Global Surveyor (Figure 1) and Mars Odyssey missions have only added to the mysteries of the observed variability of Mars' atmosphere. It is important to realize that most of these observations have been made during local daylight hours and there may be even more interesting phenomena that take place at night (katabatic winds, clouds, etc.). Thus, one might reach the conclusion, based on the available evidence, that Mars' atmosphere is quite dynamic on large, intermediate, and small spatial and temporal scales.

The above—mentioned observations may provide clues to the existence of certain atmospheric processes, but they typically cannot provide information about the detailed three—dimensional structure and causation of such phenomena. To obtain such information, one needs to employ a relatively new tool, the numerical atmospheric model.

1.3.2 Mars Atmospheric Modeling

The pioneering MGCM work (using the full primitive equations) by Leovy and Mintz (1969) shed light on the poleward transport of energy in Mars' atmosphere. MGCMs used by Mass and Sagan (1976) and Moriyama and Iwashima (1980) employed simplified equations of motion, but provided insight into the effects orography has on dust lifting and heating. The NASA Ames Research Center MGCM, using a full primitive equation core from the terrestrial UCLA GCM, was developed and gradually improved by Pollack et al. (1976, 1981, 1990), and later Haberle et al. (1993b, 1999). It was this model that helped interpret Viking Lander and Orbiter data during the 1980s and

early 1990s and allowed the large–scale circulations of the Martian atmosphere to be studied and understood in some detail. Advances in computer technology led to the birth during the 1990s of new MGCMs such as the GFDL (Wilson and Hamilton 1996) and Oxford–LMD (Forget et al. 1999) models. Today, results from each of the three modern MGCMs may be compared to better refine our understanding of large–scale atmospheric processes on Mars.

Just as telescopic and even spacecraft measurements are currently not sufficient to understand the detailed nature of large–scale atmospheric processes, the capability of current MGCMs is often insufficient to understand regional and local Martian weather. There are two main reasons for this: First, the horizontal grid spacing (or effective resolution, in the case of a spectral model) of MGCMs is often several hundred kilometers or more at the equator, and the models cannot resolve a feature less than about three times that spacing in size. Phenomena forced by albedo, thermal inertia, or topographic variation at a smaller scale than that are not part of the MGCM solution. Secondly, MGCMs employ the hydrostatic approximation to simplify computations. This approximation may not be strictly appropriate for even regional–scale motions on Mars, due in part to the weak Martian gravity, extreme topography, and strong radiative forcing. The typical mesoscale numerical model has neither of those limitations.

There have also been many excellent one– and two–dimensional numerical studies of the Martian atmosphere that have yielded much insight. In particular, the Mars Mesoscale Circulation Model (MMCM), developed at the University of Helsinki, Department of Meteorology (UH/MET) in the early 1990s (Savijarvi and Siili 1993), was the first concerted foray into mesoscale atmospheric processes on Mars. A two–

dimensional version of the MMCM was used to investigate the effects of mesoscale topography and surface characteristic variations on the atmosphere (Savijarvi and Siili 1993; Siili 1996). The MMCM results brought to light the strong mesoscale forcing of Mars' atmosphere, and initiated a worldwide impetus to construct other Mars mesoscale atmospheric models. The work described in this thesis was largely born from that impetus.

Recently, two other three–dimensional Mars mesoscale models have been developed (Tyler et al. 2002; Toigo and Richardson 2002), both derived from the MM5 terrestrial mesoscale model. Both of these models have been employed to study mesoscale processes on Mars. The only Mars LES (microscale) work done thus far has been the two–dimensional modeling studies of Odaka et al. (1998, 2001). These studies were undertaken with simplified model physics and radiative transfer, yet yielded invaluable clues to the nature of the Martian CBL. The actual convective boundary layer is three–dimensional, however, and all three dimensions are likely to be important. The current work aims to elucidate the CBL's full structure.

1.3.3 RAMS and MRAMS

The Mars Regional Mesoscale Modeling System (MRAMS) was developed at San Jose State University (Rafkin et al. 2001) and is derived from the Regional Atmospheric Modeling System (RAMS), which was developed at Colorado State University in the mid–1980s. RAMS represents a fusion of several terrestrial weather simulation codes (Mahrer and Pielke 1977; Tripoli and Cotton 1982; Tremback and Kessler 1985; Pielke et al. 1992). Since that time, RAMS has become a powerful and

widely–used model for the study of a wide range of phenomena including but not limited to: structure and evolution of the stable and convective boundary layer through the use of Large Eddy Simulations (Hadfield et al. 1991; Walko et al. 1992), physiographically forced mesoscale systems such as downslope windstorms (Lee et al. 1989; Wesley et al. 1990), thermally forced circulations (Xian and Pielke 1989; Pielke et al. 1991), and wintertime baroclinic storm systems (Meyers and Cotton 1992).

MRAMS is a non–hydrostatic model easily configured over a wide range of user–specified regions and has a horizontal grid spacing that can range from meters to hundreds of kilometers. The vertical coordinate is a terrain–influenced "sigma–z" system that may be geometrically stretched with height to provide highest resolution in the boundary layer. Typical vertical grid spacing is on the order of a few meters near the surface and several hundred meters or more in the free atmosphere.

An unlimited number of multiple–nested, two–way interactive grids may be easily added, which allow for the capture of small–scale phenomena embedded in larger–scale systems. Physical parameterizations and packages available in MRAMS include several turbulence schemes with closures up to a level 2.5 prognostic turbulent kinetic energy equation (e.g., the closures described by Deardorff in 1980 and Mellor and Yamada in 1982), a multiple level prognostic soil model (Tremback and Kessler 1985), and a surface layer model with fluxes tied to atmospheric structure functions which are themselves a function of the Richardson Number (Louis 1979). Variations in surface aerodynamic roughness length, albedo, and thermal inertia are permitted. A variety of lateral and upper boundary conditions are also available.

Strictly speaking, MRAMS is more than just numerical integration code. At the

front end, a custom preprocessing package allows for the ingestion of MGCM or larger-scale MRAMS atmospheric simulation output in order to provide initialization data and time dependent lateral boundary conditions through four–dimensional data assimilation. This preprocessor is used with MRAMS to provide as realistic a setting for simulation as possible and enables use of the model in any Martian season and at nearly any spatial or temporal resolution. At the back end, there are a variety of post–processing and visualization tools built around the National Center for Atmospheric Research (NCAR) graphics libraries. Options for output formats of other analysis packages (GrADS, Vis5D) are also available.

1.3.4 Large Eddy Simulation (LES) of Earth's ABL

A Large Eddy Simulation is a numerical simulation of the atmosphere in which the horizontal and vertical model gridspacing are on the order of 100 meters or less. This approach explicitly resolves the dominant, energy–carrying large eddies in the CBL, enabling one to use a relatively simple scheme to parameterize the effects of subgrid–scale turbulence and viscous energy dissipation. The primary use for LES in the atmospheric sciences is to investigate the complex processes that occur in the ABL, largely in order to create more realistic turbulence parameterizations for mesoscale and general circulation models.

The pioneering work in this area was done by Deardorff (1972). That first investigation compared relatively well with available observations. However, computational power proved to be a severely limiting factor, and little additional numerical work was published until the mid–1980s, when computers had improved

sufficiently. By the close of that decade, the primary structure of the convective boundary layer had been described in detail (Schmidt and Schumann 1989), though there are a paucity of observations to compare those results to. Briefly, the buoyantly–driven ABL is seen to develop quasi–steady cellular updraft/downdraft structures, roughly hexagonal in shape, with narrow, intense updrafts surrounding much wider and less intense downdrafts.

As computer capability continued to improve, additional investigations were conducted, such as comparing shear– and buoyancy–driven ABLs (Moeng and Sullivan 1994). The widening of the cellular structures with time in LES has been noted by Fiedler and Khairoutdinov (1994) and Dornbrack (1997). Recently, Kanak (2000) has laid the groundwork for the numerical investigation of small–scale vortices in the CBL (e.g., dust devils).

1.4 Present Approach

The work described in this paper can be divided into three discrete tasks: The first is to modify the most recent version of the terrestrial RAMS model (version 4.3.0) for use on Mars. This involves generating custom code to ingest nonstandard MGCM and spacecraft datasets, adding a Mars radiative transfer scheme, and implementing topographic shadowing, to name a few examples. The second task involves comparing MRAMS mesoscale results to two lander time series (Viking Lander 1 and Mars Pathfinder) of wind magnitude, wind direction, and air temperature. This is done to lend a measure of credibility to the model results so that MRAMS may be applied to other Mars locales with some degree of confidence, even if no observational data is available

there. The third task is to perform a partially idealized LES for conditions and a location similar to that of the Mars Pathfinder mission. This investigation is meant to explore the unknown microscale structure of Mars' atmosphere and if possible, compare with the structure of Earth's ABL.

2. MODEL MODIFICATIONS

2.1 General

2.1.1 Atmospheric and Planetary Constants

The gross physical similarities between the atmospheres of Mars and Earth (i.e., both are a relatively rapidly rotating and shallow layer of fluid having an open upper boundary and an impervious lower boundary) allow the core dynamical and thermodynamical equations within RAMS (or indeed most terrestrial atmospheric models) to remain unchanged, except for several constants. A detailed look at Mars' atmosphere reveals that it is quite different from that of Earth. Owen (1992) states that it is primarily composed of carbon dioxide (95.32%), nitrogen (2.7%), and argon (1.6%). The global average surface pressure is only about 600 Pa, and the temperature regime is much colder than that of Earth. Clearly, one cannot use many Earth atmospheric constants in this situation. Additionally, Mars is much less massive than Earth (and roughly half its size), and thus has a lesser gravitational acceleration at its surface. Mars' angular rotation rate is only slightly less than that of Earth. Table 1 lists the Mars values of the model constants that required alteration.

ATMOSPHERE	Value	Units
Gas constant, R	192.0	$J\ K^{-1}\ kg^{-1}$
Heat capacity (at constant pressure), c_p	770.0	$J\ K^{-1}\ kg^{-1}$
Heat capacity (at constant volume), c_v	578.0	$J\ K^{-1}\ kg^{-1}$
PLANET		
Surface gravity, g	3.72	$m\ s^{-2}$
Planetary radius, r_M	3.390E+06	m
Planetary rotation rate, Ω	7.088E-05	$rad\ s^{-1}$

Table 1. Constants modified for Mars

2.1.2 Mars Timekeeping

Due to the close similarity between the length of a solar day on Mars and Earth, and the familiar division of an Earth day into 24 hours, it seems natural to partition a Martian day, or sol, into 24 Mars–hours (a Mars–hour approximately equals 3699 seconds). Each Mars–hour can be divided into 60 Mars–minutes. Further analogous divisions (e.g., Mars–seconds) may be made, but doing so risks confusion with the universal unit of time (the second). The orbital period of Mars is roughly 687 Earth days (669.6 sols), and thus no obvious extension of any familiar Earth calendar would be of practical use. However, heliocentric longitude (i.e., where the planet is with respect to a fixed reference point on its orbit, measured as an angular distance) serves the same purpose. In practice, heliocentric longitude is not used directly, as it does not have a permanent correlation with the Martian equinoxes. Instead, one uses a quantity known as L_s (alternative names: areocentric longitude and Mars seasonal index), which is defined as the heliocentric longitude plus some constant offset so that in a given astronomical

13

Epoch, $L_s = 0°$ corresponds to the Northern Hemisphere vernal equinox on Mars.

Earth RAMS uses dates extensively in its filename conventions, as well as in its preprocessing and post–processing routines. In light of the above Mars considerations, this reliance on calendar dates was removed from MRAMS. The replacement routines and filename conventions are based on the current model time (in seconds), areocentric longitude, and Mars solar time.

2.2 Surface and Regolith Characteristics

2.2.1 Topography

In order to obtain relevant and realistic topographic information for each of its finite grids, MRAMS uses the following procedure: Each grid point is assigned the mean value of all topographic dataset points within a square area centered on the grid point. The length of each side of that area is normally twice the model gridspacing (however, this quantity is adjustable) in order to remove topographic modes that may force atmospheric motions that the finite difference grid cannot properly treat. Also, several other topographic schemes are available, including silhouette averaging.

MRAMS currently uses a publicly available, global, gridded topography dataset derived from results of the Mars Orbiter Laser Altimeter (MOLA), an instrument aboard the Mars Global Surveyor (MGS) spacecraft currently in Mars orbit. The gridspacing of the dataset is 1/32 of a degree in longitude and latitude (about 1.85 kilometers at the equator).

2.2.2 Albedo

Surface albedo is treated using the same mean value algorithm as topography (see

Section 2.2.1). The dataset used is derived from Thermal Emission Spectrometer (TES

— onboard the Mars Global Surveyor spacecraft) measurements, and has a gridspacing

of 1/8 of a degree in longitude and latitude (about 7.4 kilometers at the equator). This

dataset is not truly global, however, as data quality decreases markedly above the mid–

latitudes and there are data voids near both poles.

2.2.3 Regolith Properties (Thermal Inertia, Density, etc.)

Regolith thermal inertia is interpolated from a gridded dataset in the same fashion

as albedo (see Section 2.2.2). The dataset used is derived from Thermal Emission

Spectrometer measurements, and has a gridspacing of 1/8 of a degree in longitude and

latitude (about 7.4 kilometers at the equator). This dataset must be used with caution,

however, as data quality significantly decreases poleward of mid–latitudes.

Thermal inertia is used in conjunction with a fixed regolith volumetric heat

capacity (density × heat capacity) to obtain an approximate value for the regolith thermal

conductivity (assumed valid for all levels of the finite–differenced regolith model). The

regolith density used is 1500 kg m^{-3}, and the regolith heat capacity is 711 J K^{-1}kg^{-1}.

These values are the midpoints of the currently estimated ranges of the quantities. For

more information, consult Rafkin et al. (2001).

2.3 Radiative Transfer

The radiative transfer code in MRAMS is directly derived from that in the NASA

Ames Mars GCM (Haberle et al. 1993a). The MRAMS version of the code was

completely rewritten to ensure compatibility with the rest of the model and to implement

15

the following modifications:

The NASA Ames MGCM uses sigma–pressure (σ_p) vertical coordinates and is hydrostatic, which significantly simplifies the implementation and memory footprint of the radiative transfer code. However, MRAMS is a nonhydrostatic, sigma–height (σ_z) model. Emissivity coefficients, for example, vary strongly with pressure. The pressures on each of the MGCM vertical levels are a function of surface pressure alone, whereas the pressures on MRAMS levels are highly variable in space and time. Therefore, porting the code involved creating large, high resolution lookup tables resident in memory (corresponding to longer initialization times) to avoid the extremely expensive recomputation of emissivity coefficients every radiation timestep for all gridpoints in the domain. Even if MRAMS were hydrostatic and used σ_p coordinates, one would still have need for higher resolution lookup tables, since MRAMS is a mesoscale model, and has smaller vertical gridspacing than a MGCM.

Nocturnal, surface–based radiation inversions on Mars can be extremely strong (50–100 K), and at the same time quite shallow (only a few hundred meters deep). This creates a great deal of structure in the lowest several hundred meters of the radiative heating profile that may not be properly resolved with the normal vertical spacing of MRAMS. Therefore, a method of imposing (in the radiative transfer flux calculations only) a finer vertical gridspacing near the surface was developed. The fine mesh gridspacing is geometrically stretched from the surface to a specified MRAMS level, where it exactly matches the normal vertical gridspacing. Within the fine mesh region, calculated radiative fluxes are interpolated back to the regular vertical grid before the

final diagnosis of flux divergence (and thus radiative heating rate) is performed.

The logic necessary to implement topographic shadowing (see Section 2.4.1) was emplaced. Also, the logic needed to implement topographic slope and aspect angle shortwave radiative effects (see Section 2.4.2) was added. In support of this, a routine to calculate the instantaneous solar azimuth angle was developed. The solar azimuth angle is calculated using the following equation:

$$azimuth \ angle \ = \ \arccos[\frac{\lfloor(\cos(Z)\cdot\sin(\phi))-\sin(\delta)\rfloor}{[\sin(Z)\cdot\cos(\phi)]}] \ ,$$

where Z is the solar zenith angle, δ is the solar declination angle (latitude at which the Sun is currently directly overhead), and ϕ is the latitude of the current grid point.

2.4 Topographic Effects on Radiative Transfer

2.4.1 Shadowing

Mars' topography is quite extreme and complex due to its thin atmosphere (little protection from impacting bodies, more difficult for significant aeolian erosion to occur), lack of macroscale life (at least), present lack of significant erosional processes due to liquid water, and lesser gravity, to name a few reasons. In reality this topography casts a myriad shadows. Indeed, without the shadows it would be difficult for the human eye to discern depth in a spacecraft image of Mars. Similarly, it is the supposition here that without the inclusion of topographic shadowing in a mesoscale Mars atmospheric model, an accurate representation of the atmosphere is not possible (particularly at small spatial grid scales). On Mars, due to the ease with which the regolith may radiate energy into

17

space (the thin atmosphere provides little insulation and relatively low regolith thermal inertia is common), shadowed areas may be much colder than sunlit ones, leading to local pressure gradients and atmospheric flows that would not otherwise exist. It is believed that at present, no full mesoscale atmospheric model (applied to any planet) has fully taken topographic shadowing into account. Thus, in order to be capable of accurately modeling small–scale flows near complex topography on Mars, a method of calculating topographic shadowing was devised. Most of the calculations necessary to achieve this functionality are performed during the initialization of MRAMS. During the time integration itself, only a few additional minor calculations and logical statements are needed.

The primary quantity calculated is *cosz_horizon* (the cosine of the solar zenith angle that must be achieved before the point in question becomes sunlit), which is a function of topography, planetary curvature, and azimuth. The following procedure is repeated for each gridpoint on every grid: The areocentric Cartesian (AC — an *xyz* coordinate system with the center of the Mars areoid as its origin) coordinates of the gridpoint are computed from its known areocentric spherical (AS — a spherical coordinate system with the center of the Mars areoid as its origin) coordinates $(\rho_p, \theta_p, \phi_p)$. Note that ρ_p is the true planetary radius at the gridpoint (the sum of the areoid radius and the topography height). A new topocentric Cartesian (TC) coordinate system is then defined by rotating the AC coordinate axes so that its new origin is at the gridpoint, the positive *z*–axis is directed towards the local zenith, and the *x*– and *y*–axes lie on the plane centered at the origin and tangent to a sphere with radius ρ_p (Figure 2a). The TC *xy* plane

corresponds to the ideal local horizon.

In order to capture the azimuthal dependence of *cosz_horizon*, it is computed for a number of traverses (currently 48), equally spaced in azimuth (direction) and projecting radially outward from each gridpoint along the TC *xy* plane. The distance along the
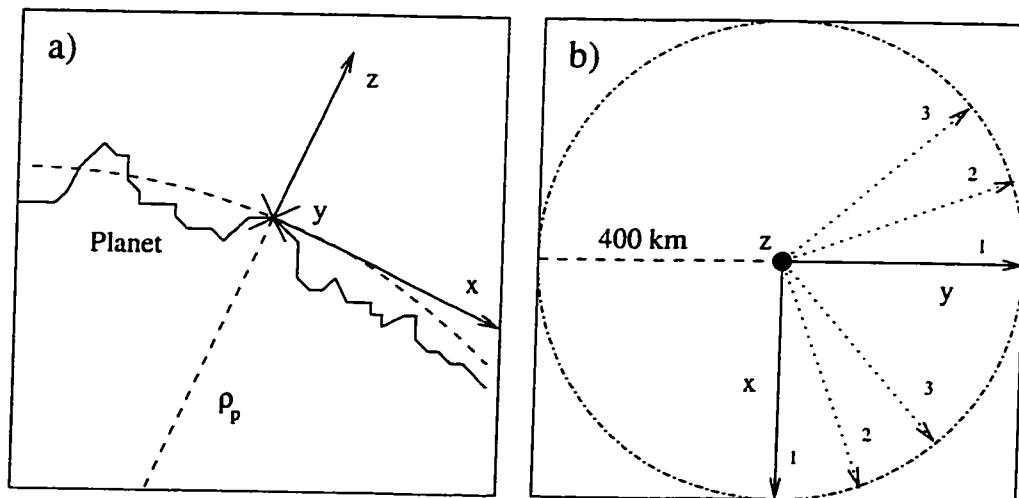

Figure 2.   (a) Lateral view of TC coordinate system   (b) Plan view of TC coordinate system, showing three successive azimuth traverses.

surface required for the most extreme topography found on Mars (Olympus Mons, which rises approximately 23 kilometers above the surrounding plain) to disappear below the horizon (due to mean planetary curvature) is approximately 400 kilometers. Therefore, each traverse is constrained to be about 400 kilometers in length. For each azimuth traverse the TC positive *x*-axis is rotated to correspond exactly to the traverse path (Figure 2b). This greatly simplifies later calculations. A series of TC points is then defined along the traverse, spaced apart a distance of one-third the horizontal model gridspacing. Each traverse point's TC coordinates are converted to AS coordinates and the planetary radius at that point is found (interpolated from the standard gridded topography dataset using overlapping quadratics). These new AS coordinates $(\rho_t, \theta_p, \phi_p)$

19

are then converted back to the TC system. The factor of three between the traverse point spacing and the model gridspacing is arbitrary, but it was adopted since it was found that if the factor was too large, interpolation errors could produce spurious topographic gradients, and if the factor was too small, the accuracy of the horizon angle calculation was reduced.

After the TC coordinates at all points on a particular azimuth traverse have been calculated, the maximum TC z-coordinate value along the traverse is found. This value and the distance of that point from the TC origin (i.e., the point's x-coordinate) are then used to calculate the elevation angle of that point as seen by an observer at the TC origin (using simple trigonometry). The sine of that elevation angle is *cosz_horizon*. If *cosz_horizon* is negative, the horizon is extended, and the Sun will rise earlier (or set later) at that location compared to a normal horizon case. However, since at such extended elevation angles solar energy must pass through a considerable amount of atmosphere, severely limiting its intensity, locations with extended horizons are constrained to receive only a fixed amount of insolation (an amount equivalent to a solar zenith angle of about 87.7 degrees) until the solar zenith angle becomes greater than about 87.7 degrees or the Sun sets below the local extended horizon. Alternatively, if *cosz_horizon* is positive, then the location will be in shadow for some finite amount of time. The portion of the column that is shadowed can be calculated by knowing the current solar elevation angle, the distance along the TC xy plane to the horizon obstruction, and the height of that obstruction. Only the shadowed portion of the atmospheric column receives zero insolation.

During time integration of the model, *cosz_horizon* has already been calculated

20

(during model initialization) for all azimuths around a given gridpoint. Thus for each radiation timestep, the current *cosz_horizon* is obtained by linearly interpolating to the current solar azimuth angle. The current horizon obstruction distance and height are obtained in the same fashion.

The current shadowing parameterization has some weaknesses. First of all, diffuse shortwave radiative energy is not accounted for within a shadowed region. However, diffuse shortwave energy should have a much smaller magnitude compared to the energy received by sunlit regions. Secondly, atmospheric refraction effects are neglected. Lastly, real horizon extension effects can be quite complicated and are currently treated very simply. A significant advantage of the current technique is that the actual shape of the planet can be accounted for (i.e., no assumptions about a flat local area or a perfectly spherical or ellipsoidal areoid).

2.4.2 Slope and Aspect Angle

Topographic slope and aspect angle (the mean direction that a given piece of ground is angled towards) are important radiative factors on Earth, and are even more necessary for realism on Mars. The method used here is uncomplicated, but appears to work well. The following operations are performed for every gridpoint on every grid at model initialization (only the values of topographic slope and aspect angle are used during time integration): The model topography is first interpolated to four points, each a distance of one-quarter the horizontal gridspacing from the current gridpoint and at one of the cardinal directions (north, south, west, and east). These values are then used to calculate the east-west and north-south topographic gradients (or slopes). Assuming

21

these two slopes to be the two orthogonal components of the total vector slope, the Pythagorean theorem is employed to yield the magnitude of the total slope. Finally, the arctangent of the ratio of those slopes (paying careful attention to the signs of each slope component) yields the topographic aspect angle at the current grid point.

2.5 Initial and Boundary Conditions

In its variable initialization mode, MRAMS boundary and initial conditions are derived from MGCM output fields. The most formidable obstacle to doing this is that there are sometimes large differences (up to 15 kilometers in the vertical) between the topography used in the MGCM and that used in MRAMS. Faced with such a potential challenge, the imposition of two constraints is necessary: The first is that the temperature and wind structure sufficiently far aloft should be preserved exactly (as these fields should not be affected significantly by the surface). The second is that the atmospheric boundary layer structure should be preserved as much as possible (e.g., if there is a 70 K inversion 300 meters deep, keep it as such, even if it requires a constant offset to be added to the actual temperatures). Constrained by the above, at each point where the MRAMS topography is less (more) than the MGCM topography, it is necessary to invent (delete) a portion of the MGCM atmospheric column. MGCM studies have found that the lower Martian atmosphere responds very quickly to direct and indirect radiative forcing. This suggests that the ABL temperatures, even if artificially offset, should adjust quickly back to a radiative quasi–equilibrium state. Thus it was decided to preserve the structure below a certain level (attempt to include the entire ABL) and extend (via extrapolation) or delete a depth of the atmosphere directly above

this preserved layer. The temperatures within the preserved lower layer are then offset by an appropriate constant, so that the uppermost temperature of this layer matches the adjacent gradient of the modified column above it. The wind profile is modified similarly, except that no offset is added to the lower layer profile. After the temperature profile modification the pressures at each model level are recalculated via hydrostatic integration.

The above method is not terribly elegant, and there is significant room for future refinement. Unfortunately, the problem is not well–posed from the start — the finite nature of the model grids leads to a mandatory difference between models' topography, and thus the deletion or invention of a portion of each atmospheric column is inevitable. However, in practice the above technique appears to work satisfactorily.

2.6 Subgrid–scale Turbulence Parameterization for LES

For the Martian LES it was deemed necessary to have a stretched vertical grid to reduce computational expense. However, the 1.5 order, TKE–based subgrid–scale turbulence model of Deardorff (1980) that was used performs best on a grid that is isotropic in all three dimensions (i.e., the gridspacing is equal in all directions). The main reason for this isotropic dependence lies in the definition of subgrid–scale mixing length. Deardorff defines mixing length as the cube root of the product of the x–, y–, and z–direction gridspacings. Another way to approach the problem (that would be better able to handle vertical grid anisotropy, and is used in this work) is to define two subgrid–scale mixing lengths: one for the horizontal directions, and another for the vertical direction. The horizontal scale is used to calculate horizontal mixing

23

coefficients, and the vertical scale is used to calculate vertical mixing coefficients. However, in the prognostic calculation of subgrid–scale TKE, Deardorff's definition of the mixing length is used, since it does contain information (however muted) about the full dimensions of each grid cube.

The vertical subgrid–scale mixing length is equal to the product of a vertical scaling constant and the vertical gridspacing at the current level. The horizontal subgrid–scale mixing length is analogous to the vertical one, being the product of a horizontal scaling constant and the square root of the product of the x– and y–direction gridspacings. It was found through numerical experiments that the values for the scaling constants, which in practice have a value equal to or slightly greater than unity on Earth, needed to be decreased by a factor of at least three in order to avoid overdiffusing the model solution for Mars. If the scaling constants (and thus ultimately the mixing coefficients) are too large, resolved–scale convection fails to initiate, and instead a very quiescent ABL develops due solely to the accumulated action of subgrid–scale diffusion. If the scaling constants are made too small, numerical noise ("2Δx" noise) quickly develops and dominates the model solution.

Many combinations of scaling values were tried, including pairs where the vertical scaling constant was much greater than the horizontal one, and vice versa. It was found that the horizontal scaling constant effectively controlled the timing of the onset of resolved–scale convection and the damping of numerical noise. In stark contrast, the model solution appeared to be much less sensitive to the value given to the vertical scaling constant. The significance of these observations is uncertain, especially given that the LES results themselves suggest that a terrestrial–type subgrid–scale turbulence

parameterization may not be valid near the surface except at very small gridspacings, if at all (see Section 4.2.2).

3. MESOSCALE SIMULATION AND MODEL VALIDATION

3.1 Simulation Design

3.1.1 Setup

The objective of this simulation was to resolve the primary mesoscale atmospheric structure and flows in the vicinity of the Viking 1 (VL1) and Mars Pathfinder (MPF) landing sites. The landers lie on opposite sides of Chryse Planitia, and are subject to all manner of slope and valley flows from multiple sources and directions. Initial and boundary conditions were obtained from the output of the NASA Ames MGCM, which has a horizontal gridspacing of 7.5 × 9 degrees. The coarseness of the MGCM grid and the complex topography of the region of interest prompted the use of a
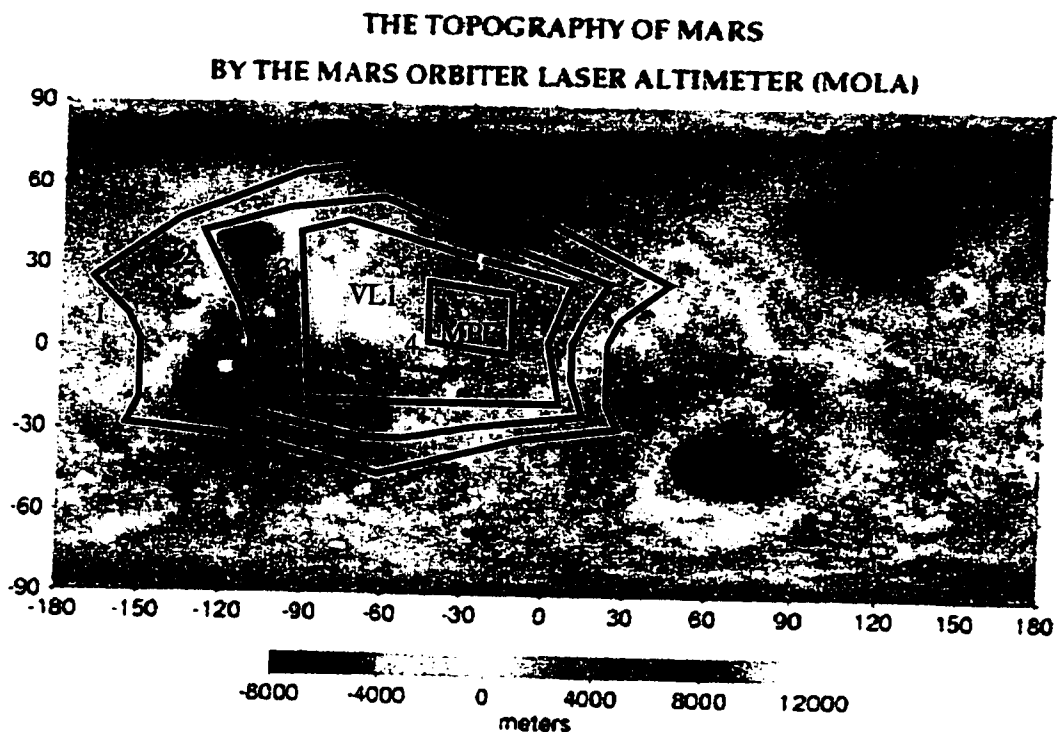

THE TOPOGRAPHY OF MARS
BY THE MARS ORBITER LASER ALTIMETER (MOLA)

Figure 3. Approximate areographic placement and size of grids 1 through 4 (landing sites are marked)

26

nearly hemispheric MRAMS first grid with a horizontal gridspacing of 240 kilometers in order to better resolve the effects of key large–scale topographic gradients and features. Figure 3 depicts the approximate placement and size of each of the first four grids. The placement and resolution of grid 2, with a horizontal gridspacing of 120 kilometers, was chosen so that it well–resolved and encompassed Ascraeus Mons and Alba Patera (in case those features produced atmospheric flows that might affect the Viking 1 or Mars Pathfinder sites). Grid 3 zooms in on the southern Chryse Planitia region using a
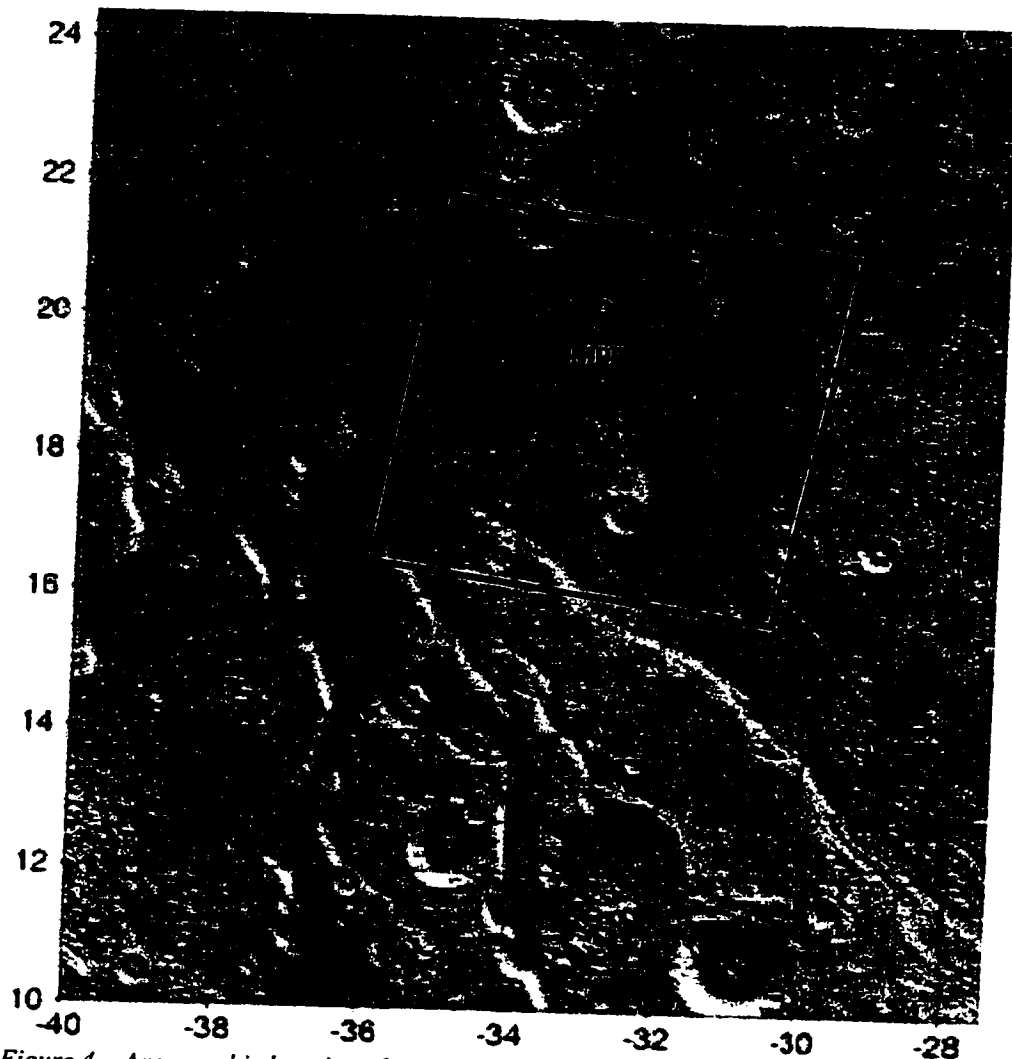
Figure 4. Areographic location of grid 5, with MPF landing site marked.
(Left scale: degrees of latitude, bottom scale: degrees of longitude)

27

horizontal gridspacing of 60 kilometers.

Grid 4, with a horizontal resolution of 20 kilometers, zooms in on the southeast periphery of Chryse Planitia with a main purpose of well–resolving a significant portion of Ares Vallis (which likely creates valley flows which affect the MPF site). Figure 4 shows the size and areographical placement of grid 5. The main purpose of grid 5 is to well–resolve the local complex topography surrounding the Mars Pathfinder landing site. Greater attention was placed on the MPF site, as that lander dataset has a much greater time resolution than that of Viking 1. Also, the MPF site is situated very near terrain more complex than exists near the VL1 site.

The stretched vertical grid was the same on all nested grids, with the lowest level being 14.4 meters above the surface and the greatest model layer thickness being 1000 meters. The lowest model level may seem unusually high (the lowest level in a modern MGCM is about 5 meters from the surface); this is a direct consequence of the nonhydrostatic nature of the model and the relatively high vertical grid resolution used in the atmospheric boundary layer. A lower first model level may be used, but the dynamical timestep required decreases nonlinearly, resulting in a much higher computational expense with little gain. The model top was approximately 35 kilometers above the surface at the MPF site. MRAMS was configured in its fully variable initialization mode for this simulation. This entails using MGCM output for initial and boundary conditions, spatially variable thermal inertia, albedo, and topography, an oblique polar stereographic projection, topographic effects on radiative transfer (shadowing and slope/aspect), and fully variable radiative and orbital parameters. Additionally, a static dust distribution was used, with a dust optical depth of 0.3 on a

pressure surface of 6.1 hPa.

3.1.2 Procedure

MRAMS was initialized with MGCM output and then run with all five grids for nearly three sols (approximately 230,000 seconds). The dynamical timestep used on grid 1 was nine seconds, while that of the remaining four grids was 4.5 seconds. On Earth, with comparable gridspacing, a timestep of 60 to 90 seconds would likely be satisfactory. The small timestep required for the two coarsest grids on Mars is due to the presence of the Tharsis volcanoes (i.e., extreme, complex topography) on those grids. The radiation timestep used was 300 seconds. This value was chosen objectively based on prior experiments. Analysis files were written to disk every 20 Mars–minutes (about 1233 seconds). The starting season was approximately $L_s = 143$ degrees, which is the latter portion of the Northern Hemisphere summer. This season was chosen partly because synoptic–scale disturbances should be weak at both MPF and VL1 sites (allowing for repeatability sol after sol), and secondly, MPF landed during this season, so the model results should compare well with lander measurements. The simulation was begun at 0730 UTC (about 0516 LST at the MPF site — just before local sunrise). This time was chosen because the MGCM initial condition is probably more accurate at night than during the day (due to the fact that the nocturnal atmospheric structure evolves primarily via radiative processes which are likely well–captured by the MGCM; during the day, however, convection shapes the lower atmospheric structure, and is likely poorly parameterized in the MGCM).

3.2 Results

3.2.1 Mars Pathfinder Landing Site

Figure 5 compares MPF lander temperature measurements, MRAMS air temperature at the same level (1.27 meters), and MRAMS surface temperature. The MPF lander data is taken from the first several sols of the landed mission. The MRAMS air temperature has been extrapolated from the lowest model level (14.4 meters) using Monin–Obukhov surface layer scaling laws originally developed for Earth's atmosphere. It is unknown whether these laws are strictly valid on Mars, but for the present purposes it is assumed that they are. The air temperatures compare quite well, except in the late
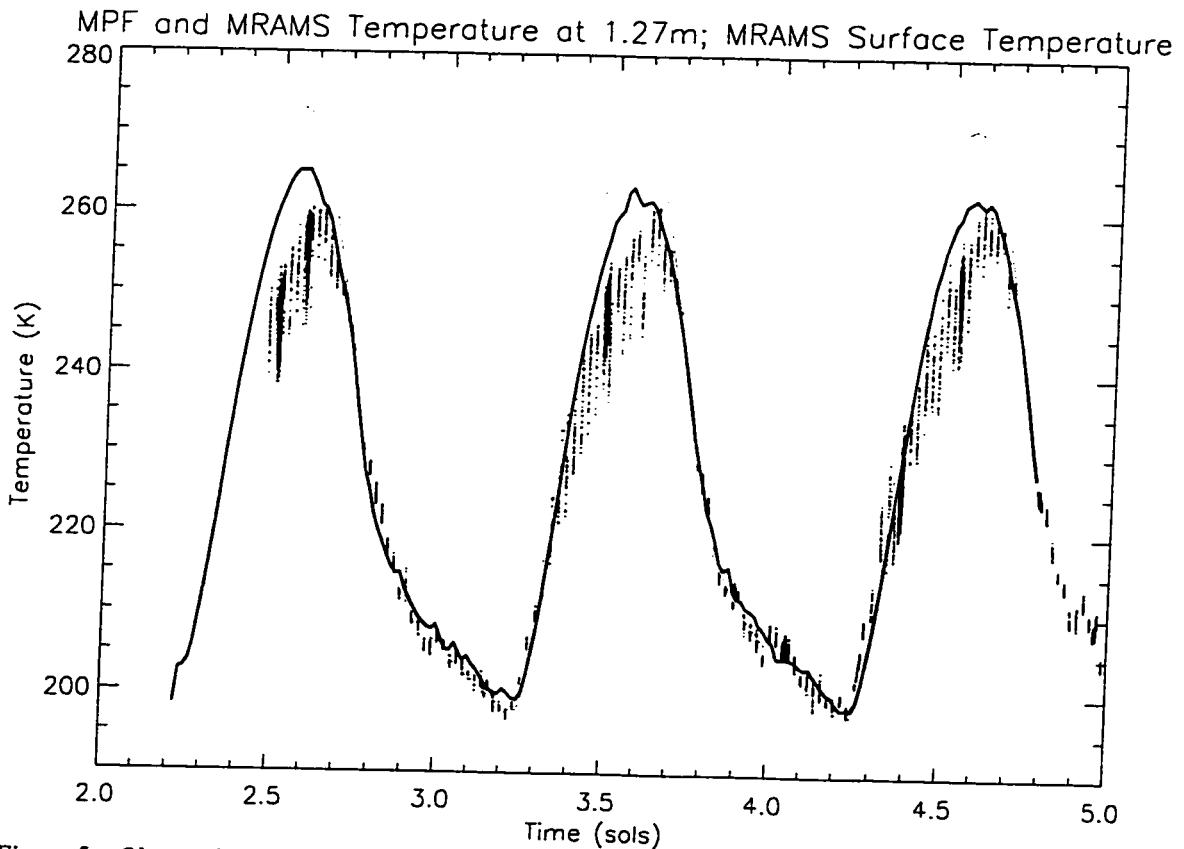
Figure 5. *Observed vs. modeled MPF temperature comparison.*

MRAMS surface temperature (solid gray line), MRAMS 1.27 m air temperature (solid black line), MPF observations (black points); time axis is in LST

30

morning and early afternoon when MRAMS is too warm. This may be due to inaccurate values of regolith properties, but may also be related to the active daytime convection at this location and season. Accordingly, it may hint at a turbulent mixing parameterization problem (i.e., the 2.5 order closure scheme of Mellor and Yamada may not represent the effects of Martian convection well). Also notice the significant temperature
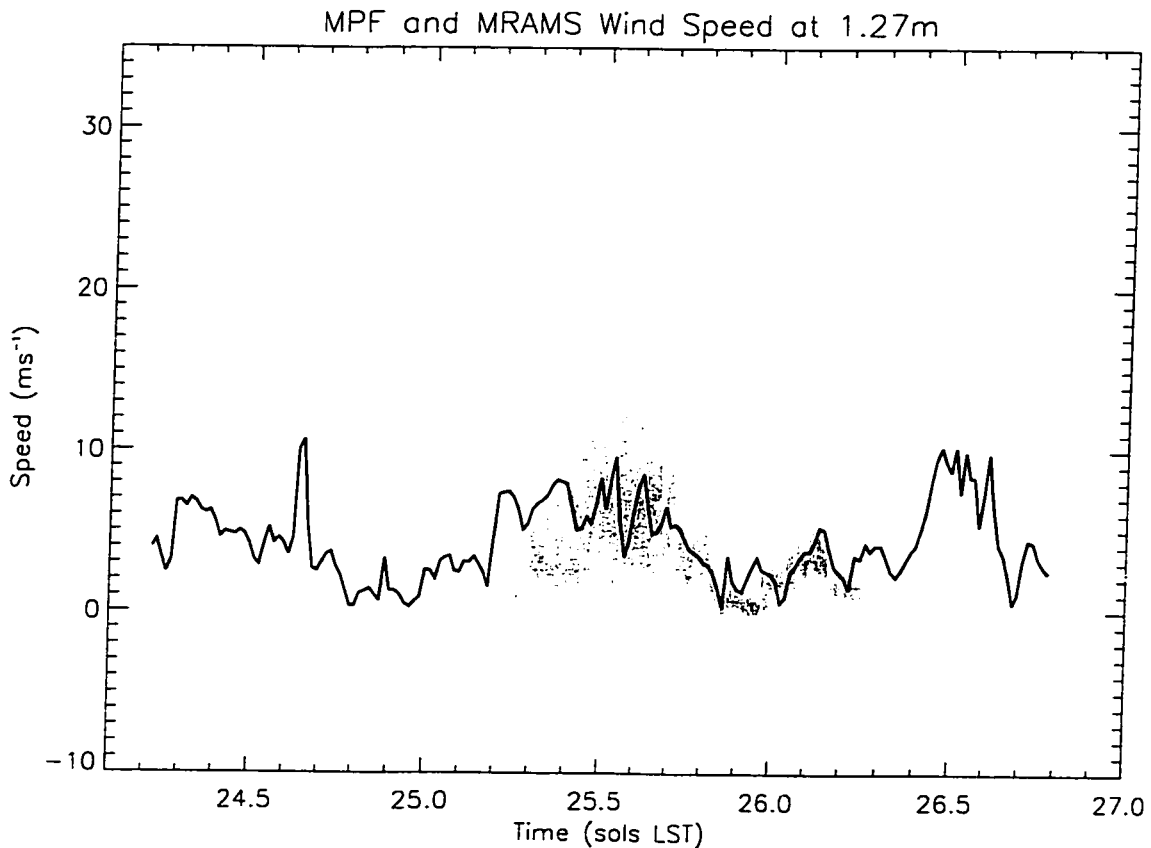
Figure 6. Observed vs. modeled MPF wind speed.
MRAMS wind speed (solid black line), MPF observations (black points)

perturbations at night, evident in both the lander data and MRAMS. These appear to be sporadic periods of warm advection from relatively nearby high thermal inertia regions.

Wind speeds are compared in Figure 6. The MPF wind data presented (courtesy of Dr. J. Murphy, NMSU) are from the Sol 25/26 "Presidential Series" period of high–

31

frequency data sampling. Only simple linear extrapolation has been used to reduce the

MRAMS wind speed from the lowest model level height to 1.27 meters. Many of the

extreme values (and all negative values) in the MPF data are likely miscalibrated data

points. However, these bad data account for only a small fraction of the total dataset,

especially at night. In general, the MRAMS values compare well to the MPF data, with a

daytime maximum and nocturnal minimum. There are local maxima at night in both

datasets that appear to be due to the passage of katabatic fronts originating from

surrounding, but not necessarily local, elevated terrain (some source regions are over

1000 kilometers distant). It is important to note that the modeled wind speeds appear to

be less repeatable sol after sol than temperature, for example. This likely occurs because
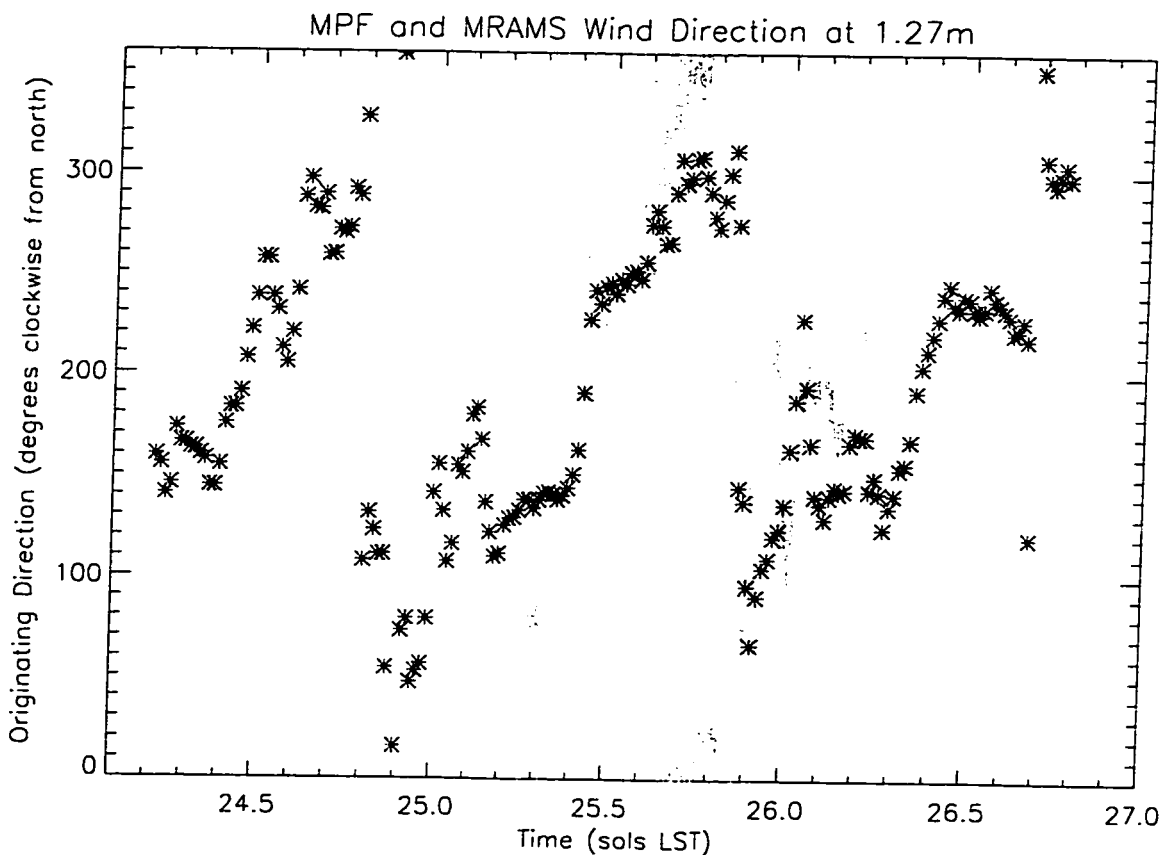

Figure 7. Observed vs. modeled MPF wind direction.

MRAMS wind direction (black asterisks), MPF observations (gray points)

the near–surface air temperature on Mars is very strongly controlled by radiative processes alone, whereas many complex and nonlinear processes can affect a moving fluid (including model approximations of topography, physics, etc.).

Figure 7 compares MPF wind direction data to MRAMS results. Note that MRAMS, when run at mesoscale resolution, cannot resolve small–scale turbulent motions that produce the high degree of variation in the observed wind direction at all times of sol. A small portion of the variation is also due to the above–mentioned miscalibration of some of the MPF wind data. However, MRAMS generally compares well to the MPF data, with a nearly full rotation of wind direction throughout a sol. The largest systematic discrepancy occurs in the afternoon and early evening, when the MRAMS wind direction stays relatively constant at about 300 degrees, whereas the observed wind direction continues to change at a constant rate. Wind direction is affected considerably by the passage of atmospheric tides. Therefore, this difference may be due to a known problem of anomalously low–amplitude tides in the MGCM solution used to provide boundary conditions.

3.2.2 Viking Lander 1 Landing Site

The extrapolation and interpolation of MRAMS data to the VL1 location was performed in an identical fashion as at the MPF location. All MRAMS data presented in this section are from grid 3 of the simulation, which has a horizontal gridspacing of 60 kilometers.

Figure 8 compares VL1 temperature measurements, MRAMS air temperature at the same level (1.6 meters), and MRAMS surface temperature. The VL1 data are from

33

the same season as the MRAMS simulation, but are only available binned and averaged over every 1/25 of a sol. Much of the high frequency variation seen in the MPF dataset is therefore not present in the VL1 dataset solely because of the averaging procedure and not because it does not exist in reality. MRAMS clearly has a warm bias and slight lag in phase compared to the VL1 measurements. This is likely partly due to having a higher topography height in MRAMS than in reality, as the VL1 site lies quite near a large topographic gradient, and the relatively coarse spatial resolution of grid 3 likely smears that gradient out over the VL1 site. Also due to the coarseness of grid 3, thermal inertia and albedo are likely not exactly equal to their actual values at the VL1 site. As
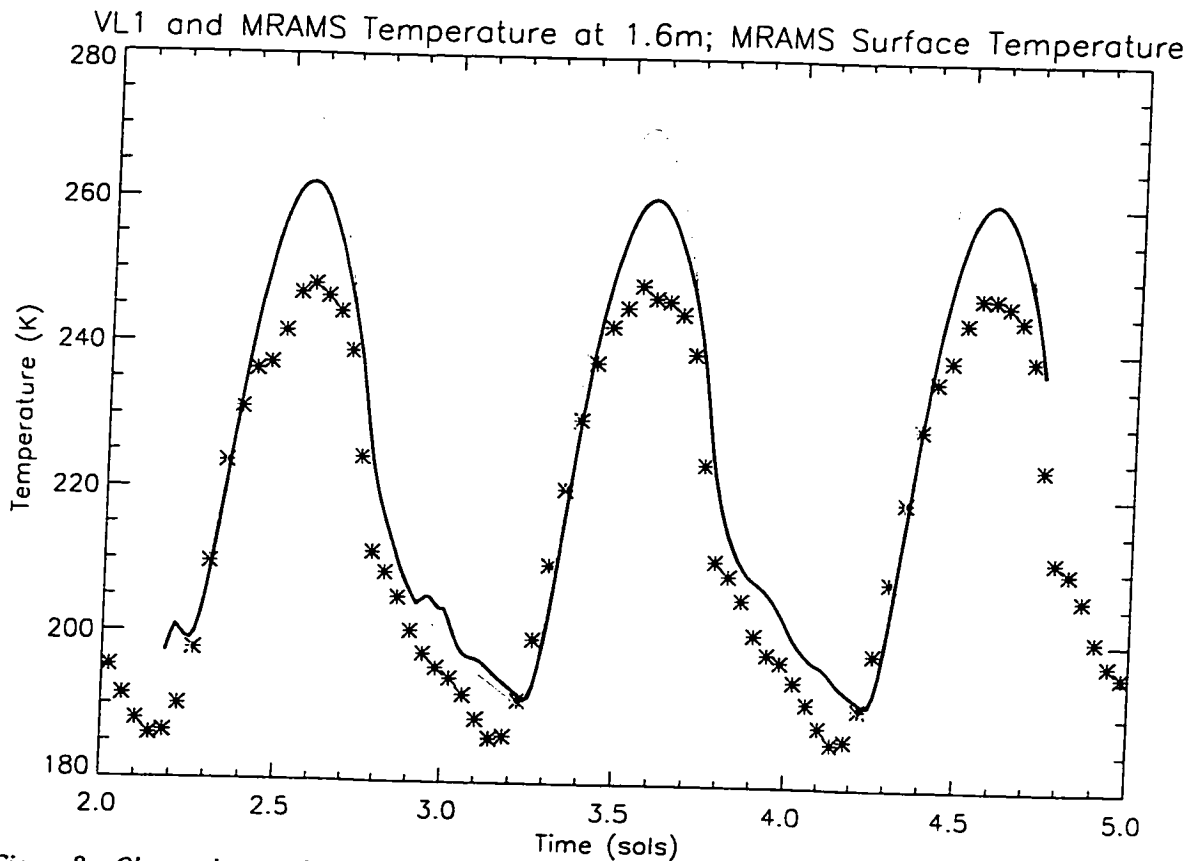
Figure 8. *Observed vs. model VL1 temperatures.*

MRAMS surface temperature (solid gray line), MRAMS 1.6 m air temperature (solid black line), VL1 observations (black asterisks); time axis is in LST

suggested in the MPF site comparison above, there may also be an issue with the turbulence parameterization.

Observed versus modeled wind speeds at the VL1 site are compared in Figure 9. Notice how neither MRAMS nor the VL1 measurements are the same sol after sol. MRAMS has systematically higher wind magnitudes, with extrema that are out of phase, compared to VL1 observations. However, the gross features of a daytime maximum and a nocturnal minimum are successfully reproduced. Much of the above differences is likely attributable to the unrealistic local topography, thermal inertia, and albedo gradients (which produce erroneous horizontal pressure gradients) present on the
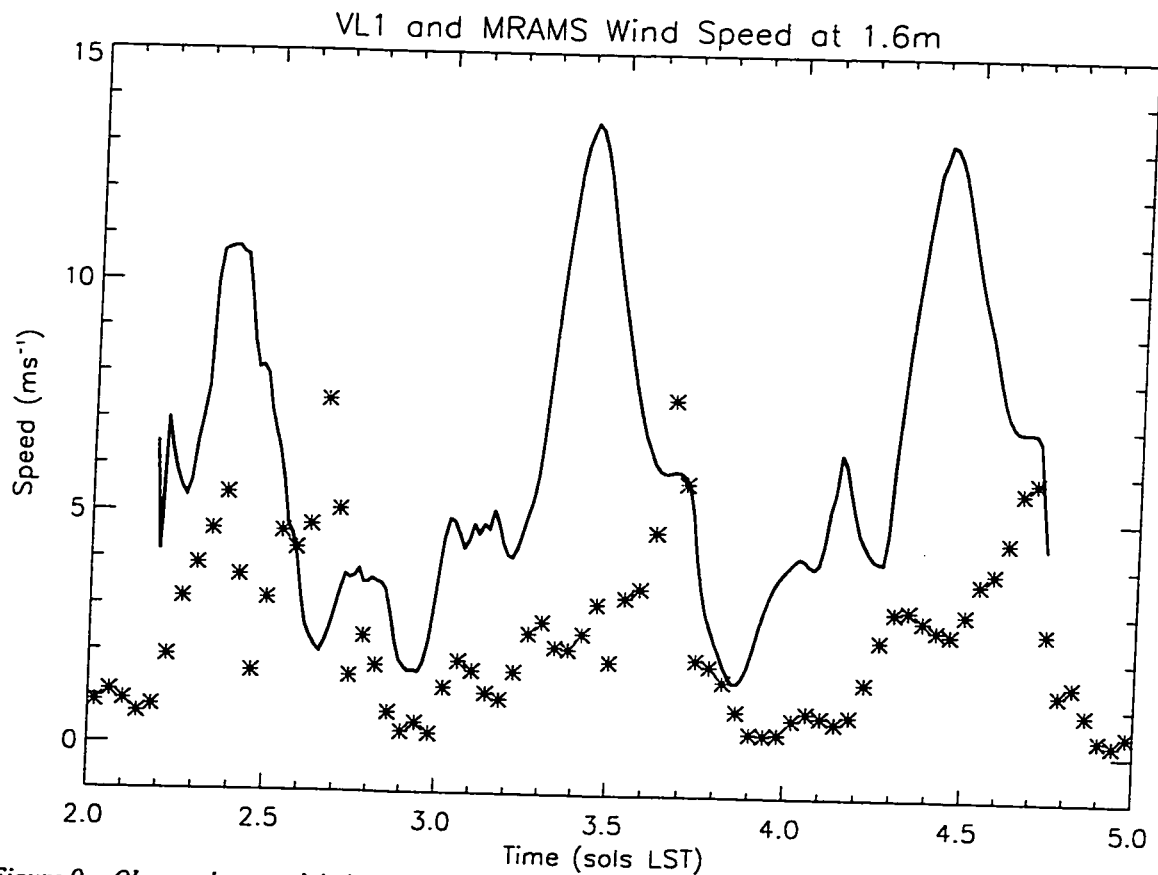
Figure 9. Observed vs. modeled VL1 wind speed.

MRAMS wind speed (solid black line), VL1 observations (black asterisks)

relatively coarse grid 3.

Figure 10 shows the MRAMS and observed VL1 wind direction. Again note that both the observed and modeled wind direction pattern changes significantly from sol to sol. MRAMS generally compares well to the VL1 measurements, especially on the third sol. An interesting, but puzzling, feature is the full rotation of the MRAMS wind direction on the second sol. The fact that the MRAMS wind direction on a relatively coarse grid compares so well to observations is either a coincidence, or more likely, the actual local and regional topography and surface property gradients that strongly control the wind are oriented in a direction similar to that of the grid 3 gradients of the same quantities.
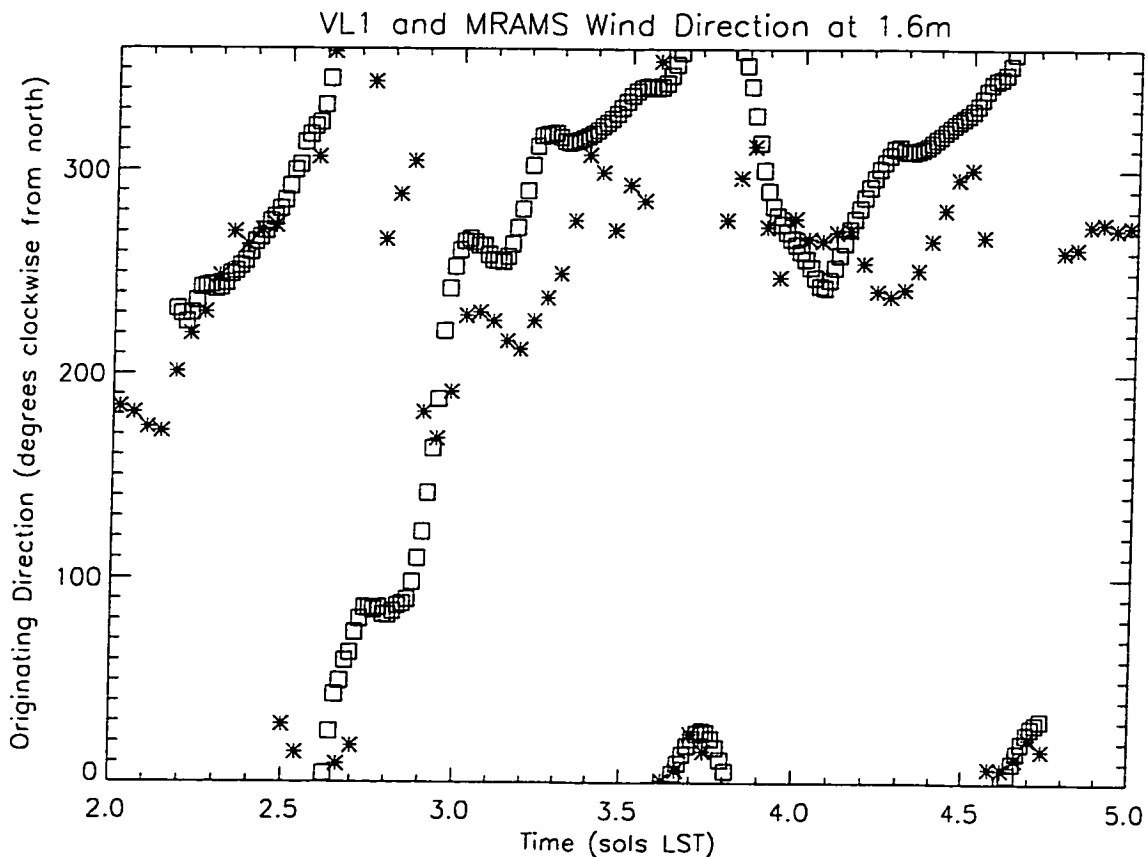
Figure 10. Observed vs. modeled VL1 wind direction.

MRAMS wind direction (black squares), MPF observations (black asterisks)

4. LES SIMULATION

4.1 Simulation Design

4.1.1 Setup

Two separate simulations were performed at different horizontal and vertical resolutions. This was done in order to better understand the impact of model gridspacing on the resulting solution, to attempt to resolve the life cycle of dust devils more clearly, and to elucidate the characteristics of the flow at and during the onset of ABL convection. Both simulations were initialized in exactly the same manner, and used the same model physics and parameterizations. However, due to finite time and computational resources, the computational grids of the simulations were not the same size, nor were they integrated over the same period of time.

The computational grid of Simulation 1 (hereafter referred to as S150) is 24 × 24 kilometers in the horizontal and approximately 9.5 kilometers deep in the vertical. The horizontal gridspacing is 150 meters, and was chosen based on earlier two– and three– dimensional trial runs that indicated this value to be satisfactory for modeling the largest CBL eddies. The vertical grid was gradually stretched with height, with a first layer thickness of 4 meters (lowest level at about 1.9 meters AGL), increasing to a maximum of 225 meters (1.5 times the horizontal gridspacing, in order to keep the bulk of the three–dimensional computational grid approximately isotropic) aloft. These dimensions require 160 × 160 × 61 (1,561,600) grid points. The rationale for choosing the above grid dimensions is that Mason (1989) postulated that a grid at least 3.2 times the width of an individual convective cell was necessary to properly represent CBL statistics. Based

37

on earlier tests (which suggested that Martian convective cells were 7 to 8 kilometers wide) and computer limitations (both memory/storage and computational time needed), the above dimensions were chosen — with the aim of having significant CBL statistics and realistic CBL structures and dynamics.

The computational grid of Simulation 2 (hereafter referred to as S30) is 6 × 6 kilometers in the horizontal and approximately 2.3 kilometers deep in the vertical. The horizontal gridspacing is 30 meters. The vertical grid is gradually stretched with height, with a first layer thickness of 4 meters (lowest level at about 1.9 meters AGL), increasing to a maximum of 45 meters aloft. These dimensions require 200 × 200 × 61 (2,440,000) grid points.

All grids were made strictly Cartesian (i.e., no attention was paid to planetary curvature). Flat topography was assumed (i.e., topography was set to zero meters everywhere). The grids were centered at the Mars Pathfinder landing site at the southern edge of Chryse Planitia (19.33°N, 33.55°W) in order to compare with actual landed data. Thermal inertia and albedo were set to be constant over the entire grid (set to representative values from the MPF site: thermal inertia = 384.5 J K^{-1} m^{-2} s$^{-0.5}$, albedo = 0.197). The surface aerodynamic roughness length used was 0.03 meters. A static dust distribution was used, with a dust optical depth of 0.3 on a pressure surface of 6.1 hPa.

4.1.2 Procedure

Cyclic (sometimes termed periodic) lateral boundary conditions were used for both simulations. This type of boundary condition was primarily chosen because there are no three–dimensional ABL observations for Mars to use as boundary conditions and

an appropriate mesoscale simulation to provide boundary conditions was judged to be too time–intensive to undertake at present. Moreover, it is likely a reasonably good approximation to the situation in the northern plains of Mars. Assuming a mean wind of 5 m s^{-1}, the equivalent domain simulated during a solar convective day of 10 Mars–hours (about 36,990 seconds) is basically a flat plain 200 kilometers wide with atmospheric convection occurring everywhere. A plain of such a size is easily found near the MPF landing site. At the model top, a Rayleigh friction layer 5 vertical grid points thick was used with a dissipation time scale of one Mars–hour.

The Coriolis force was kept spatially constant (set to the value at 19.33°N) for both simulations. The full regolith model of MRAMS was used, as well as the full radiation code. However, the solar zenith angle was treated as if the entire grid was a single point (the areographical location of the grid center). A radiative timestep of 30 seconds was used in an attempt to capture the radiative changes induced by the largest convective ABL eddies (since they may significantly alter the temperature/pressure profile over that period of time). The starting season was approximately $L_s = 143$ degrees, which is the latter portion of the Northern Hemisphere summer. This season was chosen partly because the synoptic–scale disturbances should be weak at the MPF site (allowing for atmospheric repeatability sol after sol), and secondly, this was the season that the Mars Pathfinder spacecraft landed at, so the model results should compare well with the landed observations.

Both simulations were initialized with a single sounding from a previous mesoscale simulation of the MPF site. The initial fields were thus horizontally homogeneous. Only the sounding temperature and pressure profiles were used. Wind

components were specified as follows: $w = 0$ m s^{-1}, $v = 0$ m s^{-1}, and $u = 5$ m s^{-1}. This choice was made in order to examine the intrinsic structure (i.e., the weakly sheared structure) of the convective boundary layer on Mars, but have a slight amount of mean wind in one direction to move the convective cells/phenomena across the domain (which adds realism) and concurrently examine some of the effects mean wind has on the structure of the convective ABL. The horizontally homogeneous potential temperature field from the sounding was randomly perturbed by up to ± 0.1 K at the lowest model level in order to provide a slight amount of inhomogeneity to foster the onset of resolved convection. Both simulations were started at 0810 UTC (about 0556 LST), which is just after the local sunrise, in order to simulate the entire convective ABL evolution (achieved only in S150).

A dynamical timestep of 2 seconds was required to keep S150 numerically stable after resolved convection initiated, due to large vertical velocities across the relatively thin model layers near the surface. The model saved a fully three–dimensional snapshot of all prognostic variables every 300 simulated seconds. S150 was halted at 2020 UTC (1805 LST, 45000 seconds after start) after the ABL convection had almost completely dissipated.

A dynamical timestep of 1 second was required to keep S30 numerically stable. Model output occurred every 180 seconds. S30 was halted at 1349 UTC (1134 LST, 20880 seconds after start) after it was judged that the convective cells were becoming too large for the grid.

4.2 ABL Results and Discussion

4.2.1 Spatial and Dynamic Structure

Loss of momentum to the ground (due to friction) quickly creates near–surface speed shear in the initially vertically homogeneous wind profile. Soon after, the surface/air interface becomes warmer than the immediately overlying air (due to insolation), and atmospheric convection ensues (as the fluid's natural way to cool its lower boundary). The convective boundary layer initially evolves purely due to subgrid–scale (SGS) turbulence, evidenced by a deepening layer of greatly increased SGS turbulent kinetic energy (the only SGS quantity truly prognosed by the model) bounded by the surface and having no resolved spatial perturbations in wind, temperature, or pressure. When this SGS CBL attains a depth roughly equal to three times the horizontal gridspacing, resolved–scale convection initiates and immediately dominates the SGS processes (by an order of magnitude or more in terms of turbulent energy fluxes). This disparity between the magnitude of the SGS and resolved–scale fluxes at nearly the same time of sol appears to indicate a major difference between the atmospheres of Mars and Earth (see Section 4.2.2 for further discussion). The CBL depth at which this transition takes place is strongly a function of the strength of the horizontal SGS diffusion in the model. SGS diffusion was tuned to initiate resolved–scale convection at approximately three times the horizontal gridspacing since the model cannot properly treat turbulent eddies smaller than that (assuming the said eddies are all quasi–isotropic).

Resolved–scale convection begins as regularly spaced linear plumes of buoyant fluid aligned parallel to the mean shear vector (Figure 11). Note that updrafts and downdrafts occupy equal areas and have roughly equal magnitudes at this stage.
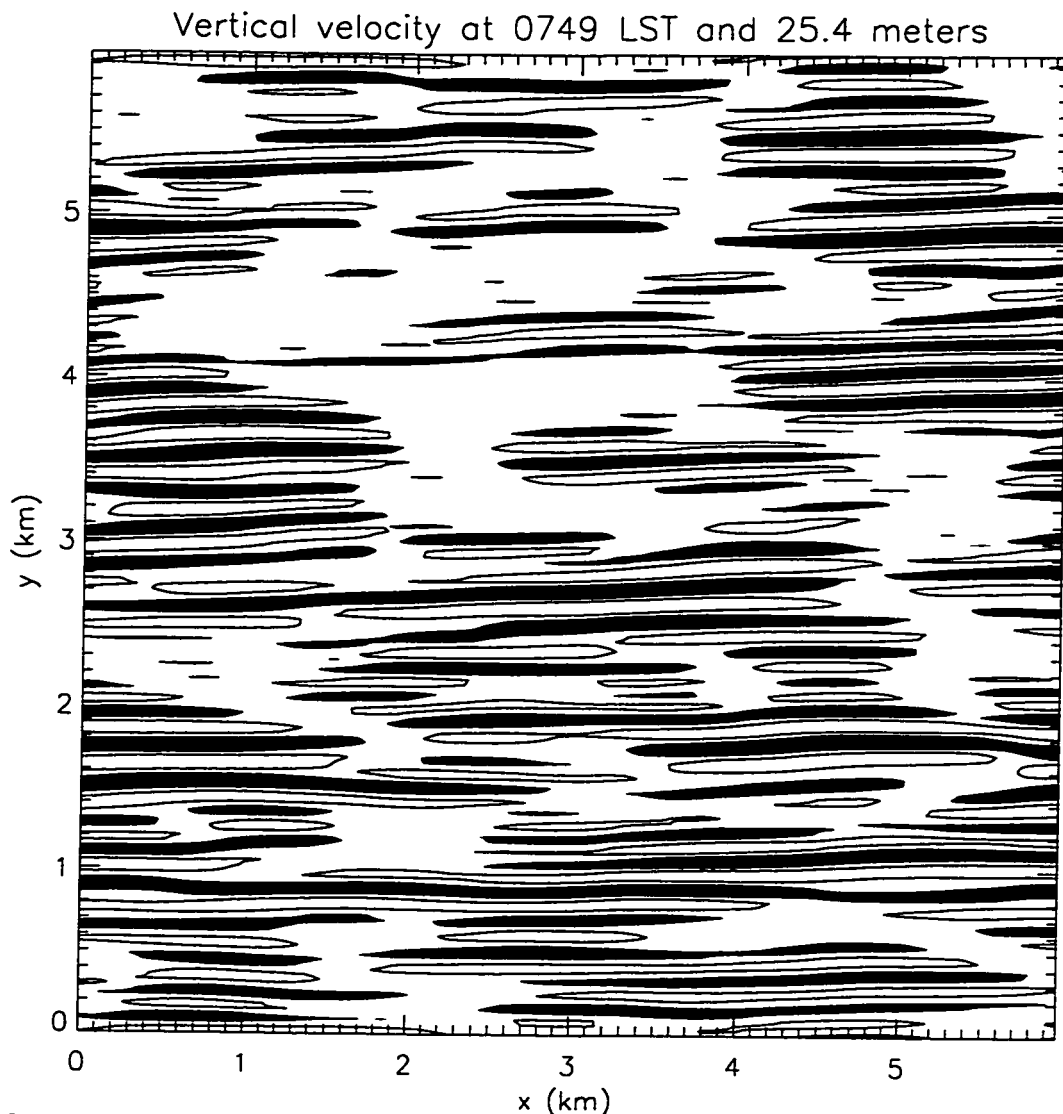
41

Figure 11. *Initiation of resolved–scale convection in S30.*

Contours are at –0.01 and 0.01 m s⁻¹; Filled areas are regions of upward (positive) motion.

However, in a near–surface (i.e., where there is vertical speed shear due to friction) environment dominated by buoyant forces, rather than shear forces, such linear structures are not stable. In order to maintain such symmetric structures, the three–dimensional fluid flow must somehow maintain an excruciating spatial symmetry, since any asymmetries will tend to amplify (because of momentum transport from aloft) or at least produce other asymmetries in the flow. In the model solutions, the first returning fluid

42

Vertical velocity at 0804 LST and 25.4 meters
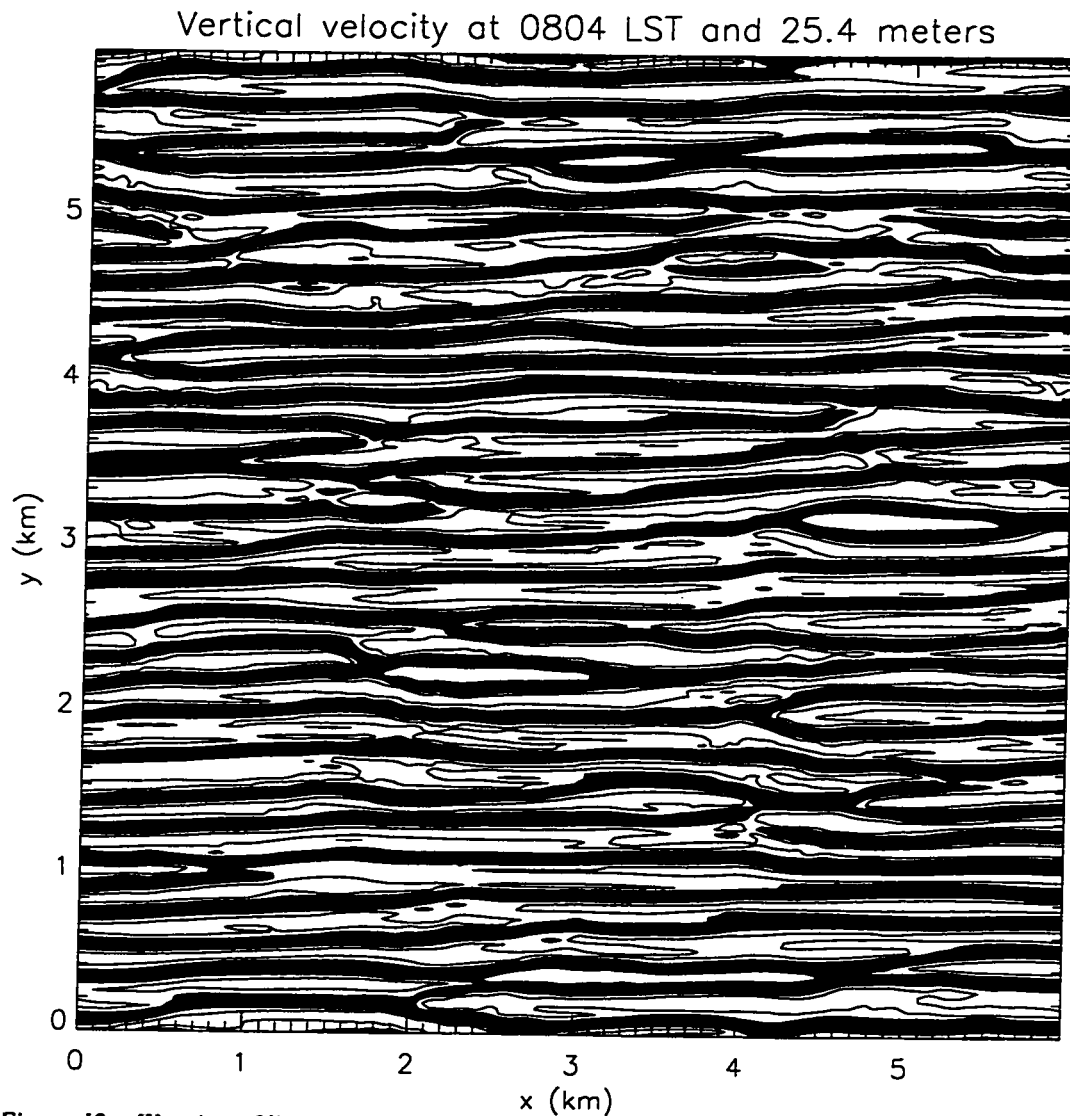
Figure 12. Warping of linear convective features in S30.

Contours are at −0.2 and 0.1 m s⁻¹; Filled areas are regions of upward (positive) motion.

(i.e., fluid that has journeyed upwards in one of the initial updrafts and has now returned to the surface in a downdraft) exhibits spatial asymmetries in vorticity (generated along the updraft lines), momentum, and heat (perhaps in part caused by gravity wave interactions along the upper boundary of the CBL) that warps sections of the linear updraft/downdraft structures in directions roughly perpendicular to the mean shear vector. The warping causes sections of adjacent updraft structures to connect, forming

Vertical velocity at 0833 LST and 25.4 meters
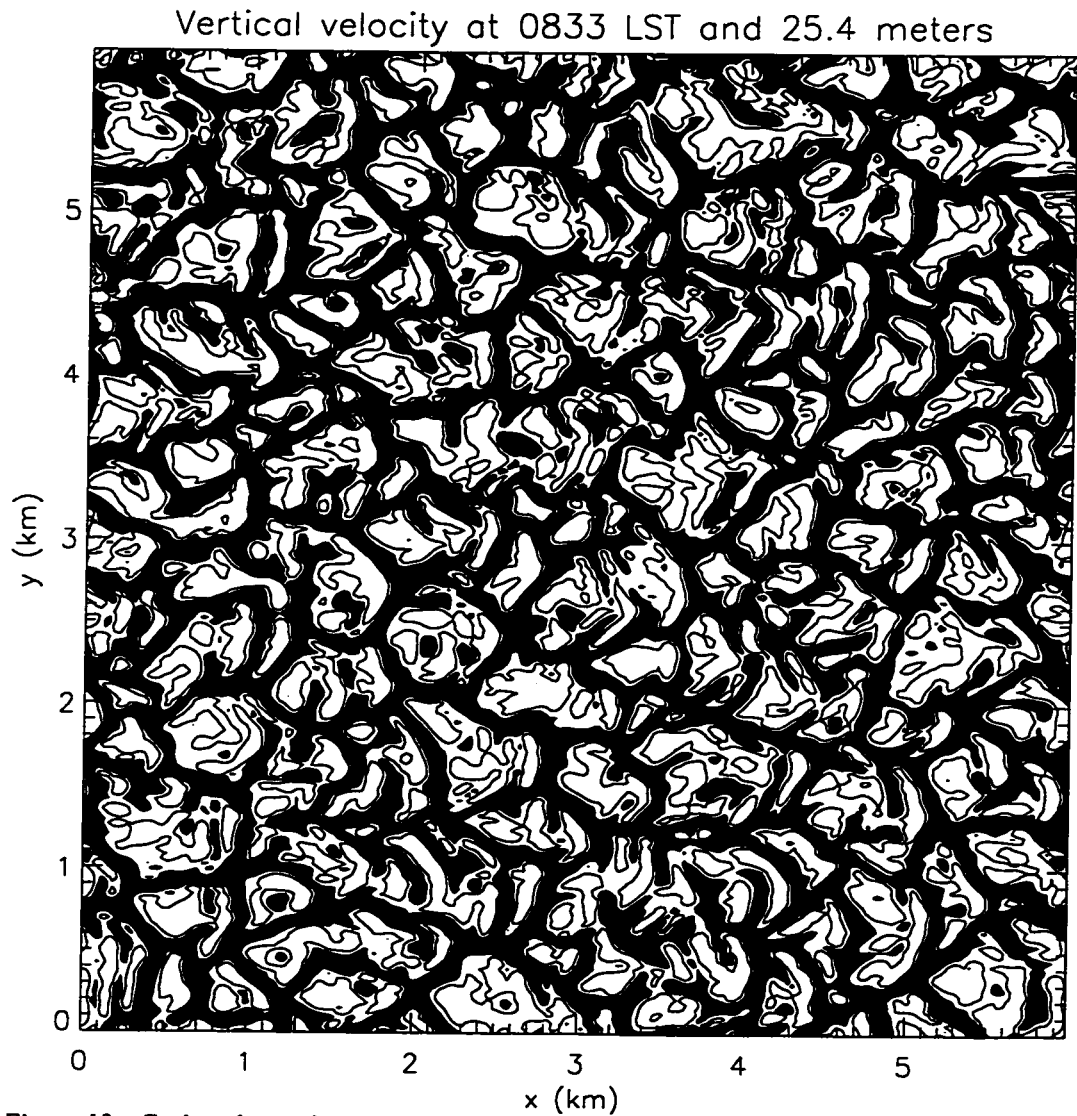
Figure 13. Early polygonal convective cells in S30.

Contours are at −0.2 and 0.1 m s⁻¹; Filled areas are regions of upward (positive) motion.

elongated, closed loop updraft structures. As this process continues, the linear updraft

structures give way to roughly elliptical structures (Figure 12), which in turn divide into

roughly circular structures (Figure 13). Also, downdrafts gradually encompass much

more area and become weaker than updrafts. Finally, updraft strength increases

dramatically during this period, as insolation, and thus the heating of the lower boundary

of the atmosphere (most importantly due to absorption of upwelling infrared radiation,

and secondarily due to conduction from the surface) increases. The shape of the approximately circular convective structures, or cells, is often more aptly described as polygonal (chiefly quadrilateral, pentagonal, and hexagonal). These polygonal cells persist throughout the remainder of the solar convective day.

The structure of these polygonal convective cells is startlingly complex and efficient. Every cell side is shared with an adjoining cell, so that there is no surface area left unencompassed. The cell sides are composed of relatively narrow and intense updrafts, while the majority of the cell interior contains only broad, relatively weak downdrafts. The lowest several hundred meters of each cell interior is a region of divergent flow towards the cell sides. Embedded in this low–level flow are much smaller convective cells with a structure similar to their larger cousins. This smaller–scale convection, kept from growing larger by subsidence and shear due to descending air in the large–scale cell interior, serves to channel near–surface buoyant fluid from the interior of the cell outward to feed the larger–scale updrafts that make up the cell sides.

The next several figures display the instantaneous S30 vertical velocity on horizontal sections at different heights at a time of 1105 LST. Figure 14 shows the vertical velocity at a level of 1.9 meters above the surface. Note the abundance of fine–scale updraft structures at this level. The CBL structure at 25.4 meters is shown in Figure 15. The updrafts have now narrowed, strengthened in intensity, and become quite organized into small polygonal cells. These are the shallow updrafts which channel buoyant fluid to the large–scale updrafts. Ascending now to 259.1 meters, Figure 16 shows the large–scale convective cells. Note that updraft intensity in the cell sides is not uniform. At 889.2 meters (Figure 17) only the more intense updrafts remain. Strong

downward motion seen at this level is associated with the entrainment of stable fluid at the CBL top. At a level of 1204.2 meters (Figure 18), only the most intense updrafts remain (analogous to the "overshooting tops" of strong terrestrial thunderstorms). This is effectively the CBL top, and is a region of active entrainment. A north–south vertical cross–section (of vertical velocity) through the domain at the same time (at $x = 90$ in the horizontal sections) is shown in Figure 19. The proportions of this figure are 1:1 (i.e., no vertical exaggeration). Several deep updrafts are visible, along with shallow updrafts and the broad downdrafts.

The mean size of all scales of convective cells broadens continuously throughout the day. This occurs at a pace dictated by the current available insolation and vertical temperature and momentum structure of the atmosphere (i.e., the cells may broaden very rapidly if a marginally stable layer of the atmosphere lies above them or if a layer of heightened momentum aloft is encountered and is then brought down to the surface). The overall mechanism that causes the cells to broaden is simply conservation of mass (if there is more mass going up, there should also be more mass descending to take its place).
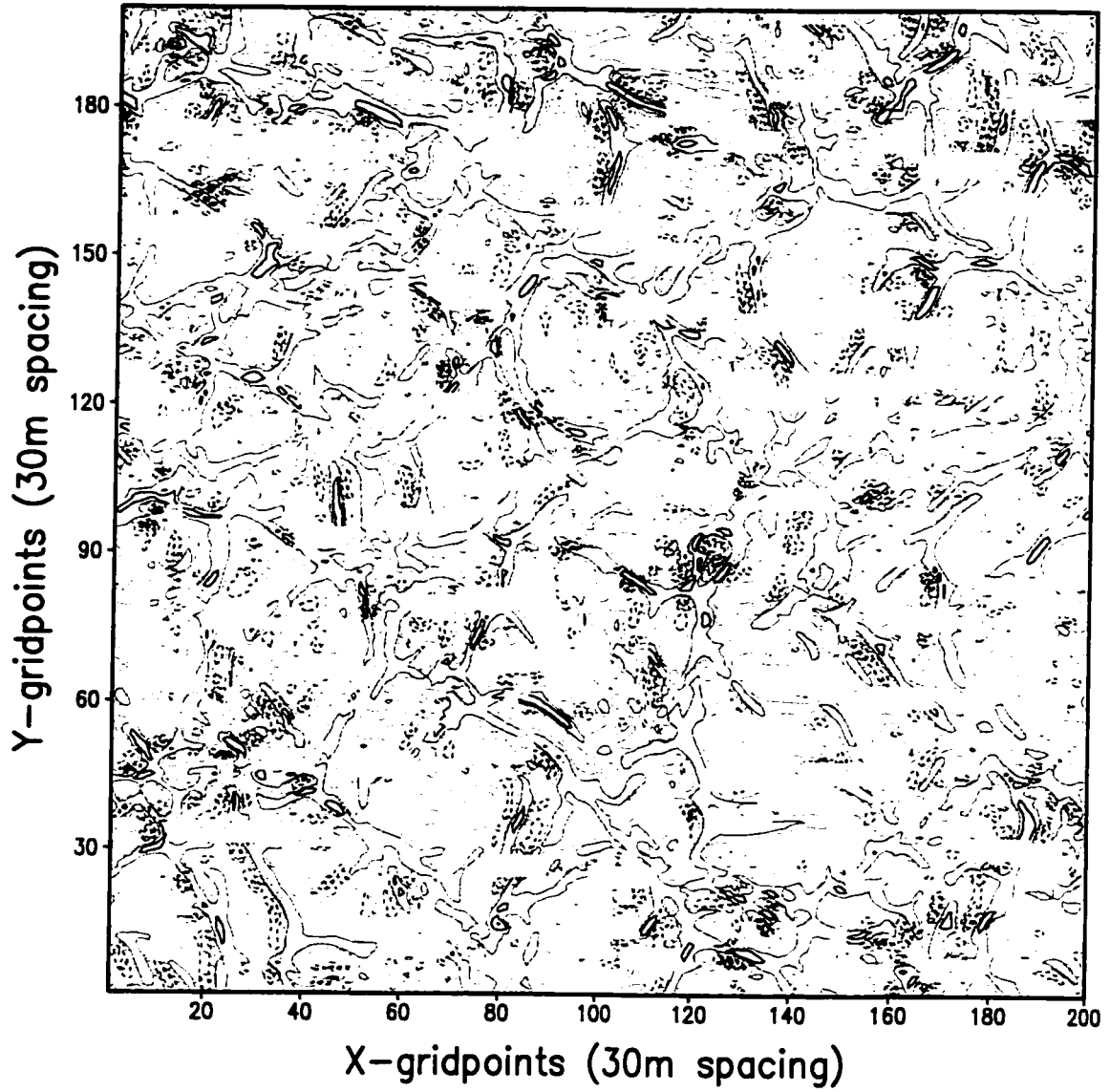
Figure 14.   S30 vertical velocity (m s⁻¹) at 1105 LST and 1.9 m

Dashed contours are negative.   Contour interval is 0.05 m s⁻¹

47
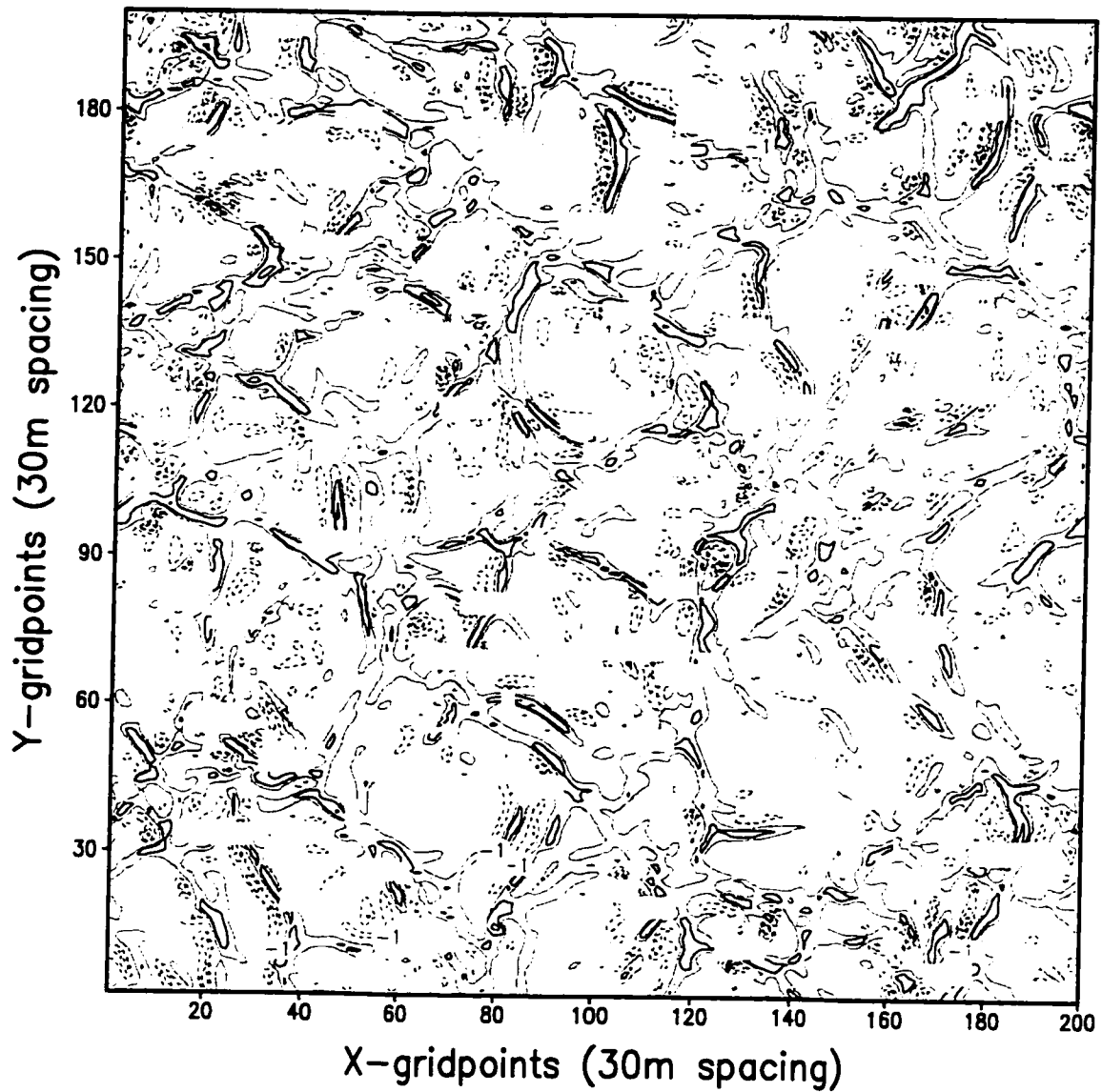
Figure 15. S30 vertical velocity (m s⁻¹) at 1105 LST and 25.4 m

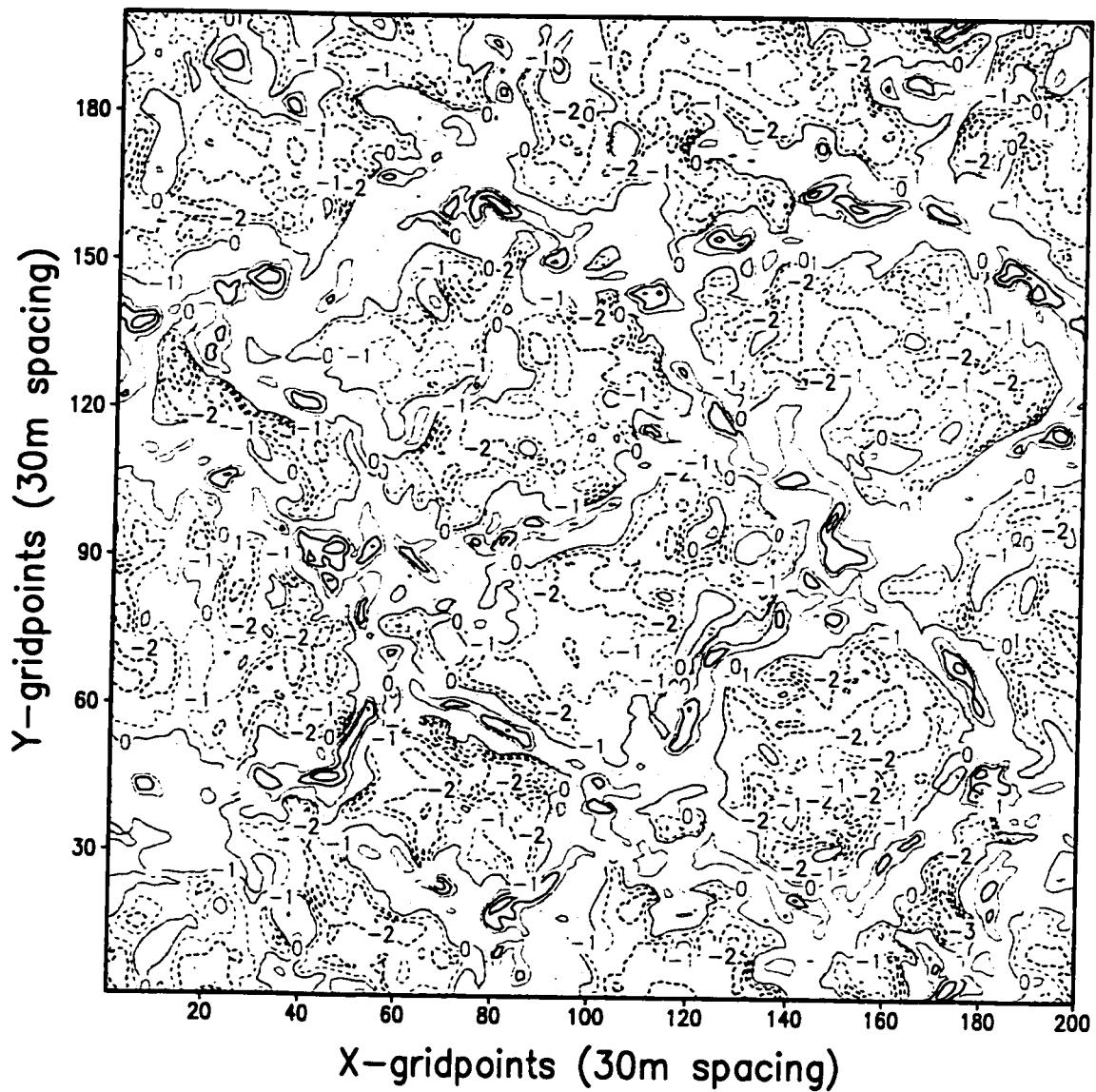*Dashed contours are negative. Contour interval is 0.5 m s⁻¹*

Figure 16. S30 vertical velocity (m s⁻¹) at 1105 LST and 259.1 m
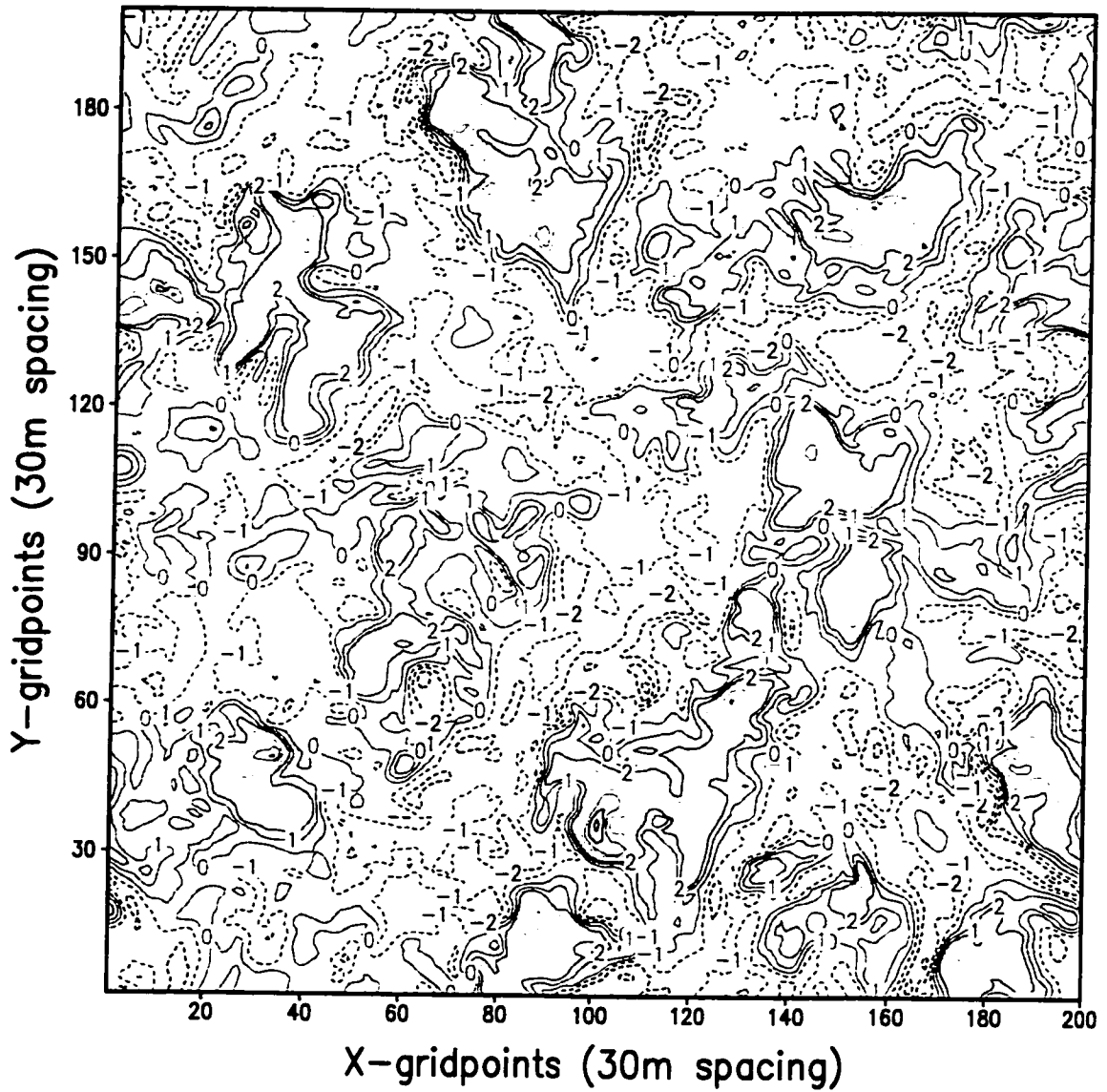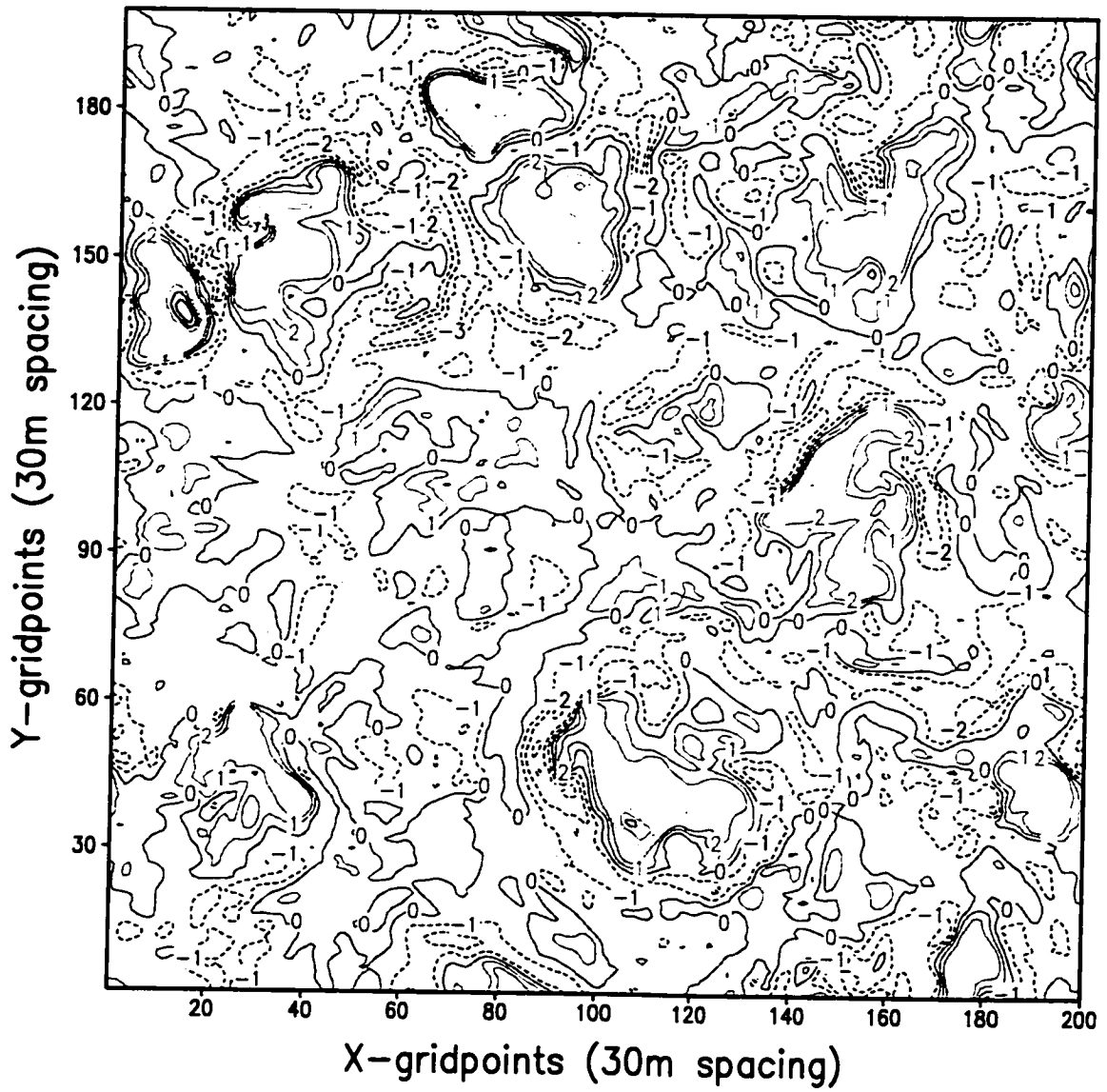*Dashed contours are negative. Contour interval is 1 m s⁻¹*

Figure 17. *S30 vertical velocity (m s⁻¹) at 1105 LST and 889.2 m*

Dashed contours are negative. Contour interval is 1 m s⁻¹

50

Figure 18. S30 vertical velocity (m s⁻¹) at 1105 LST and 1204.2 m

Dashed contours are negative. Contour interval is 1 m s⁻¹
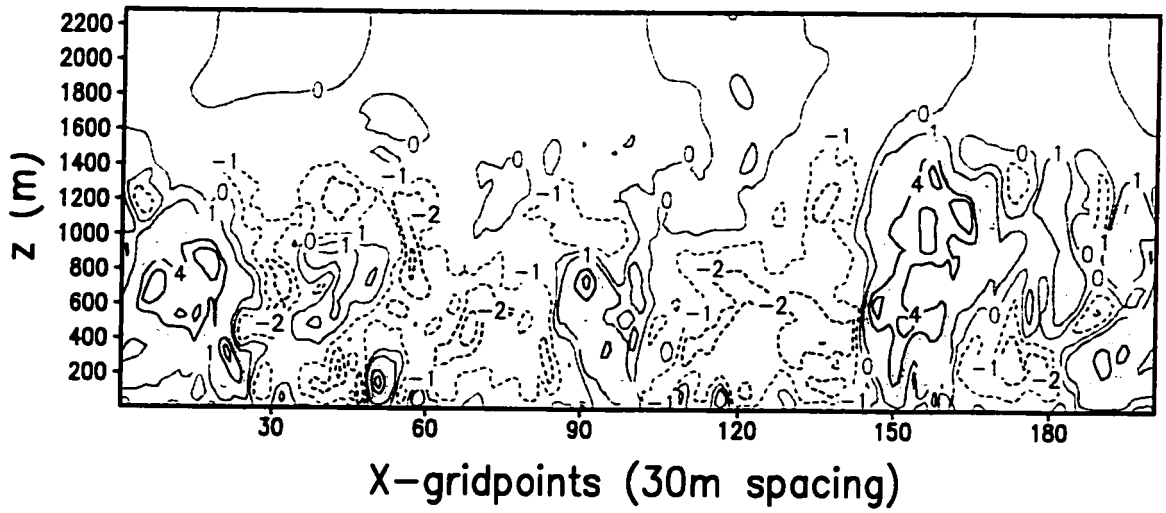
Figure 19. North–south section of S30 vertical velocity at 1105 LST and x = 90
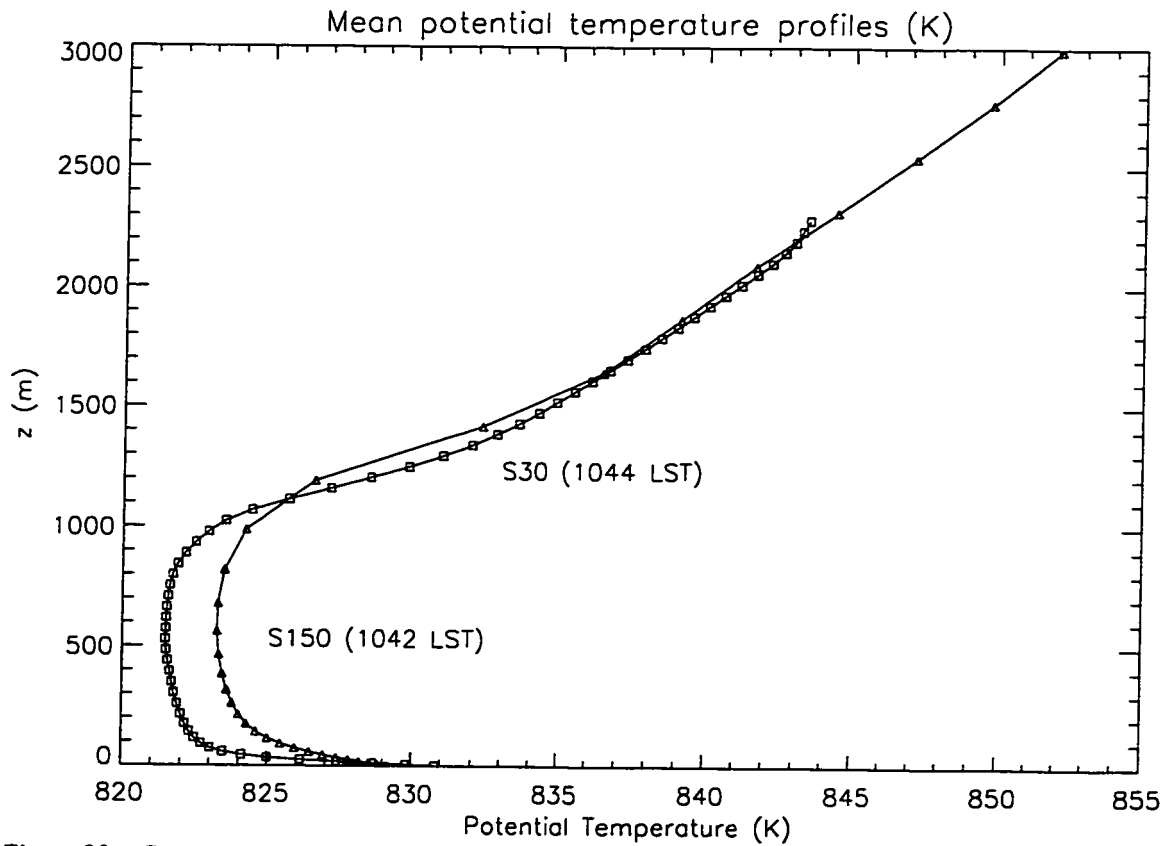
Figure 20. Comparison of mid–morning mean potential temperature profiles.

Figure 20 shows the mean (averaged over the entire horizontal domain) potential temperature profiles of S150 and S30 at roughly the same time in midmorning. S30 has developed a profile that is more than 2 K cooler than S150 throughout most of the CBL. S30 also displays the warmest potential temperature near the surface. The net result is that S30 is significantly more superadiabatic at low levels than S150. Also, note that S30 exhibits a slightly shallower CBL than S150. In both simulations, the mean profile is superadiabatic for fully half of the depth of the CBL. This is deceiving, however, since most of the domain is populated by downdrafts whose potential temperature profiles are nearly adiabatic throughout most of the CBL (Figure 21). The the extreme profiles of
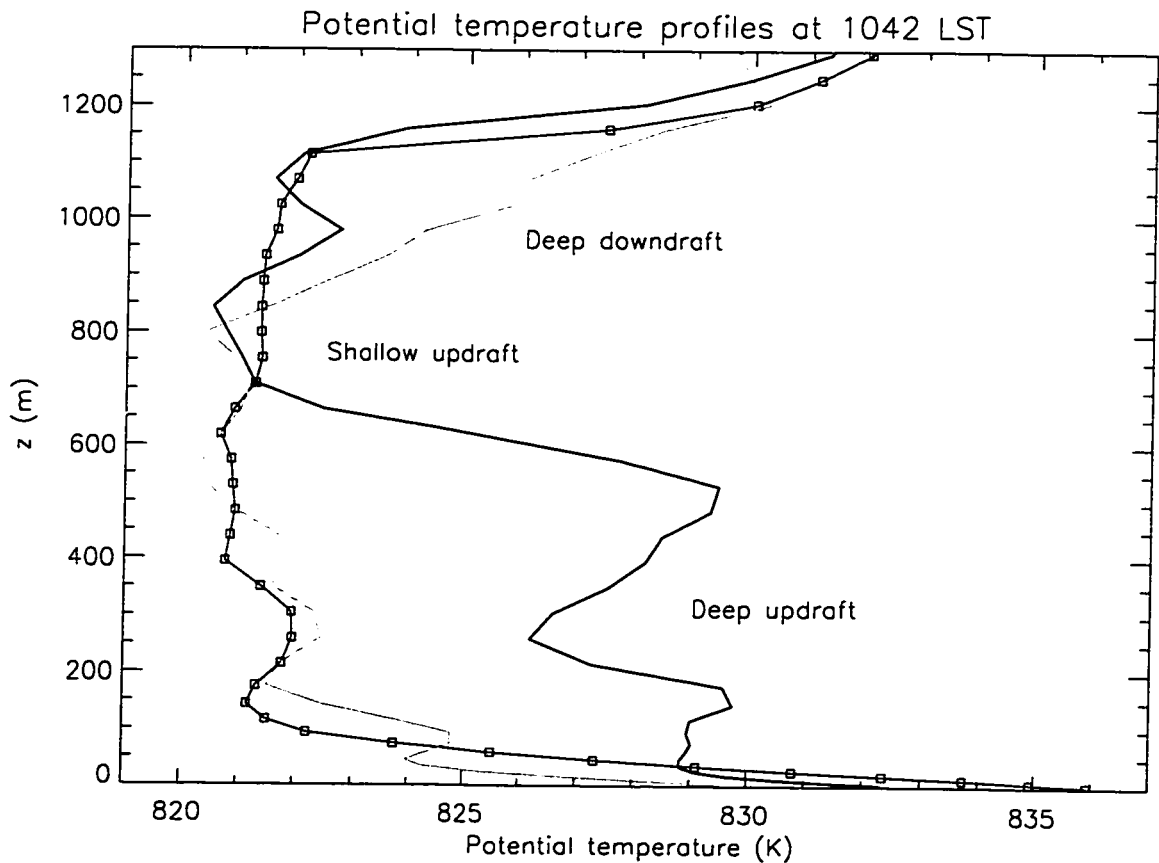

Figure 21. Several representative instantaneous potential temperature profiles.

the narrow and deep large–scale updrafts are solely responsible for the unusual shape of the mean profile. The profile through a shallow updraft in the interior of a convective cell differs from the downdraft profile only in that the lowest levels are very warm compared to even the deep updraft. Also note in Figure 21 that the CBL depth in the downdraft is significantly less than in the two updraft profiles. Finally, the shape of the deep updraft profile indicates that the buoyant fluid is able to rise relatively adiabatically and unentrained (i.e., without mixing much with cooler fluid) through much of the depth of the CBL.

4.2.2 Turbulent statistics

In light of the fact that the CBL is rife with many similar, ever–changing three–dimensional structures, it is instructive to compute a number of statistics about the flow (e.g., covariances, variances, skewness, mean profiles). For a detailed description of the statistical methods and assumptions used here, refer to Chapter 2 of Stull (1988). Such statistics provide a two–dimensional view (height and time) of the overall effects of the complex convective flows. All turbulent statistics presented here are computed as a single vertical profile for each model output time, with each profile point being assigned the average of that quantity over the entire horizontal domain at that level.

A time–height plot of the covariance of vertical velocity and temperature (a quantity proportional to the turbulent heat flux) from S150 is shown in Figure 22. Clearly, resolved–scale convection does not initiate in S150 until after 0930 LST. The entrainment zone above the CBL is plainly evident, growing deeper and more intense as the convective elements become larger and more energetic. The maximum value of 1.42
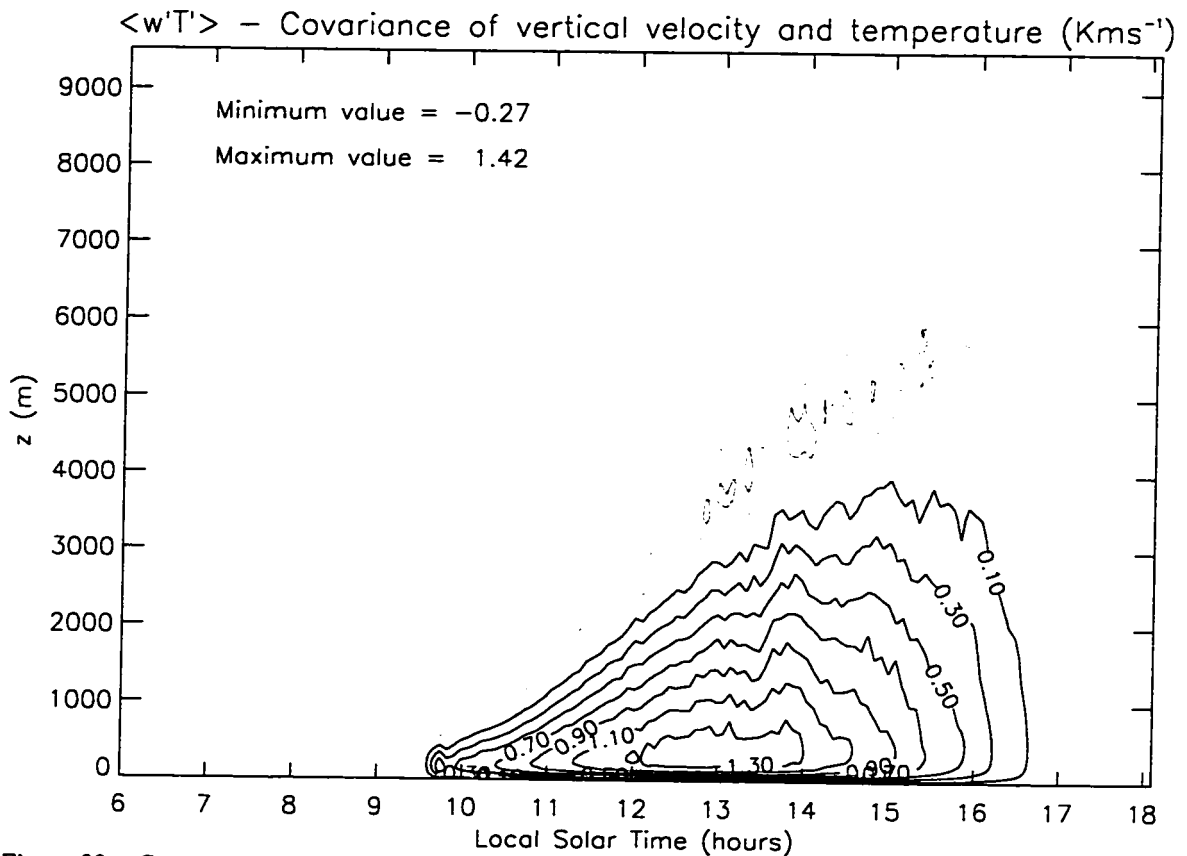
Figure 22. *Covariance of vertical velocity and temperature (S150)*

Contours are not all uniformly spaced. Gray contours indicate negative values.

K m s^{-1} is reached at 1300 LST (just after the time of maximum insolation), and is nearly

an order of magnitude greater than maximum values measured in terrestrial desert

atmosphere studies such as Schneider (1991). However, the maximum actual thermal

energy flux, which is obtained by multiplying the covariance by the air density and heat

capacity, is nearly an order of magnitude less than that on Earth, owing to the Martian air

density being nearly two orders of magnitude smaller than on Earth. Since Mars receives

approximately half the terrestrial amount of solar insolation, the Martian CBL *must* be

more vigorous and deeper than the terrestrial CBL, due to the fact that the Martian

atmosphere is so much less efficient at transporting heat. More intriguing is the presence
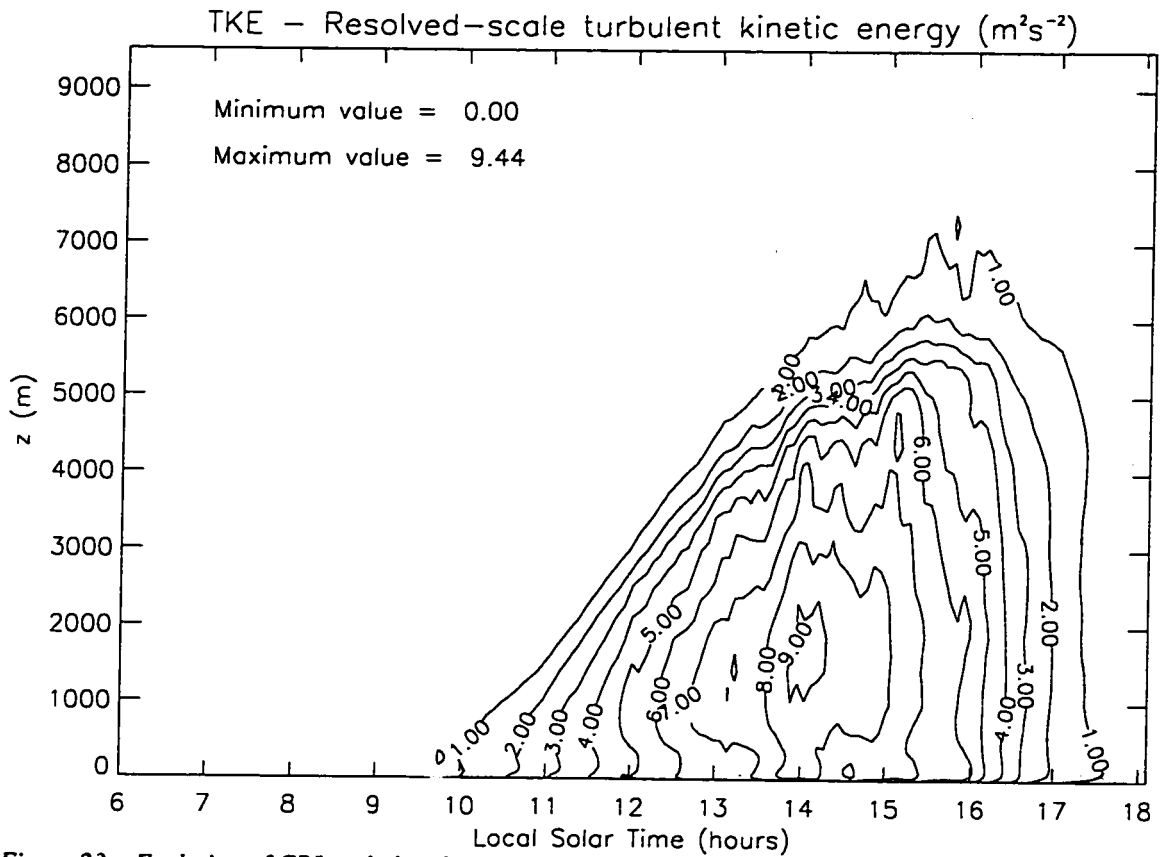
Figure 23. Evolution of CBL turbulent kinetic energy (S150)
Contours are not all evenly spaced.

in the mean statistics of what appear to be regular pulses of convective activity

(especially evident in the entrainment zone) that become more intense but less frequent

as the day passes. This suggests that all (or at least most) of the convective cells in the

domain are involved in a concerted (i.e., not random) cycle of overturning. Finally, the

amount of vertical heat transport diminishes gradually throughout the afternoon, until

convection collapses completely sometime after 1700 LST.

Resolved–scale TKE is shown in Figure 23. The maximum depth of the CBL,

when defined as the region of relatively high TKE bounded by the ground, is about 6 to 7

kilometers. The MRAMS TKE values are two to three times greater than in the typical

terrestrial desert atmosphere. The intensity of the CBL circulations is greatest at around 1400 LST. After 1600 LST, the CBL eddies rapidly lose strength and have effectively collapsed by 1730 LST. The majority of the turbulent kinetic energy in the Martian CBL is contributed by vertical motions, as evidenced by the large values of vertical velocity variance [TKE = 0.5*(<w'w'>+<u'u'>+<v'v'>)] shown in Figure 24. This is indicative

<w'w'> — Vertical velocity variance (m^2s^{-2})

Minimum value = 0.00
Maximum value = 11.51
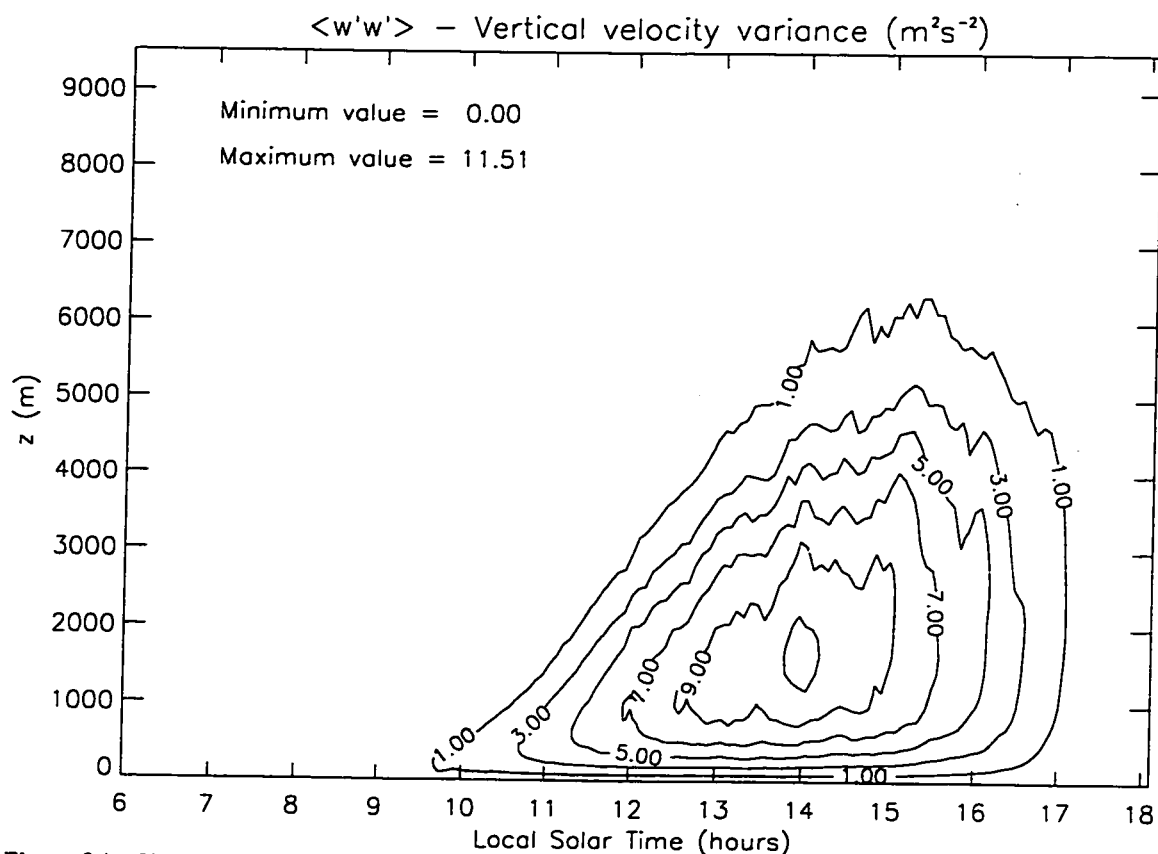
Figure 24. Vertical velocity variance (S150); contours are not all evenly spaced.

of the large–scale Martian convective eddies being strongly anisotropic (in intensity).

Figure 25 shows the vertical flux of horizontal momentum (the covariance of the horizontal and vertical velocities). The values of this statistic are slightly less than analogous measurements on Earth. The alternating positive and negative values are a puzzling feature, as they indicate periods of mean gradient and counter–gradient
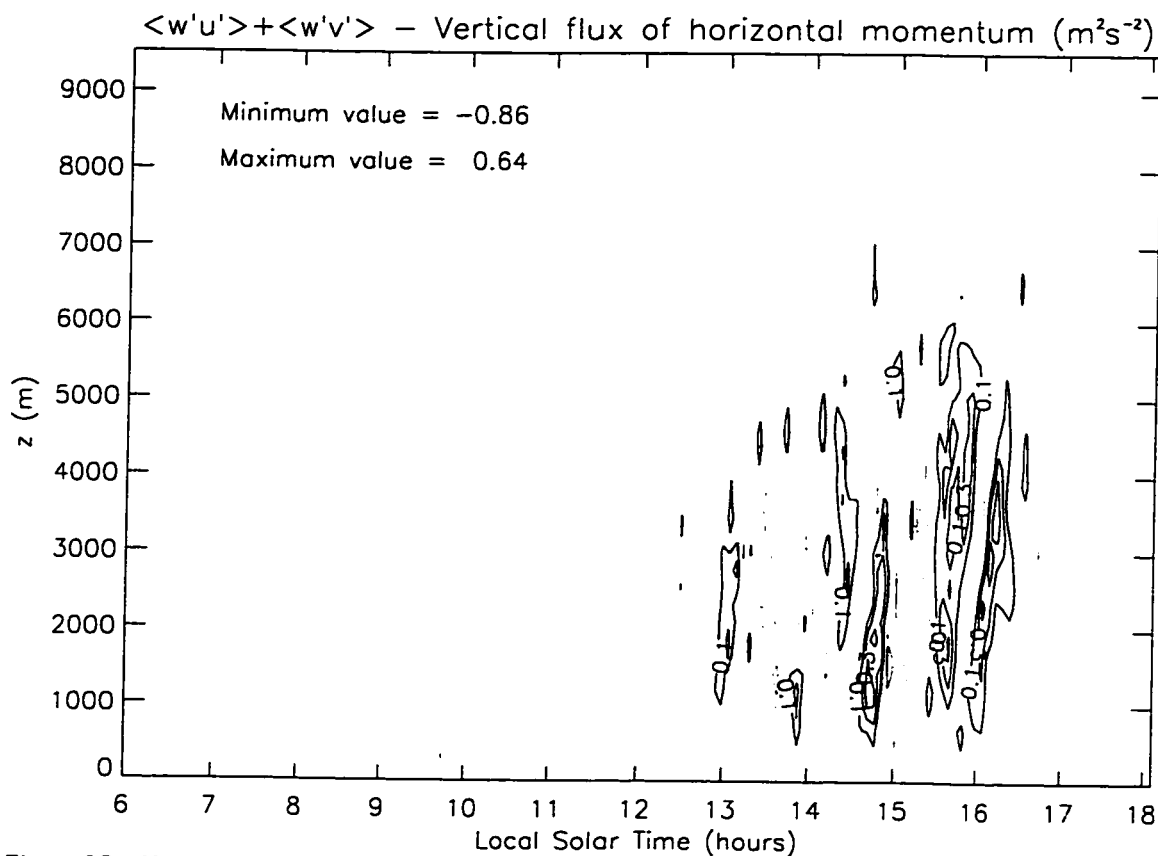
57

Figure 25. *Vertical flux of horizontal momentum.*

Gray contours are negative values, black contours are positive.

transport across the domain. Both individual covariances exhibit the same behavior, so the phenomenon is likely a three–dimensional process.

The next series of figures illustrate the differences between the statistics of S150 and S30. Figure 26 shows the covariance of vertical velocity and temperature from both simulations. The height of the CBL becomes slightly shallower in S30 than S150, and is believed to be the result of changes in energy transport (caused by the higher resolution grid) and not boundary effects at the model top. The most obvious difference is the location and intensity of the near–surface vertical gradient of the statistic. S30 has covariance magnitudes similar to S150, but exhibits a much stronger gradient near the
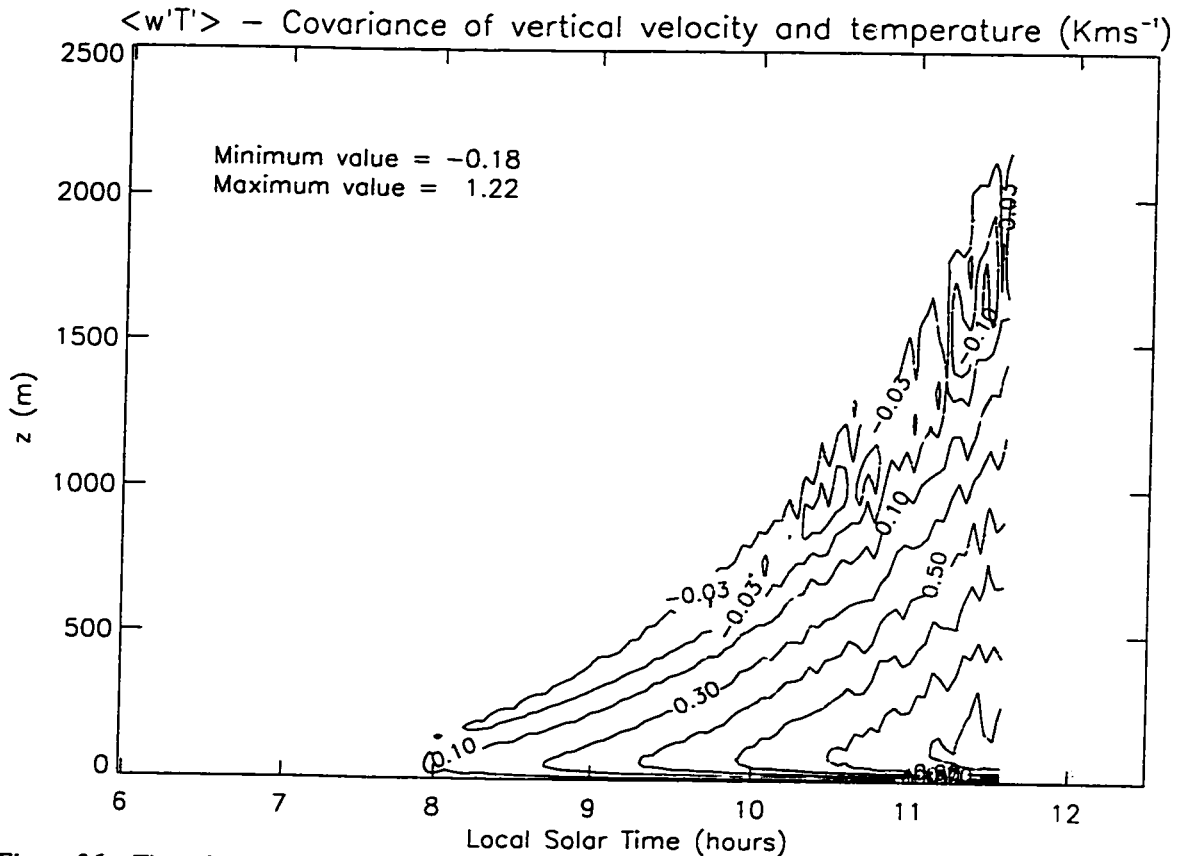
<w'T'> — Covariance of vertical velocity and temperature (Kms⁻¹)

Minimum value = −0.18
Maximum value = 1.22

Figure 26. Time–height comparison of S30 (black) and S150 (gray) <w'T'>
Contours are not all equally spaced.

surface. This difference is exemplified by the profiles of S30 covariance and the analogous S150 SGS quantity at approximately 0930 LST (immediately before resolved–scale convection begins in S150) shown in Figure 27. The S30 covariance is an order of magnitude or more greater than that of S150 throughout most of the CBL depth. In Earth LES studies, the resolved–scale covariance profile appears similar to that of S30. However, on Earth, the SGS contribution is quite significant near the surface, causing the total covariance profile (resolved+SGS) to be linear (negative slope) throughout the entire depth of the CBL. This profile shape indicates (via vertical heat flux divergence considerations) that convection on Earth acts to *warm* the atmosphere throughout the
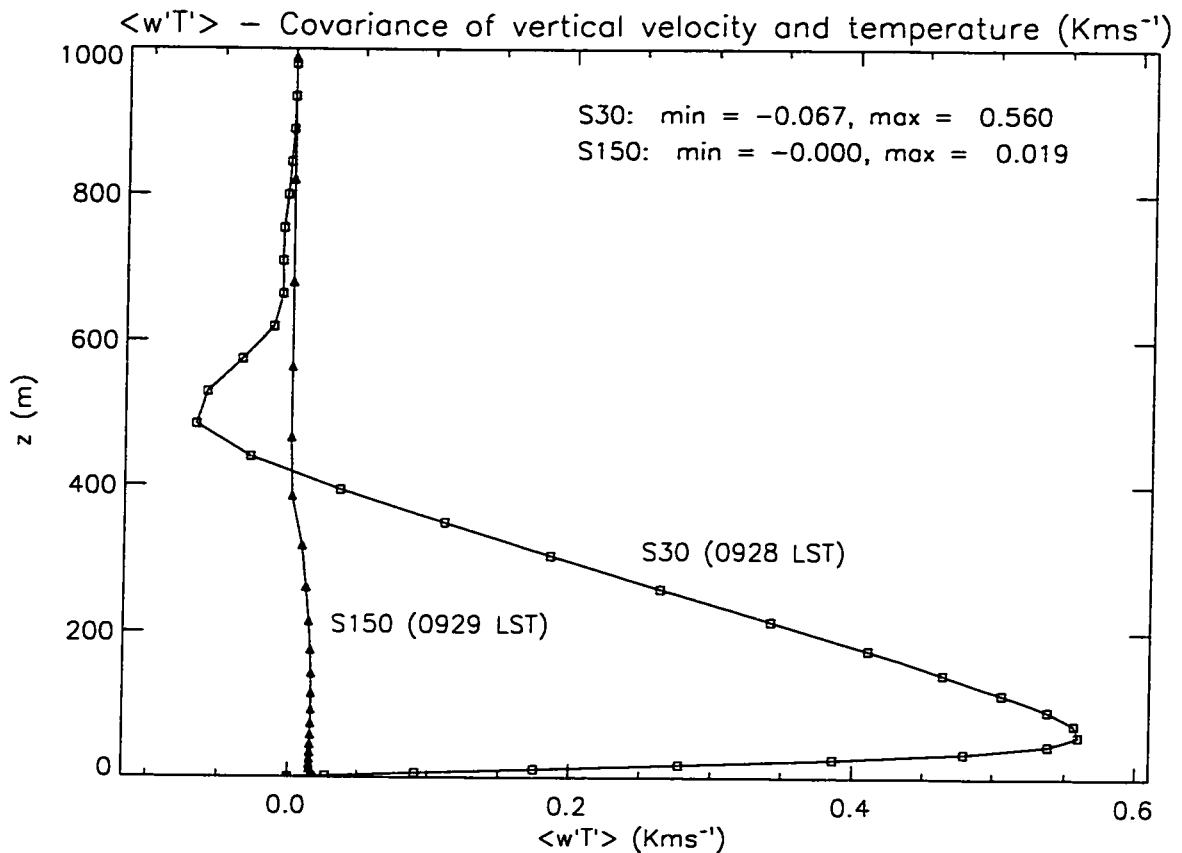
Figure 27. **Comparison of S30 (resolved) and S150 (SGS) <w'T'> profiles.**

CBL. On Mars, the SGS contribution as it is parameterized here is negligible, and the lowest portion of the covariance profile exhibits a positive slope, indicating that near the surface, convection is acting to *cool* the atmosphere. To make sense of this, consider that on Earth the atmosphere receives most of its energy via conduction from the surface, while on Mars the atmosphere receives most of its energy via the absorption of upwelling infrared radiation from the surface (Mars' atmosphere is relatively opaque in certain regions of the infrared spectrum). The role of convection in a fluid is to equalize the distribution of energy in the fluid, and as Mars' atmosphere is significantly heated internally at low levels by radiation (not just at its lower boundary via conduction), convection would naturally act to cool the atmosphere in that region and warm the
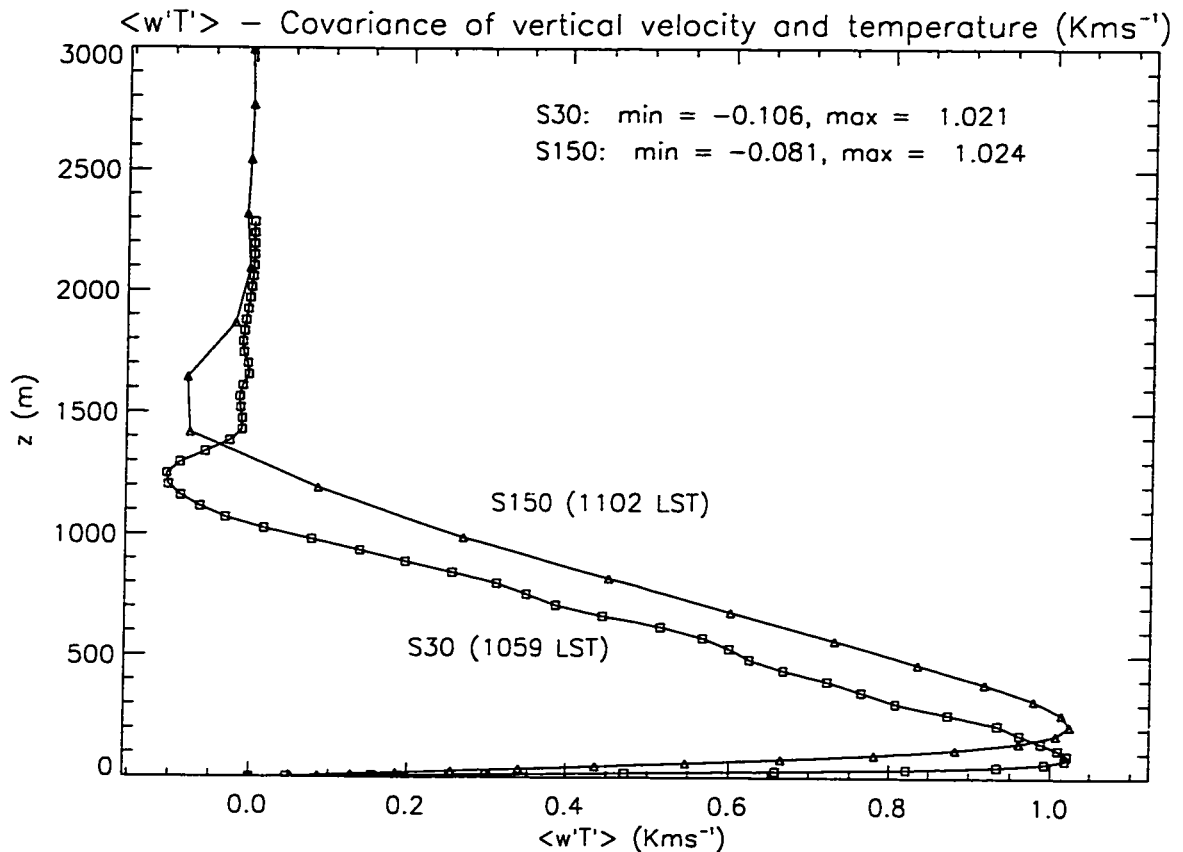
Figure 28. *Comparison of S30 (resolved) and S150 (resolved+SGS) <w'T'> profiles*

portion above. Figure 28 shows the covariance profiles after both simulations have achieved resolved–scale convection. It clearly shows a difference in CBL depth and in near–surface structure between S30 and S150. These observations are a clear indication that the terrestrial SGS turbulence scheme is not valid on Mars at similar spatial scales, and that the Martian atmosphere behaves differently than that of Earth at some scales.

Figure 29 is a comparison of S30 (resolved) and S150 (resolved+SGS) TKE results. There are two notable differences: The first is that the shape of the contours near the surface in S30 is opposite that in S150, due to the failure of the SGS scheme to properly represent near–surface convection in S150. The second is that as noted previously, the CBL depth in S30 is significantly less than in S150. Figure 30 shows
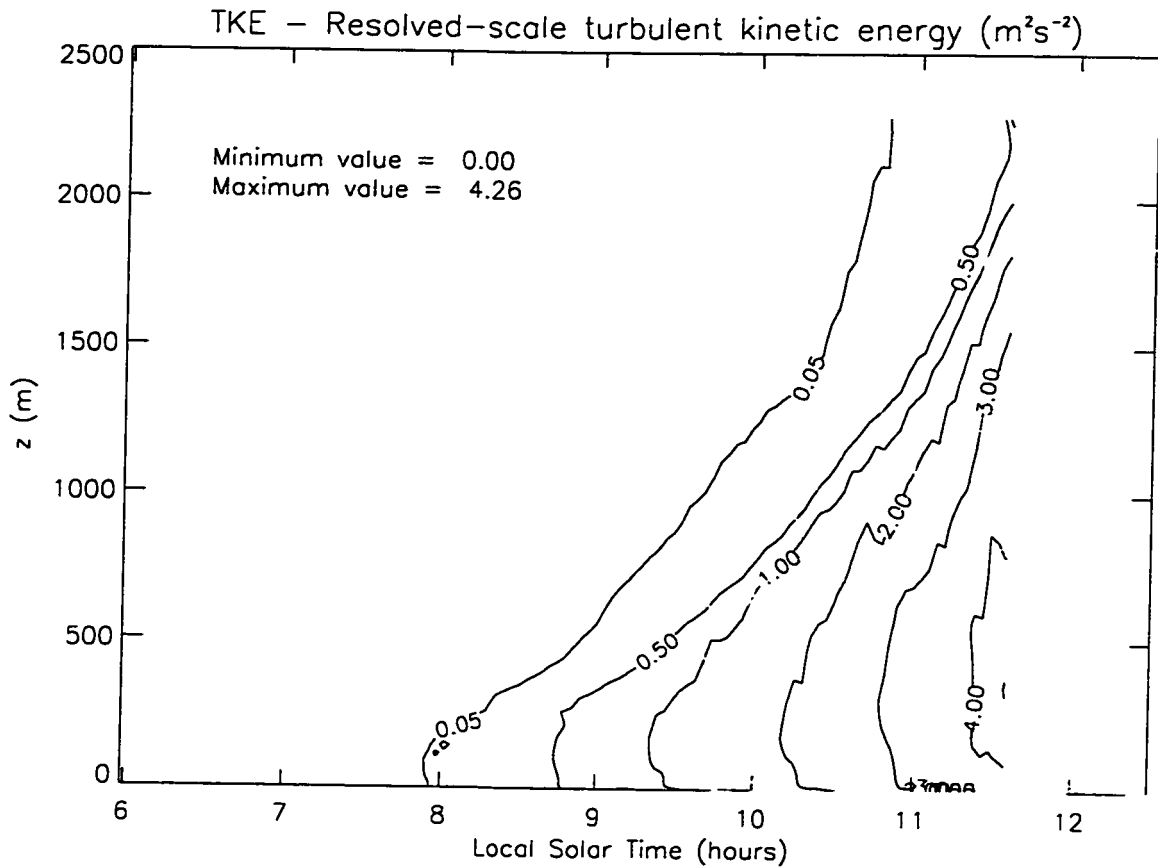
61

Figure 29. *Comparison of S30 (resolved, black) and S150 (resolved+SGS, gray) TKE. Contours are not all equally spaced.*

instantaneous profiles of TKE for S30 (resolved) and S150 (SGS). Again the SGS

scheme is shown to perform badly. Also, the region of near–constant TKE in the lowest

60 meters of the S30 profile *may* be the Martian surface layer. Profiles of S30 and S150

TKE after resolved–scale convection has set in are shown in Figure 31. The S30 TKE is

significantly greater than that of S150 in the lower 500 meters of the CBL. The opposite

is true above one kilometer in height. Examination of the corresponding vertical velocity

variance profiles (Figures 32, 33) reveals structure consistent with the differing CBL

heights, but not consistent with the behavior of the TKE profiles. Figures 34 and 35

reveal that behavior to be due to the variances of both horizontal wind components. This

indicates that the convection in S30 likely has a slightly different horizontal structure than that in S150, for reasons that are unclear at this time (except that grid resolution plays a important role).
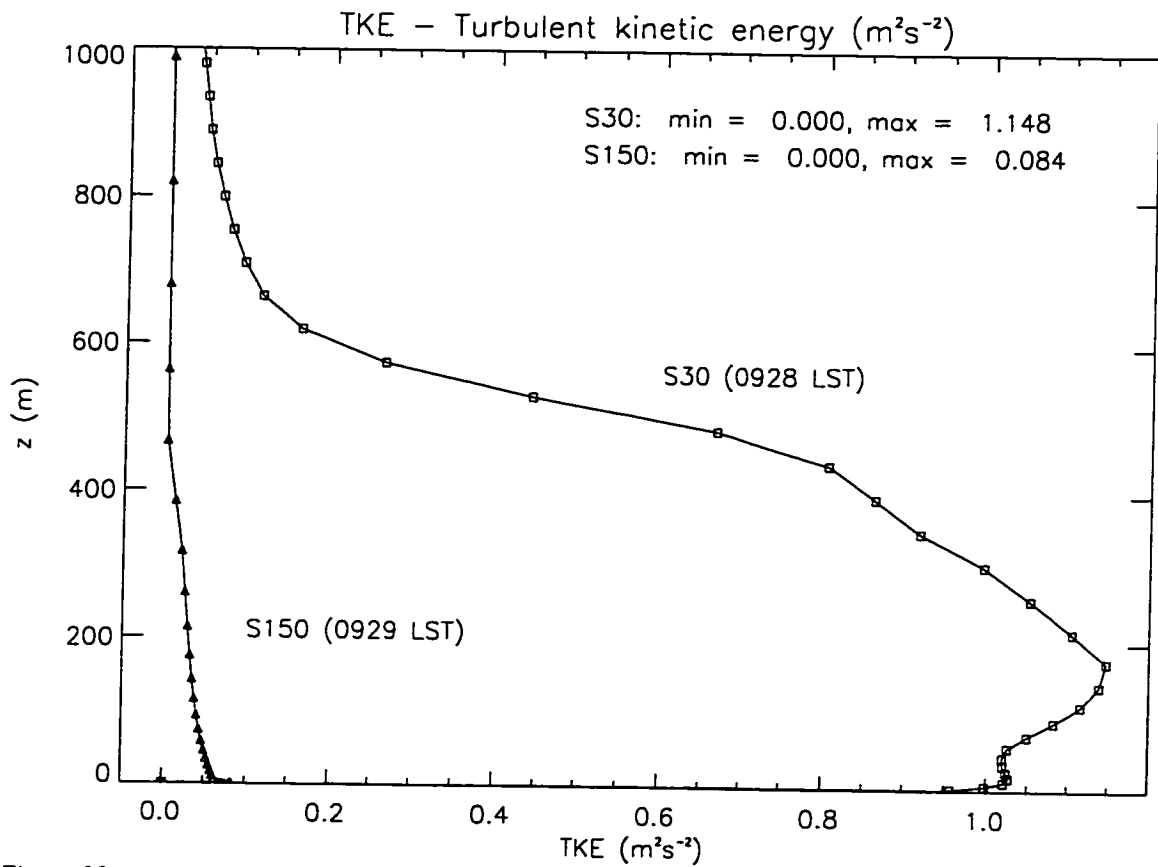

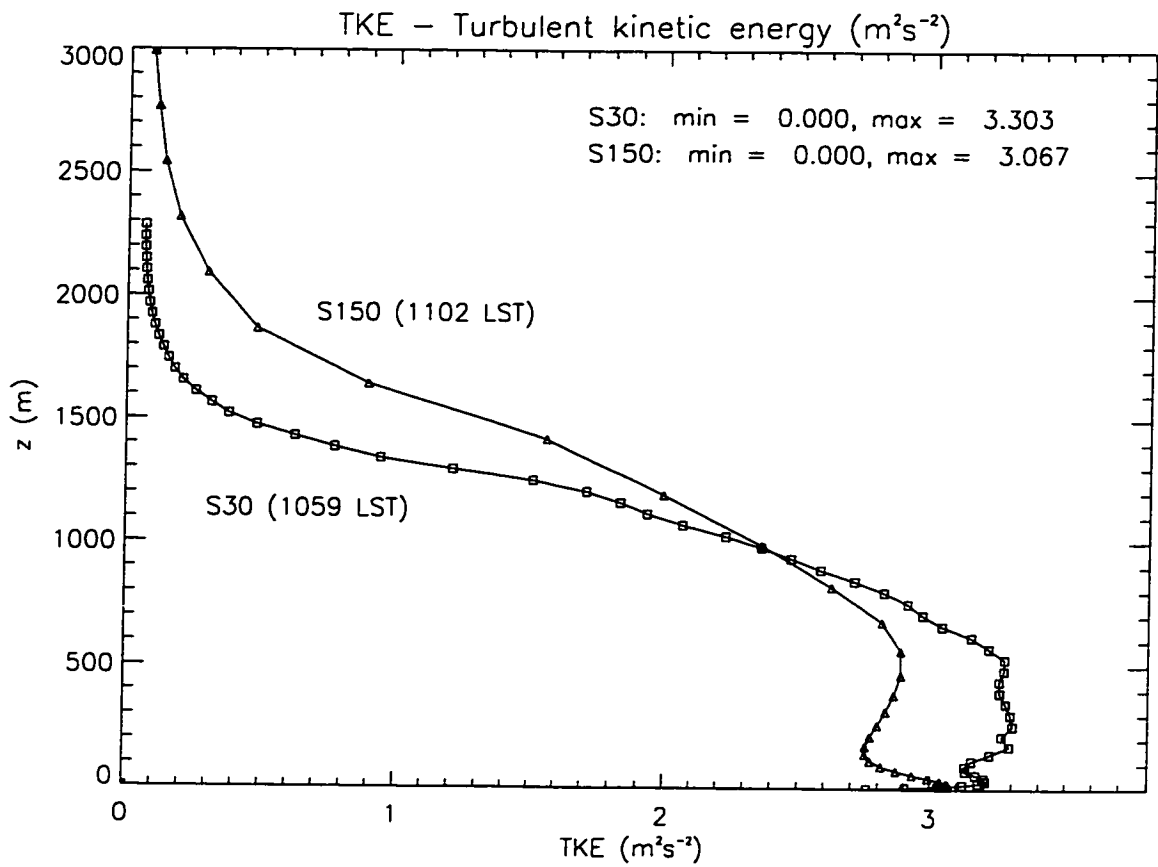*Figure 30. Profiles of S30 (resolved) and S150 (SGS) TKE*

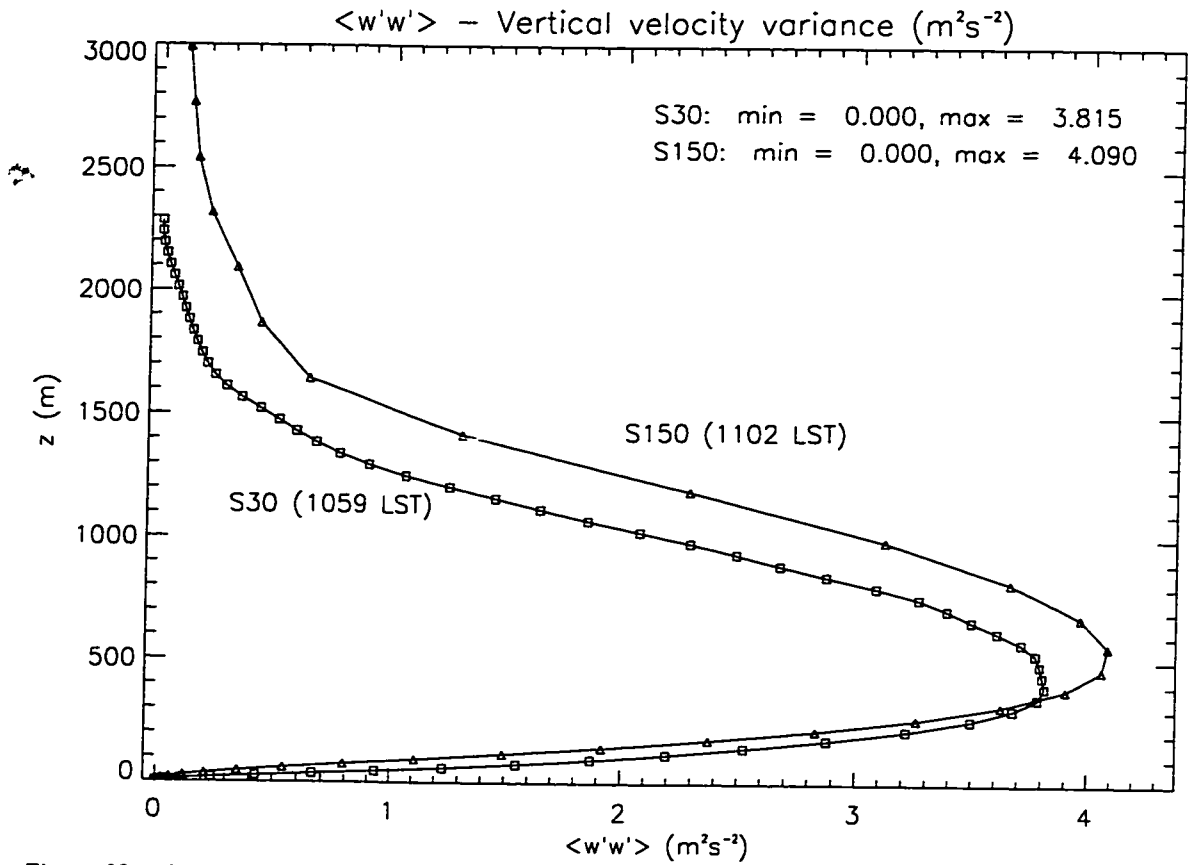*Figure 31.   Comparison of S30 (resolved) and S150 (resolved+SGS) TKE profiles.*

Figure 32. Comparison of resolved S30 and S150 vertical velocity variances.
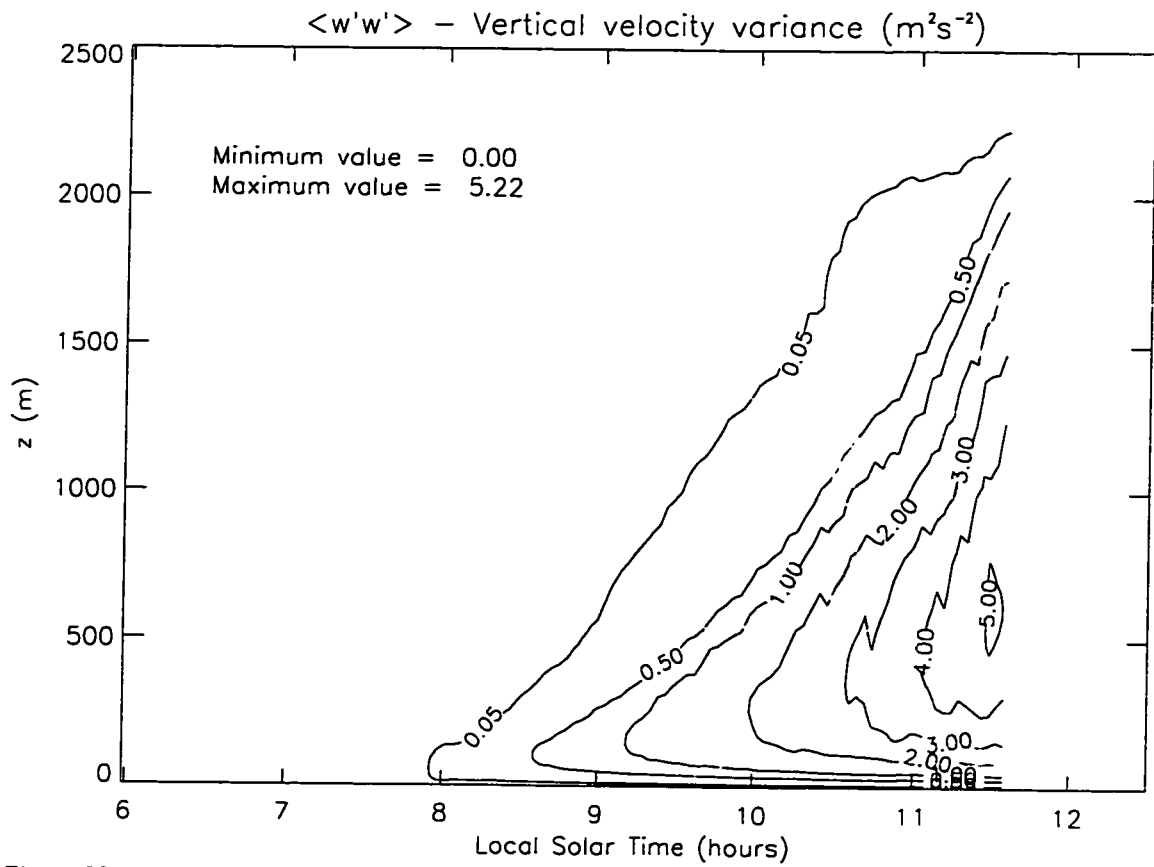
65

Figure 33. *Comparison of S30 (black) and S150 (gray) vertical velocity variances.* *Contours are not all equally spaced.*
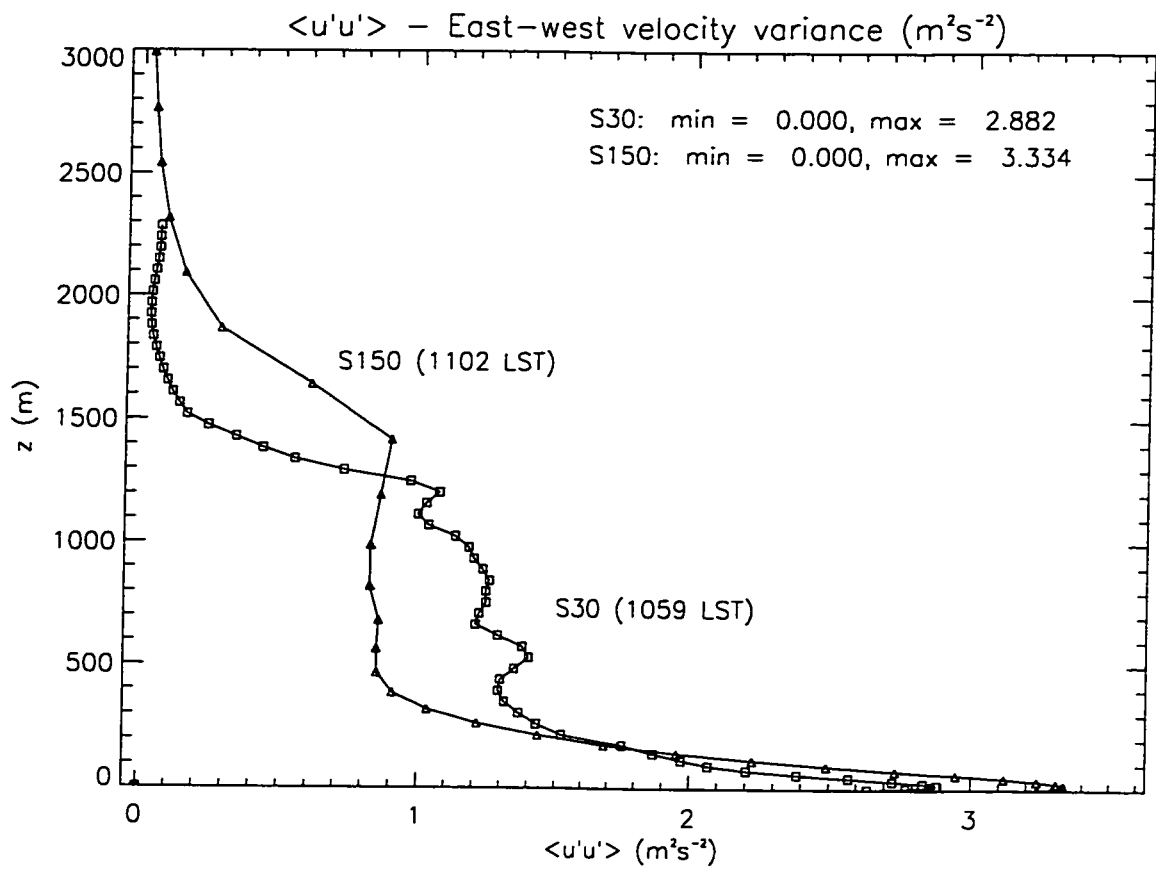
Figure 34. *Comparison of resolved S30 and S150 east-west velocity variances.*
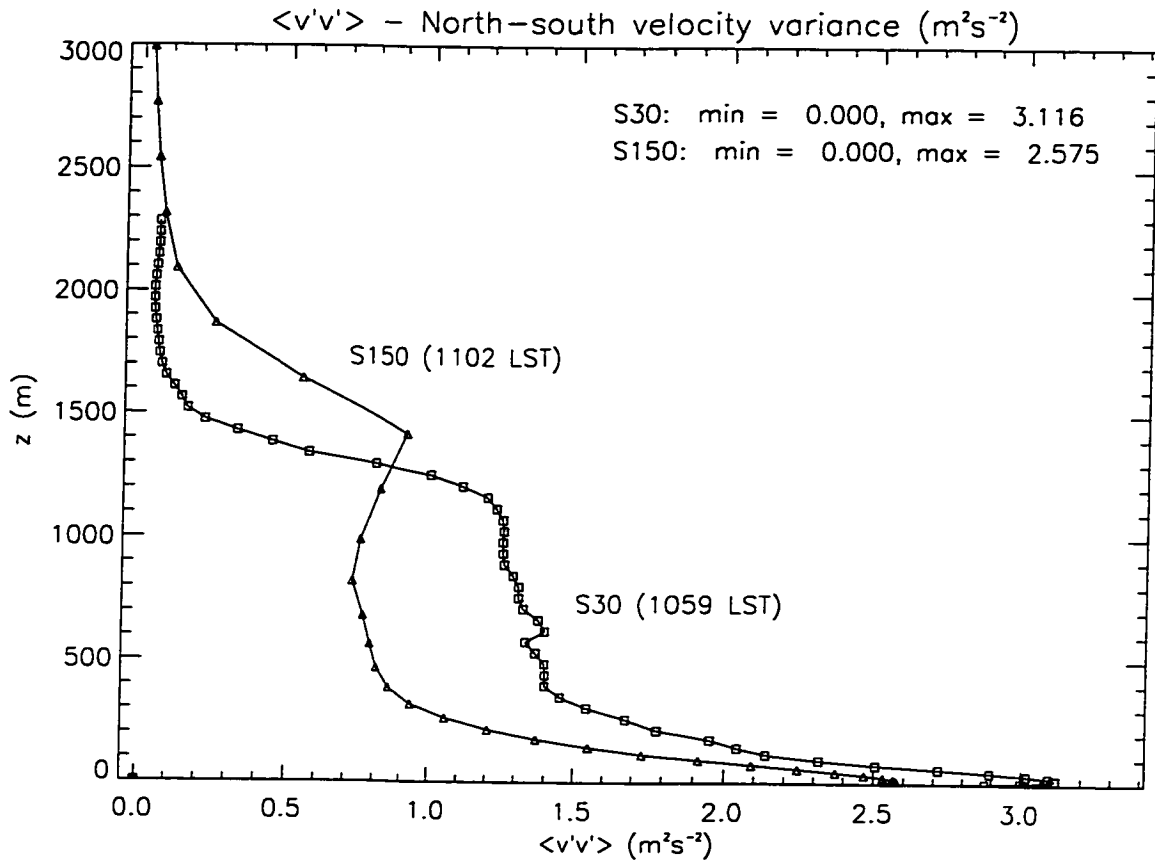
Figure 35. *Comparison of resolved S30 and S150 north–south velocity variances.*

Figure 36 shows the vertical velocity skewness profiles of S30 and S150. Assuming that the domain mean vertical velocity at each level is zero (in reality it is quite small), a positive value of this statistic indicates that updrafts are narrower than surrounding downdrafts, and vice versa. The vertical velocity skewness is positive throughout most of the CBL, and has a maximum near the top of the CBL. Gravity waves propagating along the top of the CBL are the reason for the sudden decrease above the maximum, since they have roughly equal areas of upward and downward velocity. Near the surface, the skewness becomes distinctly negative, indicating a tendency for narrow downdrafts and broad rising motion there. These profiles are quite similar in all
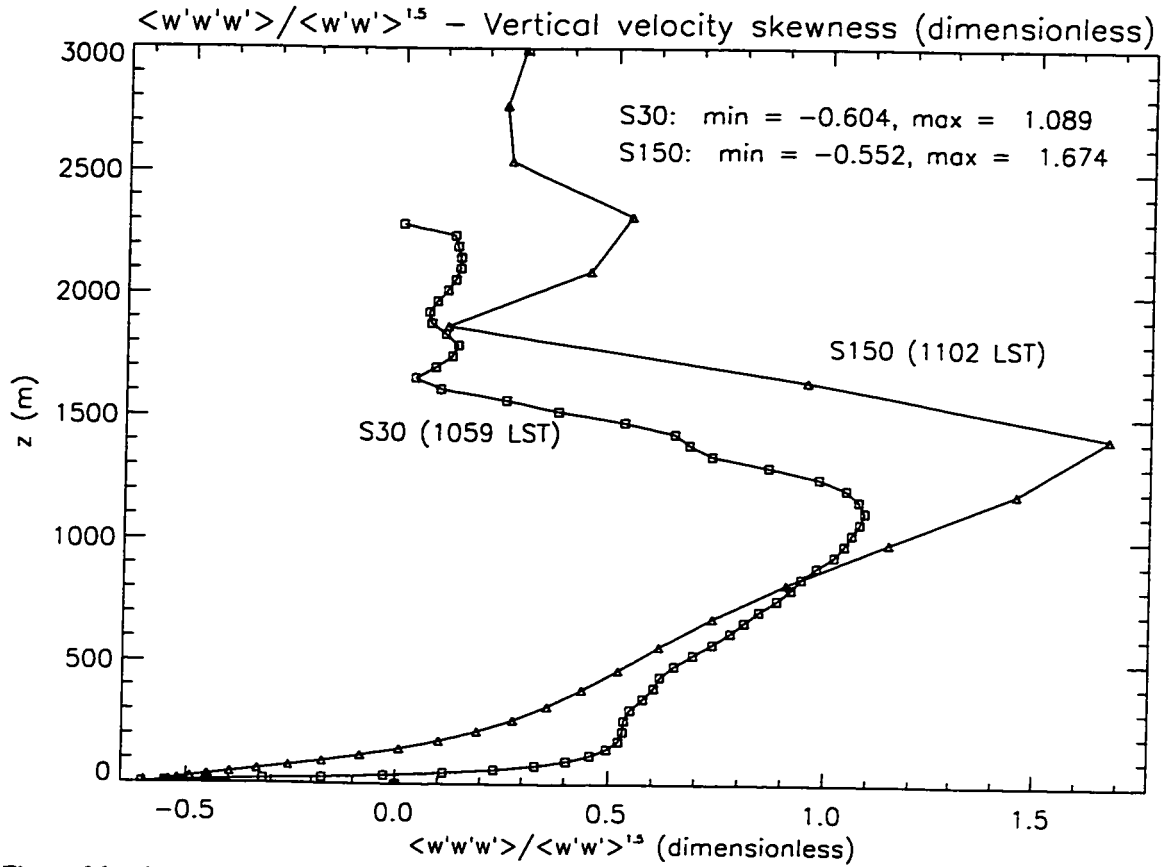
Figure 36.   Comparison of S30 and S150 vertical velocity skewness.

respects to Earth LES results, though those terrestrial results do not agree well with Earth

observations (Moeng and Rotunno 1990). Also note the significant effect grid resolution

has on the skewness profiles. Figure 37 shows a time–height plot of the S150 vertical

velocity skewness. It shows that throughout the convective day, the skewness profile is

quite consistent until about 1630 LST, when skewness aloft decreases rapidly, indicating

the collapse of the narrow updrafts. Also visible at approximately 1715 LST is the

reversal of the near–surface skewness from negative to positive, indicating broad

downward motion and narrow regions of upward motion. Nearly simultaneously, the

skewness aloft also switches sign. These reversals appear to indicate the onset of the
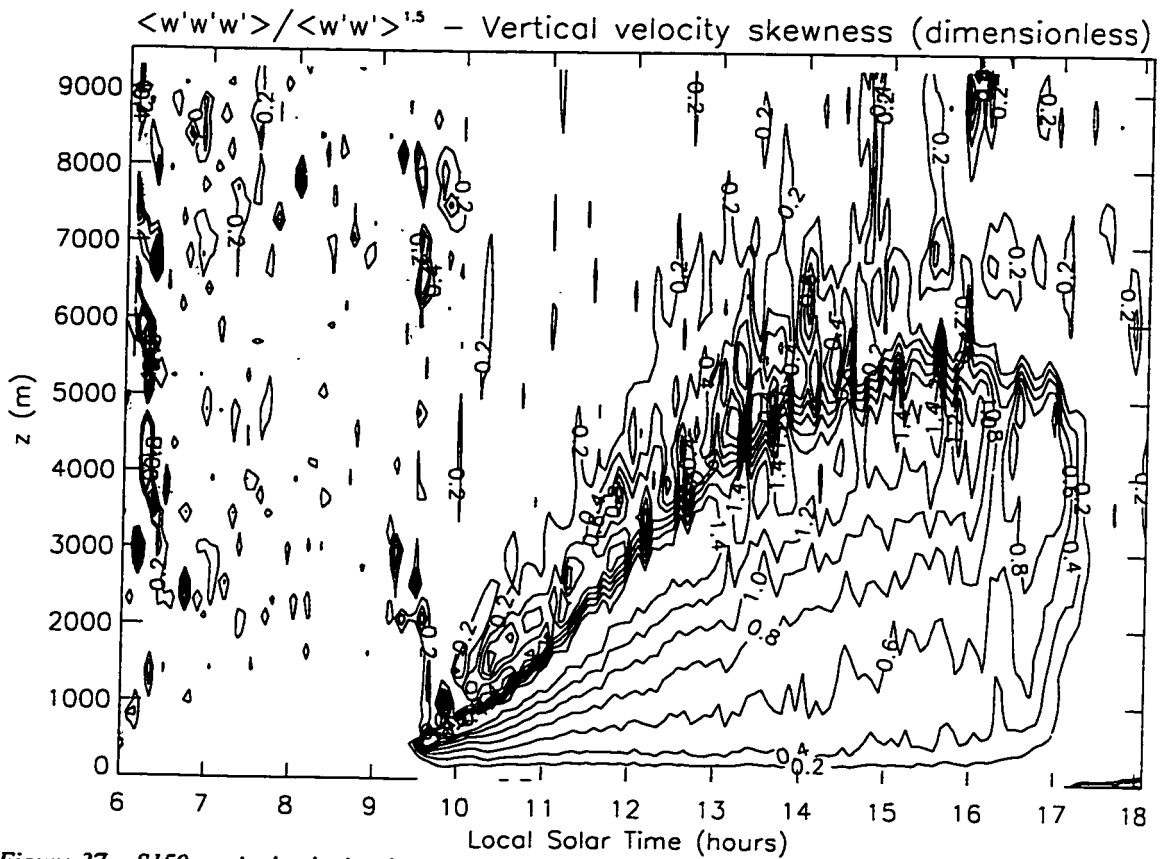
nocturnal ABL processes.

69

Figure 37. *S150 vertical velocity skewness.*

Contours are not all equally spaced. Negative contours are gray, positive contours are black.

4.2.3 Comparison to MPF data

The measured MPF temperature and wind time series have a rather large variance during the day. This has been interpreted as primarily being the effects of daytime convection at the MPF site. If that is the case, the variance of the temperature and wind time series from the present LES simulations (at the MPF site) should compare well with the lander dataset. It is important to note, however, that with the possible exception of temperature, the mean magnitudes of the LES quantities cannot be expected to match those of the MPF observations, due to the partially idealized nature of the present LES. LES results are from S150 and are plotted every 300 seconds. The time resolution of the

70

MPF data vary, but are generally of higher time resolution than the LES results presented here. Finally, though the S30 results will not be shown here, the variation that they exhibit is slightly greater than that of the S150 results.
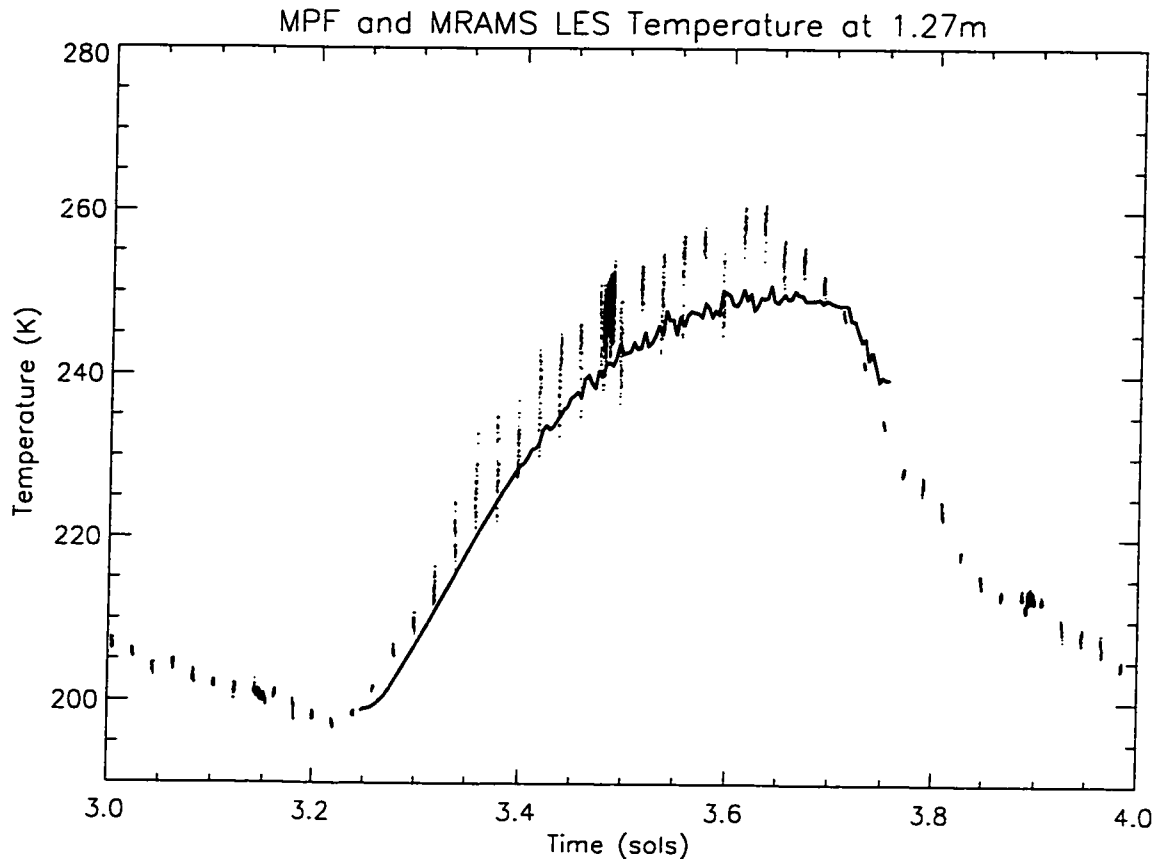

Figure 38. Comparison of MPF and LES temperature. (MPF: black points, LES: black line)

Figure 38 compares observed and modeled temperature at a height of 1.27 meters above the surface. MRAMS temperatures here are simply linearly extrapolated from the lowest model level of 1.9 meters. The MRAMS values are slightly colder than the MPF data, but do exhibit a variance of about 4 K (observed value is about 10K during mid-day).

Modeled and observed wind speeds are shown in Figure 39. Again MRAMS exhibits a sizable amount of variation (about 7 m s^{-1}) due to convective motions. Also

71

MPF and MRAMS LES Wind Speed at 1.27m
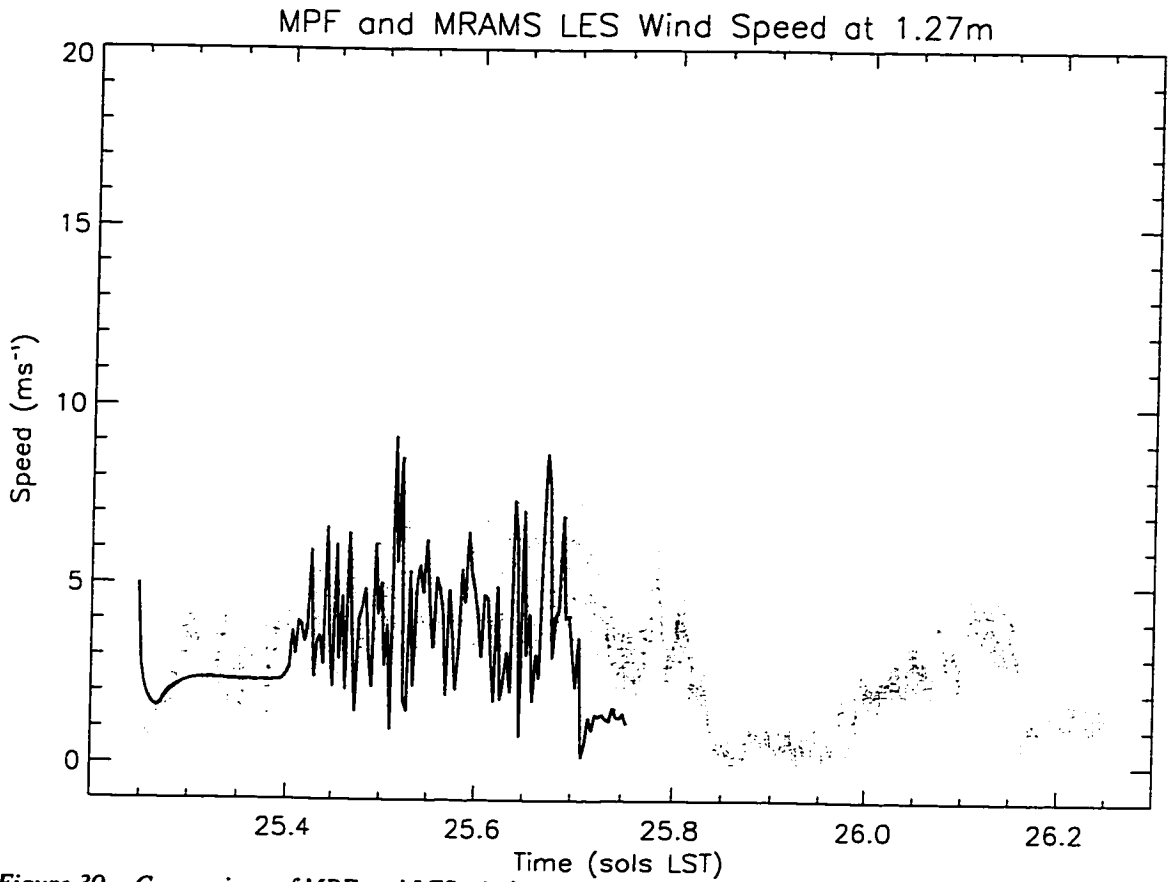
Figure 39. Comparison of MPF and LES wind speed. (MPF: gray points, LES: black line)

note the steep drop (after the 25.7 time graduation) in the wind magnitude and variability after the large-scale convection collapses (seen also in the MPF dataset). A comparison of modeled and observed wind direction is shown in Figure 40. The amount of variation in the MRAMS wind direction compares well to the MPF data. Again note that after convection collapses, the wind direction becomes much more constant (borne out in the MPF data as well).

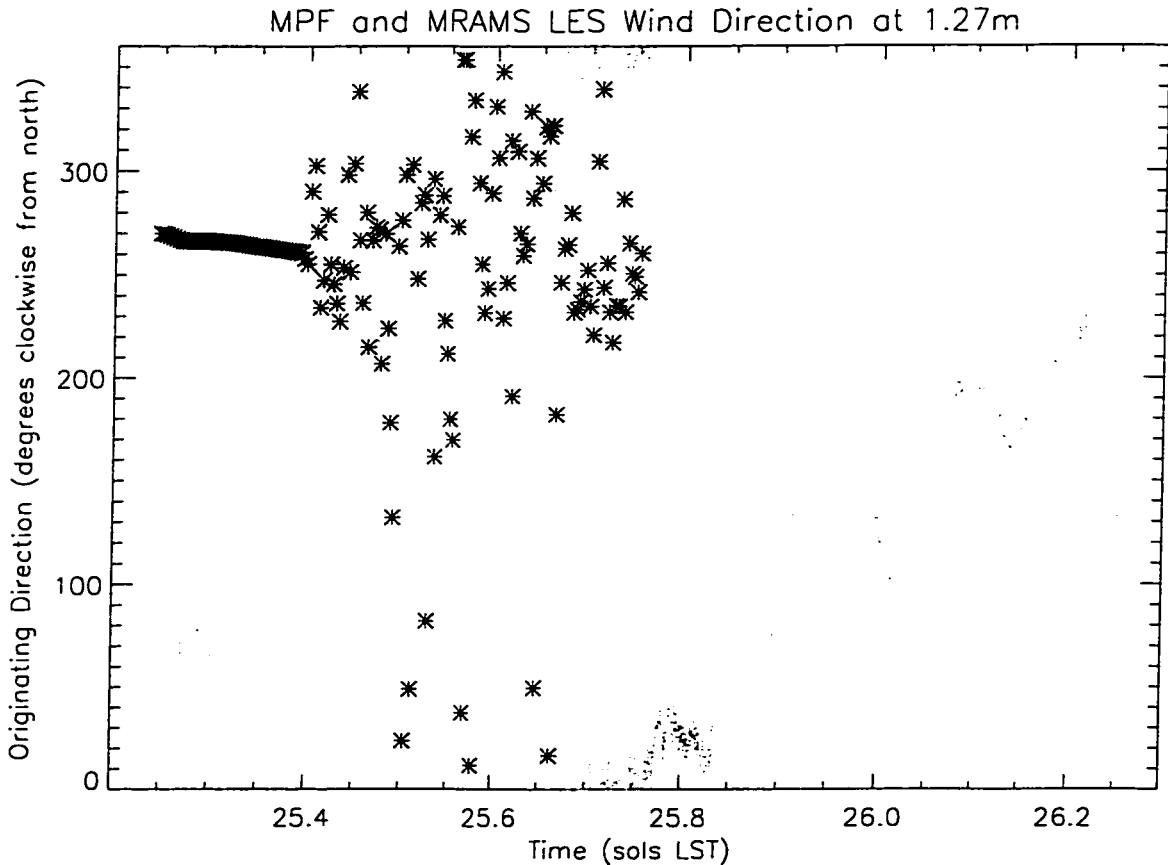*Figure 40. Comparison of MPF and LES wind direction. (MPF: gray points, LES: black asterisks)*

4.2.4 Dust Devils

Dust devils are known to be common across plains during the daytime on Mars

(Ryan and Lucich 1983; Thomas and Gierasch 1985). Specimens as large as one

kilometer in width and eight kilometers tall have been seen in orbital imagery. Viking

Lander and Mars Pathfinder meteorology instruments have recorded several suspected

small dust devils passing over or near them (Schofield et al. 1997). Small dust devils

have also been found in Mars Pathfinder lander imagery (Metzger et al. 1999). Given

dust devils' often large size and apparent ubiquity at many places on Mars, it seems

probable that they may be modeled in an Mars LES simulation. An LES such as S30 or

even S150 should in principle be able to capture these atmospheric phenomena.

It is important to realize that a given dust devil circulation may not be visible to the unaided eye if there is no dust to entrain, the circulation does not extend fully to the surface, or if the circulation is too weak to entrain dust. Also, the fine details of the dust devil circulation, especially near the ground, occur at quite small scales, and thus will not be resolved in any current LES. Finally, the structure, dynamics, and evolution of dust devils on both Earth and Mars is not well known. The large size of Martian dust devils may enable them to be simulated and studied with greater ease and the results applied by analogy to the study of the often much smaller terrestrial variety.

Surface–based convective vortices were found in both S30 and S150, beginning shortly after resolved–scale convection initiated and ending when the large–scale convection began to collapse. The strongest and largest dust devils occurred during the early afternoon, when convection is at its maximum intensity. Dust devils nearly always occurred along large–scale convective cell boundaries (updrafts), and the most intense vortices occurred at the vertices of the polygonal convective cell pattern. Near–surface wind speeds in the modeled dust devils were local maxima (on the order of 10 m s^{-1}), but not significantly greater than speed maxima caused by larger–scale processes. Distinct negative pressure perturbations (up to about 2 Pa) were associated with all of the mature dust devil circulations. The magnitude of this pressure drop compares well (after considering the difference in ambient atmospheric pressure) with measurements of Earth dust devils which produce perturbations of about 2 hPa. Calculations performed for a number of the modeled circulations indicated that they are very nearly cyclostrophically balanced. Many of the modeled dust devil circulations were found to attain heights of

60% of the CBL depth or more. Preliminary examinations of the LES results appear to indicate that helicity (i.e., horizontal vorticity) generated baroclinically along updraft lines is a primary source for many dust devils' vorticity.

An example of a simulated dust devil is shown in the next several figures. Figure 41 is a plot of (at a level of 1.9 meters) the horizontal streamlines (the mean wind has been subtracted from the wind components) for a dust devil that was present in S30 at 1112 LST. Note that dust devils at this time of day are not near their peak intensity and size. The anticyclonic dust devil is approximately 200 meters wide at its base, and widens and tilts toward the northeast somewhat with height. This vortex is only about 500 meters deep, and if it were dust–laden, an observer would likely describe it as a wedge–type dust devil. Figure 42 illustrates the perturbation imposed on the total pressure field by the same vortex, which is quite small (about 0.55 Pa), but nevertheless is distinctly and unambiguously present. The corresponding vertical velocity field is shown in Figure 43. Note that the vortex lies along and is embedded in one of the narrow, quasi–linear updraft features. Figure 44 is a contour plot of the total wind magnitude, in which the vortex's location is clearly obvious. Notice that due to a mean east–west wind, the northern half of the dust devil exhibits the most intense wind (constructive interference). An east–west vertical cross–section of 3D relative vorticity magnitude through the dust devil is shown in Figure 45. The vortex clearly tilts with height. Figure 46 shows a similar cross–section of vertical velocity, illustrating how the dust devil is embedded in a much larger–scale buoyant plume. The dashed contours at lower center are of relative vertical vorticity, and are intended to show the location of the vortex. Note that the maximum vertical velocity is located along the leading edge of the

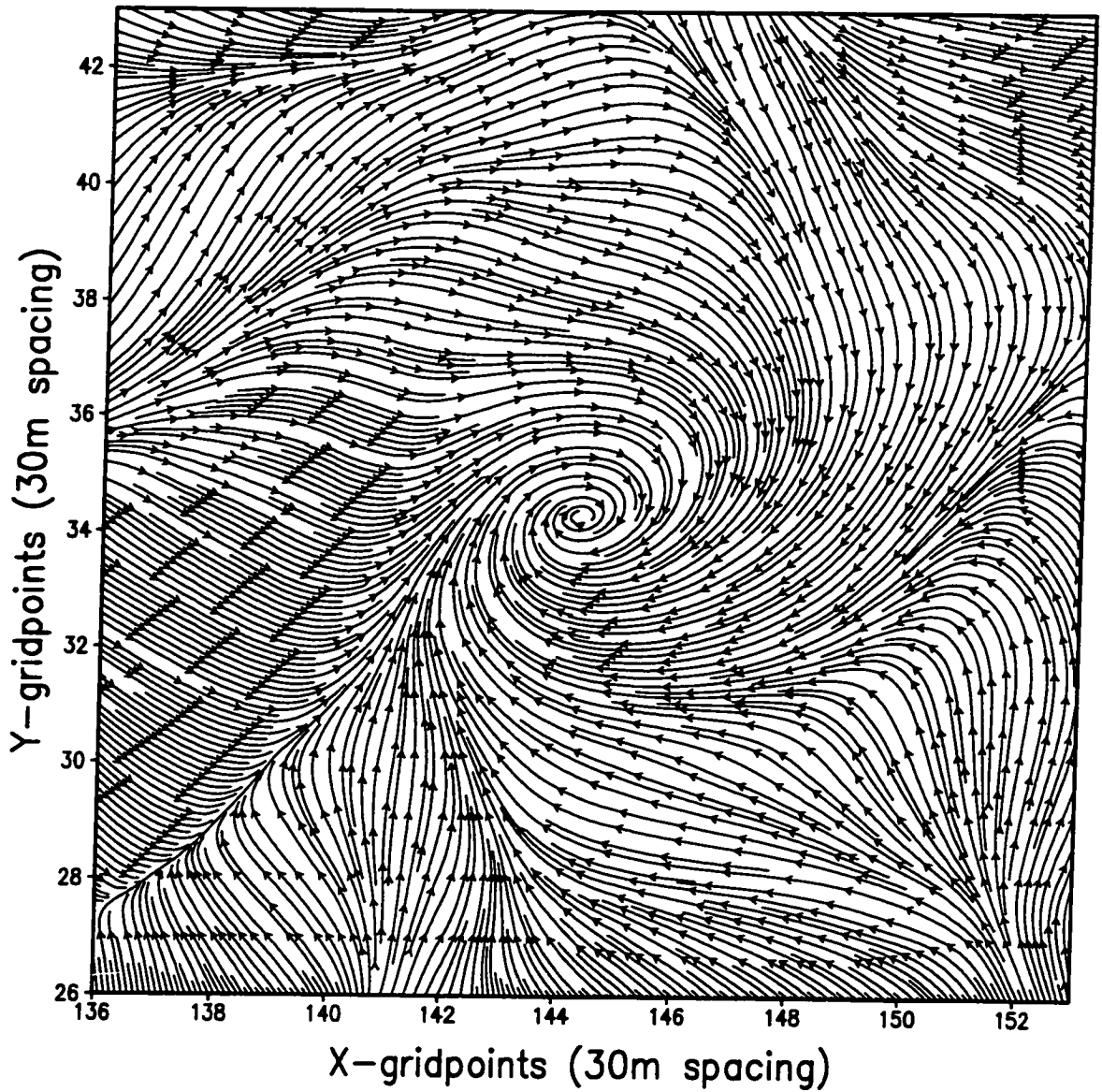vortex (movement is from left to right), whereas there is a distinct minimum along the trailing edge.

Figure 41. Horizontal streamlines (mean wind removed) of S30 dust devil at 1112 LST and z = 1.9 m
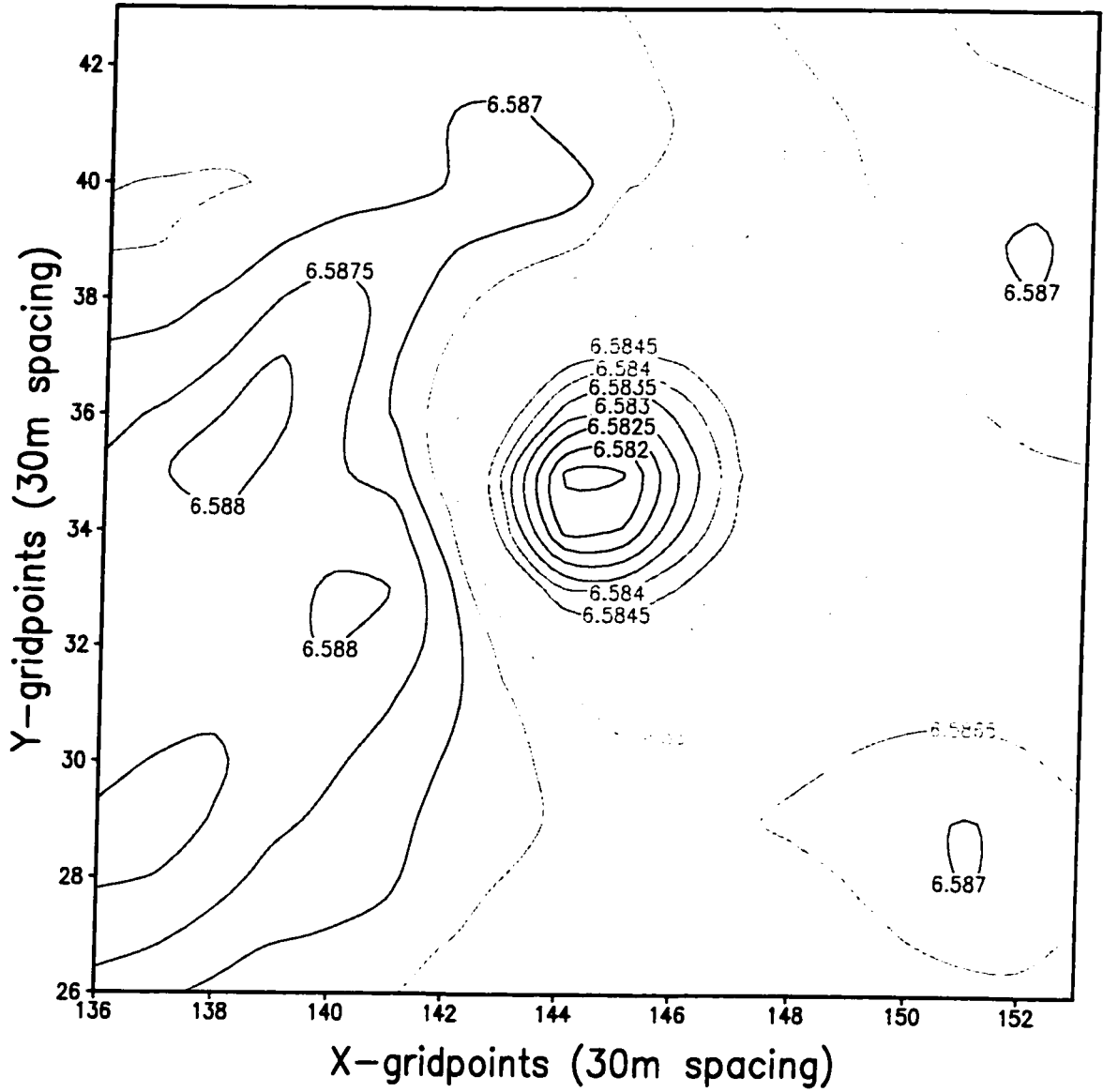
Figure 42. Same as Figure 41, except contours of pressure (hPa)
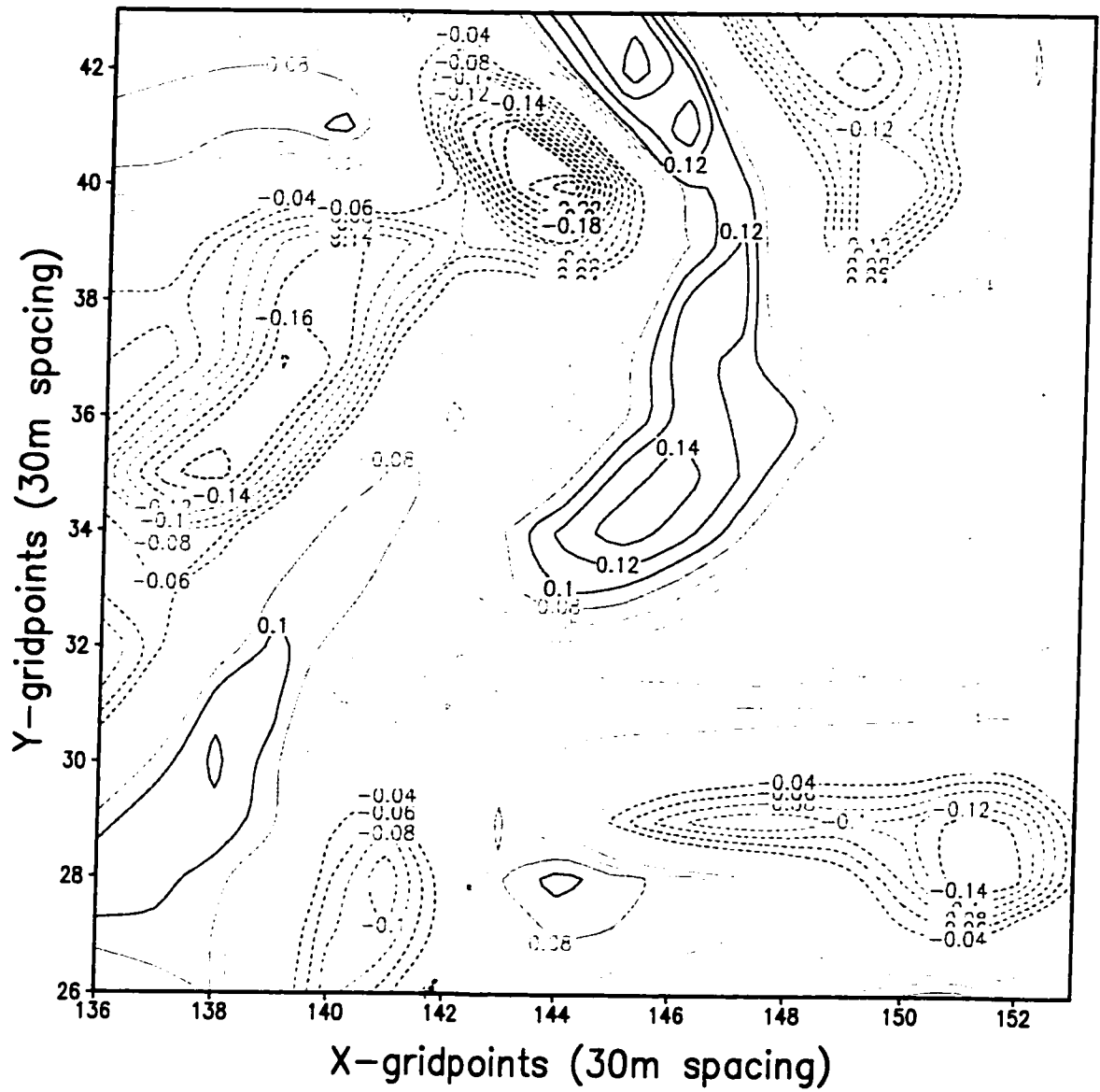
Figure 43.   Same as Figure 41, except vertical velocity (m s⁻¹)

78
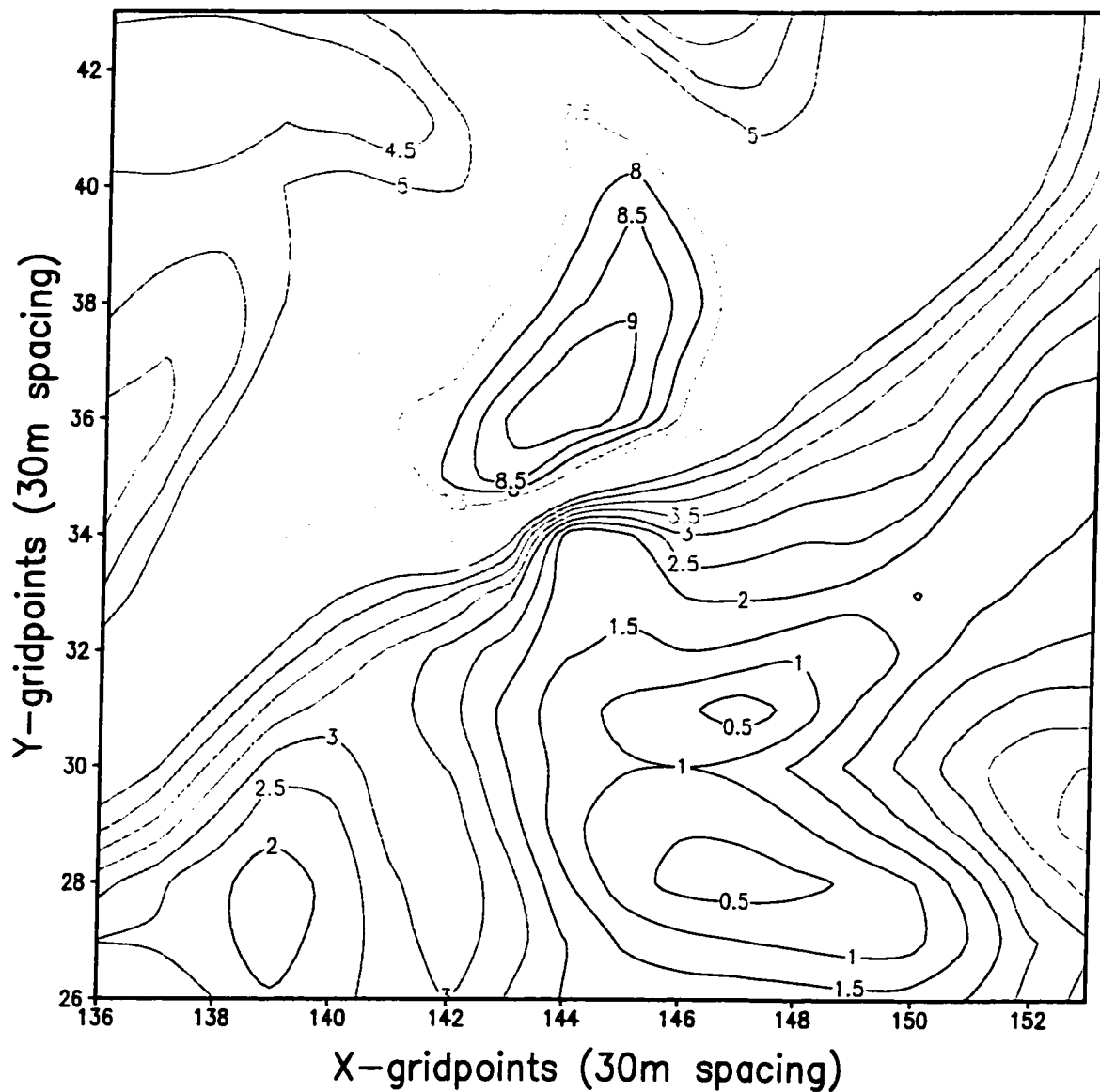
Figure 44. Same as Figure 41, except contours of total wind speed (m s⁻¹)

Figure 45. East—west vertical section (y = 35, 1112 LST) through the same dust devil as previous figures. Contours are of 3D relative vorticity magnitude (rad s⁻¹).

80

Figure 46.   Same as Figure 45, but vertical velocity (m s⁻¹)

(dashed contours in lower center are relative vertical vorticity — intended only to show dust devil location)

5. SUMMARY AND CONCLUSIONS

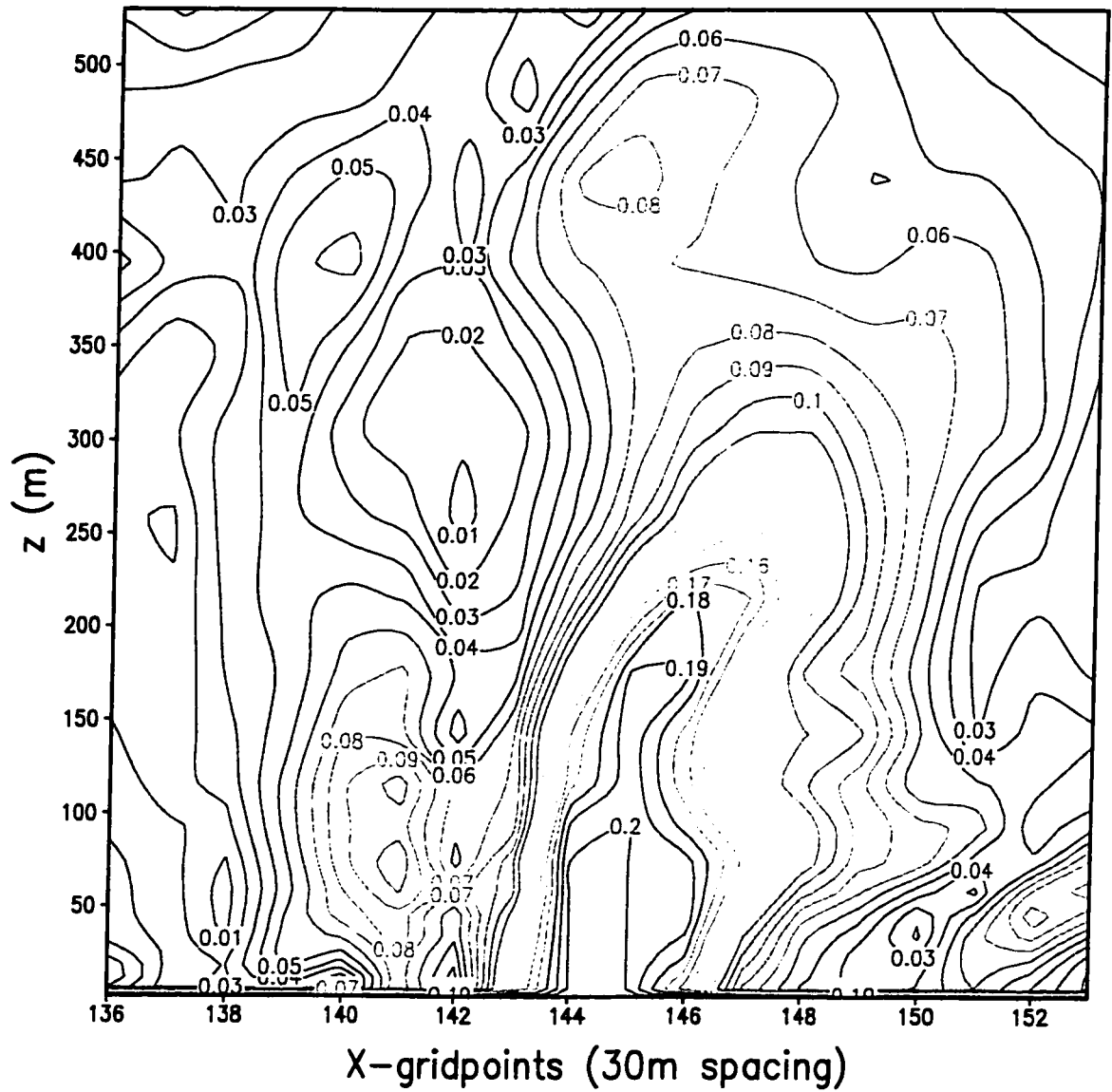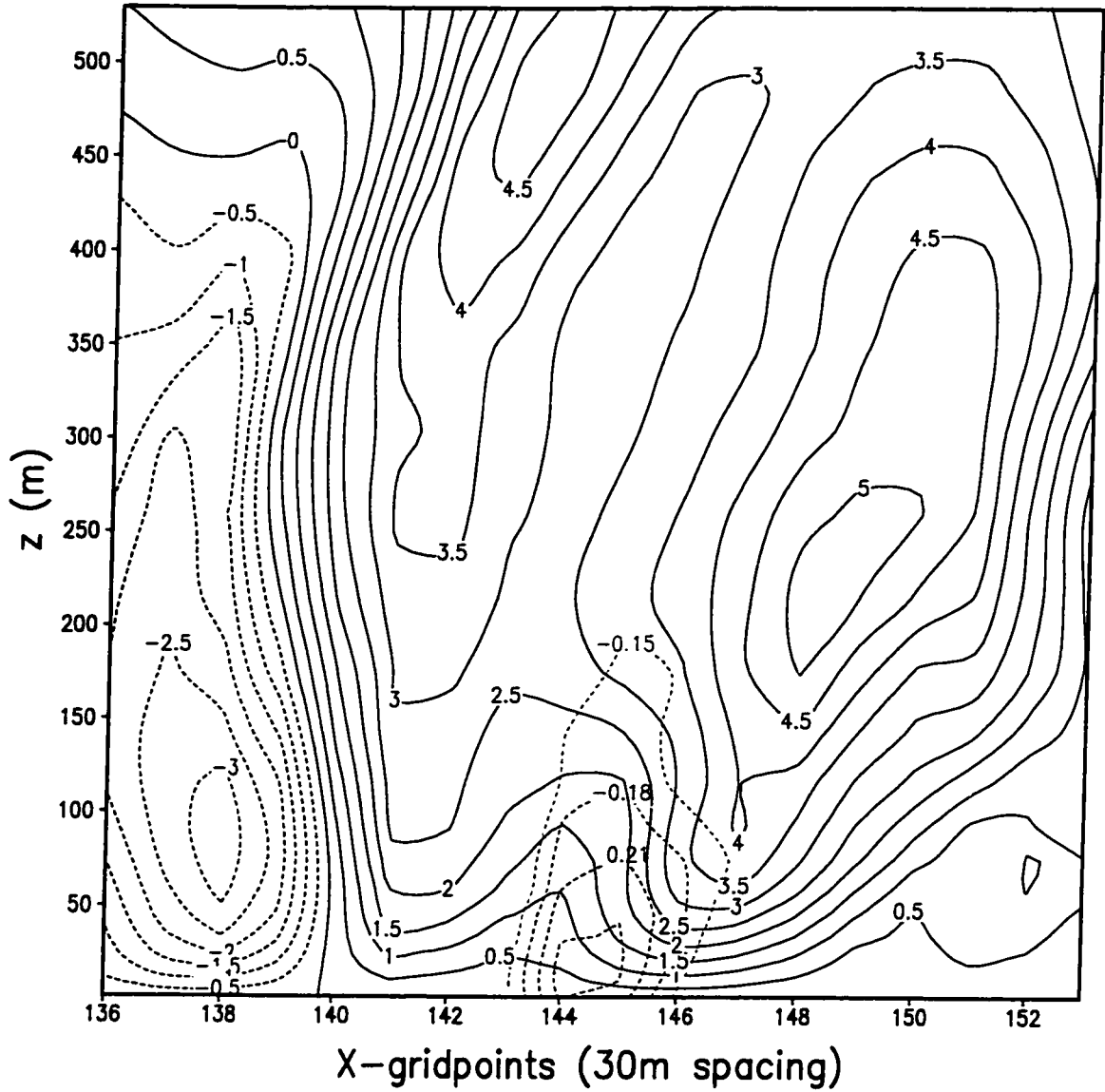A new and improved version of the Mars Regional Atmospheric Modeling System was constructed using the terrestrial RAMS 4.3.0 model as a base. Many modifications were required to complete this task, including porting the NASA Ames MGCM radiation code, adding support for the input of surface property and topography spacecraft datasets, modifying the terrestrial use of calendar dates within the model, etc. A method for calculating and including topographic shadowing in MRAMS was also successfully implemented.

An MRAMS simulation of the Mars Pathfinder and Viking 1 lander sites was performed. In general the results of that simulation compared well with observations, but it is concluded that a horizontal gridspacing of 60 kilometers is not sufficient to accurately model the Viking 1 Lander site. Additionally, there is a known issue with anomalously weak atmospheric tides in the boundary conditions (from MGCM output) that were used that needs to be addressed further.

Two LES of the Martian atmosphere were performed using horizontal gridspacings of 30 and 150 meters. The convective boundary layer of Mars was found to consist of large-scale structures outwardly similar to those in Earth's CBL. Numerous dust devils were also present in both simulations. However, several key differences between the CBL of Mars and Earth were noted: First, the lower atmosphere of Mars receives energy from the Sun primarily through the absorption of upwelling infrared radiation from the surface. This causes convection on Mars to cool the lower levels of the CBL and heat the remainder, whereas on Earth convection heats the entire CBL. Secondly, Mars' lesser gravity, much lower atmospheric density (thus much less heat

transport efficiency), and comparable amount of insolation (roughly half that of Earth) result in anisotropic convection that is several times deeper and more intense than that on Earth. Finally, the terrestrial subgrid–scale turbulence scheme (often used on Earth for horizontal gridspacings on the order of 100 meters) based on that of Deardorff (1980) appears to be invalid on Mars, even for simulations with a horizontal gridspacing as small as 30 meters. It appears that this is due to the presence of nondissipative, energetic turbulence that occurs at considerably smaller scales than on Earth. It is surmised that at some grid scale possibly much smaller than 30 meters the terrestrial SGS scheme will become valid.

As often happens in science, many more questions were raised than were answered. Future work stemming from the present research may include:

Turbulence theory and parameterizations for Mars: In light of the failure of the terrestrial SGS model, is the theoretical framework developed on Earth for the surface layer strictly valid on Mars as well? Important model parameterizations are based on those theories. Moreover, are the Earth–based empirical data used in so many ABL and surface layer parameterization schemes representative of Mars conditions as well? Indeed, it is contentious whether they are truly representative of Earth's atmosphere. The comparison of Mars turbulent power spectra to those of Earth may yield clues. Mars LES results can also be used to create new, more accurate turbulence parameterizations for use in mesoscale models and MGCMs. The study of the Martian CBL may well provide insight into the workings of the terrestrial CBL as well.

Realistic LES with topography and complex mean wind shear: What effects do complex vertical wind shear and realistic topography have on convection? Where and

83

when (seasonally) on Mars does intense convection occur? Is real convection a hazard to spacecraft descending to the surface or to all manner of flying craft in the lower atmosphere? In the future it should be possible to use the nested grid capability of MRAMS to nest from semi–global scales down to LES scales in a single simulation — and begin searching for the answers to the above quandaries.

The role of convection in the lifting and transport of dust on Mars: By what processes are dust devils formed? What is the detailed structure of a dust devil? What dust lifting potential do dust devils possess? What dust lifting potential do the larger–scale convective structures possess, and how do they contribute to the genesis and/or maintenance of a dust storm?

6. REFERENCES

Antoniadi, E. M., 1930: *La Planète Mars 1659–1929*. Herman et Cie (Paris).

Deardorff, J. W., 1972: Numerical investigation of neutral and unstable planetary boundary layers. *J. Atmos. Sci.*, **29**, 91–115.

Deardorff, J. W., 1980: Stratocumulus–capped mixed layers derived from a three-dimensional model. *Bound. Layer Meteor.*, **18**, 495–527.

Dörnbrack, A., 1997: Broadening of convective cells. *Q. J. R. Meteor. Soc.*, **123**, 829–847.

Fiedler, B. H., and M. Khairoutdinov, 1994: Cell broadening in three–dimensional thermal convection between poorly conducting boundaries: Large eddy simulations. *Beitr. Phys. Atmos.*, **67**, 235–241.

Forget, F., F. Hourdin, R. Fournier, C. Hourdin, O. Talagrand, M. Collins, S. R. Lewis, P. L. Read, and J. P. Huot, 1999: Improved general circulation models of the Martian atmosphere from the surface to above 80 km. *J. Geophys. Res.*, **104**, 24155–24176.

Haberle, R. M., H. C. Houben, R. Hertenstein, and R. Herdtle, 1993a: A boundary–layer model for Mars: Comparison with Viking Lander entry data. *J. Atmos. Sci.*, **50**, 1545–1559.

Haberle, R. M., J. B. Pollack, J. R. Barnes, R. W. Zurek, C. B. Leovy, J. R. Murphy, H. Lee, and J. Schaeffer, 1993b: Mars atmospheric dynamics as simulated by the NASA Ames general circulation model. 1: The zonal–mean circulation. *J. Geophys Res.*, **98**, 3093–3123.

Haberle, R. M., M. M. Joshi, J. R. Murphy, J. R. Barnes, J. T. Schofield, G. W. Wilson, M. Lopez–Valverde, J. L. Hollingsworth, A. F. C. Bridger, and J. Schaeffer, 1999: General circulation model simulations of the Mars Pathfinder atmospheric structure investigation/meteorology data. *J. Geophys. Res.*, **104**, 8957–8974.

Hadfield, M. G., W. R. Cotton, and R. A. Pielke, 1991: Large–eddy simulations of thermally–forced circulations in the convective boundary layer. Part I: A small-scale circulation with zero wind. *Bound. Layer Meteor.*, **57**, 79–114.

Kanak, K., D. Lilly, and J. Snow, 2000: The formation of vertical vortices in the convective boundary layer. *Q. J. R. Meteor. Soc.*, **126**, 2789–2810.

Lee, T. J., R. A. Pielke, R. C. Kessler, and J. Weaver, 1989: Influence of cold pools down–stream of mountain barriers on downslope winds and flushing. *Mon. Wea. Rev.*, **117**, 2041–2058.

Leovy, C. B., and Y. Mintz, 1969: Numerical simulation of the atmospheric circulation and climate of Mars. *J. Atmos. Sci.*, **26**, 1167–1190.

Louis, J. F., 1979: A parametric model of vertical eddy fluxes in the atmosphere. *Bound. Layer Meteor.*, **17**, 187–202.

Mahrer, Y., and R. A. Pielke, 1977: A numerical study of airflow over irregular terrain. *Beitr. Phys. Atmos.*, **50**, 98–113.

Mason, P.J., 1989: Large–eddy simulation of the convective atmospheric boundary layer. *J. Atmos. Sci.*, **46**, 1492–1516.

Mass, C., and C. Sagan, 1976: A numerical circulation model with topography for the Martian summer hemisphere. *J. Atmos. Sci.*, **33**, 1418–1430.

Mellor, G. L., and T. Yamada, 1982: Development of a turbulence closure model for geophysical fluid problems. *Rev. Geophys. Space Phys.*, **20**, 851–875.

Metzger, S.M., J.R. Carr, J.R. Johnson, T.J. Parker, and M. Lemmon, 1999: Dust devil vortices seen by the Mars Pathfinder camera. *Geophys. Res. Lett.*, **26**, 2781–2784.

Meyers, M. P., and W. R. Cotton, 1992: Evaluation of the potential for wintertime quantitative precipitation forecasting over mountainous terrain with an explicit cloud model. Part I: Two–dimensional sensitivity experiments. *J. Appl. Meteor.*, **31**, 26–50.

Moeng, C.H., and Rotunno, R., 1990: Vertical–velocity skewness in the buoyancy–driven boundary layer. *J. Atmos. Sci.*, **47**, 1149–1162.

Moeng, C. H., and P. P. Sullivan, 1994: A comparison of shear– and buoyancy–driven planetary boundary layer flows. *J. Atmos. Sci.*, **51**, 999–1022.

Moriyama, S., and T. Iwashima, 1980: A spectral model of the atmospheric general circulation of Mars: A numerical experiment including the effects of suspended dust and the topography. *J. Geophys. Res.*, **85**, 2847–2860.

Odaka, M., K. Nakajima, S. Takehiro, M. Ishiwatari, and Y.–Y. Hayashi, 1998: A numerical study of the Martian atmospheric convection with a two dimensional anelastic model. *Earth, Planet and Space*, **50**, 431–437.

Odaka M., 2001: A numerical simulation of Martian atmospheric convection with a two-dimensional anelastic model: A case of dust–free Mars. *Geophys. Res. Lett.*, **28**, 895–898.

Owen, T., 1992: *Mars.* Chapter 25: The composition and early history of the atmosphere of Mars. The University of Arizona Press, Tucson, 818–834.

Pielke, R. A., G. Dalu, J. S. Snook, T. J. Lee, and T. G. F. Kittel, 1991: Nonlinear influence of mesoscale landuse on weather and climate. *J. Climate*, **4**, 1053–1069.

Pielke, R. A., W. R. Cotton, R. L. Walko, C. J. Tremback, W. A. Lyons, L. D. Grasso, M. E. Nicholls, M. D. Moran, D. A. Wesley, T. J. Lee, and J. H. Copeland, 1992: A comprehensive meteorological modeling system — RAMS. *Meteor. and Atmos. Phys.*, **49**, 69–91.

Pollack, J. B., C. B. Leovy, Y. Mintz, and W. Van Camp, 1976: Winds on Mars during the Viking season: Predictions based on a general circulation model with topography. *Geophys. Res. Lett.*, **3**, 479–483.

Pollack, J. B., C. B. Leovy, P. W. Greiman, and Y. Mintz, 1981: A Martian general circulation experiment with large topography. *J. Atmos. Sci.*, **38**, 3–29.

Pollack, J. B., R. M. Haberle, J. Schaeffer, and H. Lee, 1990: Simulations of the general circulation of the Martian atmosphere. I. Polar processes. *J. Geophys. Res.*, **95**, 1447–1473.

Rafkin, S. C. R, R. M. Haberle, and T. I. Michaels, 2001: The Mars Regional Atmospheric Modeling System: model description and selected simulations. *Icarus*, **151**, 228–256.

Ryan, J. A., and R. D. Lucich, 1983: Possible dust devils: Vortices on Mars. *J. Geophys. Res.*, **88**, 11005–11011.

Savijärvi, H., and T. Siili, 1993: The Martian slope winds and the nocturnal PBL jet. *J. Atmos. Sci.*, **50**, 77–88.

Schmidt, H., and U. Schumann, 1989: Coherent structure of the convective boundary layer derived from large–eddy simulations. *J. Fluid Mech.*, **200**, 511–562.

Schneider, J. M., 1991. *Dual Doppler Measurement of a Sheared Convective Boundary Layer.* Ph.D. Thesis, The University of Oklahoma, Norman.

Schofield, J. T., J. R. Barnes, D. Crisp, R. M. Haberle, S. Larsen, J. A. Magalhaes, J. R. Murphy, A. Seiff, G. Wilson, 1997: The Mars Pathfinder atmospheric structure investigation/meteorology (ASI/MET) experiment. *Science*, **278**, 1752–1758.

Siili, T., 1996: Modeling of albedo and thermal inertia induced mesoscale circulations in the mid–latitude summertime Martian atmosphere. *J. Geophys. Res.*, **101**, 14957–14968.

Stull, R. B., 1988: *Boundary Layer Meteorology*. Kluwer Academic Publishers, Dordrecht.

Thomas, P., and P. J. Gierasch, 1985: Dust devils on Mars. *Science*, **230**, 175–177.

Toigo, A., and M. Richardson, 2002: A mesoscale model for the Martian atmosphere. *J. Geophys. Res.*, in press.

Tremback, C. J., and R. Kessler, 1985: A surface temperature and moisture parameterization for use in mesoscale numerical models. *Preprints, Seventh Conference on Numerical Weather Prediction*, Montreal, Canada, Amer. Meteor. Soc., 355–358.

Tripoli, G. J., and W. R. Cotton, 1982: The Colorado State University three–dimensional cloud/mesoscale model. Part I: General theoretical framework and sensitivity experiments. *J. Res. Atmos.*, **16**, 185–220.

Tyler, D. Jr., J. R. Barnes, and R. M. Haberle, 2002: Simulation of surface meteorology at the Pathfinder and VL1 sites using a Mars mesoscale model. *J. Geophys. Res.*, **107**,

Walko, R. L., W. R. Cotton, and R. A. Pielke, 1992: Large–eddy simulation of the effects of hilly terrain on the convective boundary layer. *Bound.–Layer Meteor.*, **58**, 133–150.

Wesley, D. A., J. F. Weaver, and R. A. Pielke, 1990: Heavy snow–fall during an extreme arctic outbreak along the Colorado Front Range. *Natl. Wea. Dig.*, **15**, 2–19.

Wilson, R. J., and K. Hamilton, 1996: Comprehensive model simulation of the thermal tides in the Martian atmosphere. *J. Atmos. Sci.*, **53**, 1290–1326.

Xian, Z., and R. A. Pielke, 1991: The effects of width of land masses on the development of sea breezes. *J. Appl. Meteor.*, **30**, 1280–1304.